CONSTRUCTING AND CHARACTERIZING A SCANNING SQUID MICROSCOPE FOR A CRYOGEN FREE DILUTION REFRIGERATOR

A Dissertation

Presented to the Faculty of the Graduate School

of Cornell University

in Partial Fulfillment of the Requirements for the Degree of

Doctor of Philosophy

by

David Henri Low

December 2021

CONSTRUCTING AND CHARACTERIZING A SCANNING SQUID MICROSCOPE FOR A CRYOGEN FREE DILUTION REFRIGERATOR

David Henri Low, Ph.D.

Cornell University 2021

Superconducting quantum interference devices, or SQUIDs, are highly sensitive to magnetic flux and can be used to perform magnetic imaging at cryogenic temperatures. In this dissertation, I describe the first scanning SQUID microscope in a cryogen-free dilution refrigerator. First, I briefly describe basic SQUID theory, how to perform scanning SQUID microscopy, and how to design SQUIDs suited for microscopy. Next, I discuss both the apparatus and method to systematically characterize SQUIDs. I demonstrate that while heuristics provide guidance for finding low noise operating points, one often misses the best noise performance of the SQUID found by a systematic search. I also briefly discuss how to use machine learning to predict SQUID noise. I then describe in depth the design of the SQUID microscope, focusing on explaining the reasons behind various features of the coldfinger and microscope. Finally, I describe how to characterize vibrations in our microscope using images of a vortex in a superconductor.

BIOGRAPHICAL SKETCH

David Henri Low received a B.S. in Physics from UCSB and was admitted to the Applied and Engineering Physics Ph.D. program at Cornell University in 2014. He joined Katja Nowack's research group in early 2015 as one of the two first students.

For Elaine

ACKNOWLEDGEMENTS

I thank Katja Nowack my P.I., for her unwavering support and indispensable mentorship over the last 7 years. I thank all graduate & undergraduate students, other members of the Nowack Lab, and Eric Smith for their invaluable help in lab and steadfast friendship outside lab. I thank Mark Ketchen and John Kirtley for their patience and guidance.

I thank my committee members Greg Fuchs and Bart Selman for their insights, clarity, and inspiration. I thank my cohort and my fellow basement dwellers of PSB and Clark Hall who are too numerous to name (without fear of excluding someone important) and whose contributions are immeasurable.

Finally, I thank my family and friends for providing the "carrot and stick" without which I would not be who I am today.

TABLE OF CONTENTS

LIST OF FIGURES

CHAPTER 1

INTRODUCTION

From an early age, I was taught that good results come from a strong foundation. Just as it is hard to run before one can walk and difficult to learn quantum mechanics before calculus, it is challenging to do experimental physics research without reliable instruments. In my time at Cornell University working with Katja Nowack, I tried to create reliable and functional scientific apparatuses and other foundations on which others could build. In this dissertation, I describe some of the devices and apparatuses I designed and constructed. I illustrate the challenges we were trying to solve and the shortcomings of my designs so future students and scientists can improve on my attempts.

1.1 Motivation

The primary instrument I helped to build and characterize is a scanning SQUID microscope with micron precision in a cryogen-free dilution refrigerator with a 6 Tesla magnet. One of the motivations behind this microscope was to image magnetically doped topological insulators that exhibit the the quantum anomalous hall (QAH) effect [9]. We wish to image the magnetic domains of materials that exhibit the QAH effect and how current flow through the devices. Some of the main requirements performing these imaging experiments are:

1. 10 mK base temperature to firmly be in the QAH regime
2. High out of plane magnetic field to magnetize the samples
3. 1 µm spatial resolution to resolve current density and magnetic domains

4. $1\,\mu\Phi_0/\sqrt{\text{Hz}}$ magnetic flux sensitivity to observe nA scale currents. Note that Φ_0 is the magnetic flux quantum.

While the QAH effect could theoretically occurs at the Curie temperature of these materials, usually around 15 K, it is observed that quantized resistance only occurs at millikelvin temperatures [10, 22]. Recently the QAH effect has been observed at 1.9 K [15] but lower temperatures are useful for samples that are not perfect. Requiring temperatures below 300 mK necessitates a dilution refrigerator.

Similarly, the QAH effect can be achieved with 0.1 T but some samples require 2 T [44]. While it is not necessary to have a vector magnet, it could be useful. We chose a 6T-1T-1T 3D vector magnet. While a large magnet in our system requires different designs, the difference to our microscope design between a 1 T and a 6 T magnet are minimal. Generally, designing a scanning probe microscope with a large magnet makes the use of spring stages or similar methods of vibration damping challenging.

The desired magnetic flux sensitivity can be estimated from two sources: measuring the magnetic domains in a QAH material and measuring current flow through the sample. Magnetic domains in QAH samples have been imaged using a SQUID-on-a-tip [42] and have found the domains to be easily visible on a colorbar with 200 µT range. For a 1 µm diameter pickup loop, $1\,\text{m}\Phi_0/\sqrt{\text{Hz}}$ is roughly equivalent to 1 µT magnetic field sensitivity. The more difficult measurement is to detect edge currents flowing through QAH samples. Common current amplitudes are around 10 nA. For a wire carrying 10 nA, the magnetic field at a SQUID loop 1 µm away is 2 nT, which is just within the $1\,\mu\Phi_0/\sqrt{\text{Hz}}$ noise floor of our SQUIDs.

If we use a $1\,\mu\Phi_0/\sqrt{\text{Hz}}$ SQUID sensor and build a microscope in a cryogen-free dilution refrigerator with a 6 T magnet, we should be able to study samples that exhibit the QAH effect. The two main difficulties are then finding SQUIDs with $1\,\mu\Phi_0/\sqrt{\text{Hz}}$ and designing a microscope that achieves low vibrations so that we can exploit the approximately 1 µm spatial resolution of our SQUIDs. We expect that vibrations with peak amplitudes below $100\,\text{nm}/\sqrt{\text{Hz}}$ and cumulative vibrations of below 100 nm should be adequate for our goals.

1.2 Outline

This dissertation describes the steps we took to build the first scanning SQUID system in a cryogen free system with a large superconducting magnet for use in studying the QAH effect. I describe the design and characterization of the SQUIDs, then describe how we designed and characterized the first cryogen-free scanning SQUID microscope in a dilution refrigerator that has below $100\,\text{nm}/\sqrt{\text{Hz}}$ vibration noise peaks.

In Chapter 2, I give some background on SQUIDs on how to use a SQUID for imaging. I describe how we design our magnetometers, also called susceptometers [32] , to optimize their use for imaging planar samples with sub-micron precision.

In Chapter 3, I describe how to characterize SQUID noise and some methods to search for SQUIDs with a low noise floor. We found that the SQUIDs had a large variability in their noise floor and could screen the SQUIDs before using them in an imaging experiment to achieve more sensitive or faster experiments.

In Chapter 4, I describe how to build the scanning SQUID microscope compat-

ible with a cryogen-free dilution refrigerator. I focus on describing the objectives, the design, and the shortcomings of the coldfinger and microscope body.

In Chapter 5, I discuss methods of characterizing the SQUID microscope. Scanning SQUID magnetometry is an established technique in systems with liquid cryogens. Our system is unique because it contains both a dilution cycle to cool to 10 mK and uses a cryocooler instead of liquid cryogens. The cryocooler produces vibrations so I focus on characterizing these vibrations when imaging with our SQUID microscope.

CHAPTER 2

SQUID MAGNETOMETERS

SQUIDs are among the most sensitive magnetic sensors available. Some applications of SQUIDs include measuring transition edge sensors for investigating the cosmic microwave background [51, 49, 61], forming superconducting qubits [11, 39, 1, 2] or couplers [75, 60], measuring the brain or other biological samples [27, 20, 53, 55, 54], motion detection [28, 18], and scanning SQUID microscopy. Scanning SQUID microscopy can be used to image static stray magnetic fields above a sample, to measure local magnetic response and to image the magnetic field produced by applied and spontaneous currents in a device. This technique has been applied to a wide variety of quantum materials and mesoscopic devices including unconventional superconductors [34], topological insulators [52, 41], complex oxides [3, 31, 73, 23, 12], superconducting and normal metal rings [37, 40, 7], unconventional Josephson junctions [24, 66] and a variety of graphene structures [25, 48, 70, 69]. In this chapter, I will describe some basic SQUID theory, how to use SQUIDs as scanning magnetometers, and discuss our SQUID designs.

2.1 Basic SQUID Theory

A SQUID is a loop of superconducting material interrupted by Josephson junctions. These junctions can be formed using either constrictions of the superconducting material or using a resistive element such as in the in $Nb/Al_2O_3/Nb$ Josephson junctions. There are two general types of SQUIDs: RF and DC SQUIDs. RF SQUIDs use a single junction in parallel with a large capacitance. By using parametric amplification, low noise cryogenic HEMT amplifiers, and other microwave measurement techniques, it is possible to achieve at least $0.1\,\mu\Phi_0/\sqrt{\text{Hz}}$ noise per-

formance [26]. However, microwave coaxial cables leading to the SQUID and sophisticated room temperature electronics are required. DC SQUIDs are formed by a loop interrupted by two Josephson junctions. There is a shunt resistor in parallel with each junction. A diagram of a DC SQUID can be found in Figure 2.1.A.

DC SQUIDs are very well studied and are discussed in detail in Ref [8]. DC SQUIDs are flux sensitive; the current-voltage (IV) characteristics of a DC SQUID for different amount of magnetic flux threading through the SQUID loop is shown in Figure 2.1.B,C. The response to magnetic flux of a SQUID is periodic as can be seen in Figure 2.1.C. The periodicity is given by $1\,\Phi_0$.

The IV characteristics of a Josephson junction can be hysteretic which makes DC SQUIDs hysteretic. Hysteretic SQUIDs are difficult to use for magnetometry. The hysteresis can be removed with sufficiently large shunt resistance across the junction. In particular, we want the Stewart-McCumber parameter

$$\beta_C = 2\pi I_0 R^2 C/\Phi_0 = \omega_J RC \geq 1 \tag{2.1.1}$$

where $\omega_J/2\pi = I_0 R/\Phi_0$ the Josephson frequency at voltage $I_0 R$ where I_0 is the critical current of the Josephson junction, R is the value of each shunt resistor, and C is the self-capacitance of the SQUID.

When a DC SQUID is appropriately current biased, a small magnetic flux oscillation results in a voltage oscillation which dictates the SQUID sensitivity to magnetic flux. Simulations demonstrate that the SQUID sensitivity is maximized when β_C is just below 1, or just before the SQUID becomes hysteretic and when the SQUID screening parameter

$$\beta_L = 2LI_0/\Phi_0 = 1 \tag{2.1.2}$$

where L is the SQUID self-inductance, usually dominated by the SQUID loop. At

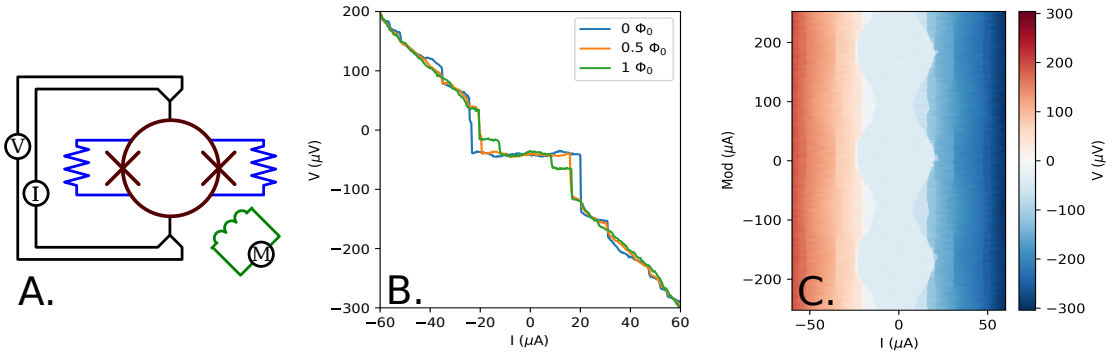

Figure 2.1: SQUID Theory. (A) Diagram of a DC SQUID with a flux bias denoted by M. The SQUID is in red, the shunt resistors are in blue, and the flux bias line or modulation coil is in green. (B) IV characteristics of a typical SQUID with flux bias at 0, 0.5, and 1 Φ_0. (C) Modulation plot of the SQUID showing periodicity of about 150 µA.

$\beta_L = \beta_C = 1$, one can predict that the SQUID transfer function or flux sensitivity

$$V_\Phi = \left|\frac{\partial V}{\partial \Phi}\right| \leq R/L.$$

If we assume that the noise from a SQUID is solely a result of Johnson noise from the shunt resistors

$$S_V(f) = 4k_B T R = v_n^2$$

where T is the temperature of the resistor and R is the resistance, we can find that the flux noise of the SQUID should be

$$S_\Phi(f) = \frac{S_V}{V_\Phi^2} \leq \frac{16k_B T R}{R^2/L^2} = 16k_B T L^2/R. \tag{2.1.3}$$

Note that the current noise per hertz of bandwidth for a single resistor is $i_n = (4k_B T/R)^{1/2}$, so two parallel noise sources give $(16k_B T/R)^{1/2}$ current noise per hertz bandwidth or a voltage noise power per hertz bandwidth of $16k_B TR$. Plugging in typical values for our SQUIDs of $T = 4\,\mathrm{K}$, $L = 100\,\mathrm{pH}$ and $R = 4\,\Omega$, we find $S_\Phi^{1/2}(f) \simeq 0.7\,\mu\Phi_0/\sqrt{\mathrm{Hz}}$ which is close to the minimum observed SQUID noise in our devices. Note that in our devices, we often target $\beta_L, \beta_C < 1$ with some safe

margin. It is challenging to accurately predict the total self-capacitance and self-inductance in our designs. As $\beta_C \propto C$ and $\beta_L \propto L$ and exceeding $\beta_C, \beta_L = 1$ results in hysteretic or very noisy SQUIDs, it is prudent to choose I_0 and R conservatively.

2.2 Scanning SQUID Overview

SQUIDs can be used as highly sensitive magnetic flux sensors because tiny amounts of magnetic flux that threads through the SQUID loop results in measurable currents. However, many design features are required to turn this sensitive device into a magnetic probe for micron-scale imaging.

To achieve micron-scale spatial resolution, our SQUIDs are designed with a small sensitive region or pickup loop. The pickup-loop is brought close and raster-scanned over the sample to produce an image. A side view of the scanning setup is shown in Figure 2.3. The SQUID is moved using homemade fine positioners made from piezoelectric components and are described in more detail in section 4.3.2. The pickup-loop is described in detail in section 2.4.2.

To facilitate imaging, the SQUID is placed on a printed circuit board (PCB) and bolted to the homemade fine positioning piezo stack described in section 4.3.2. A diagram of the SQUID PCB is shown in Figure 2.2. To determine the distance of the SQUID from the sample, a capacitive measurement is used. The SQUID is mounted to a copper or brass cantilever which is glued to a piece of cigarette paper or another piece of thin, electrically insulating material. A copper pad on the PCB provides the other side of the parallel plate capacitor. When the SQUID PCB is raised by the fine positioning piezo stack high enough that the SQUID touches the sample, the cantilever deflects and a change in the capacitance

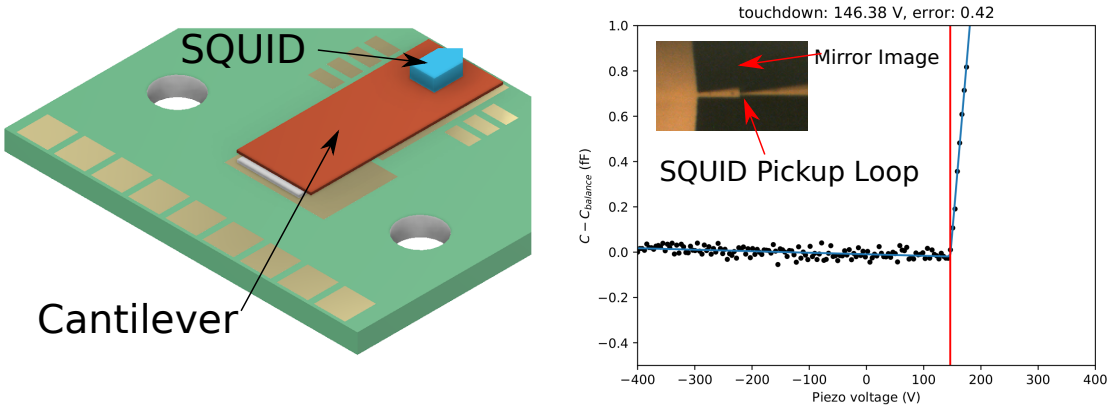

Figure 2.2: SQUID PCB diagram (left) and an example of the capacitive touchdown measurement used to determine when the SQUID touches the sample (right). The capacitance is measured between the brass cantilever and a copper pad on the PCB. The angle between the SQUID and the sample must be aligned carefully to allow the SQUID pickup loop to touch the sample first to guarantee that the SQUID achieves micron precision. The alignment angle is demonstrated in an insert on the right panel.

can be measured. We call the process in which the SQUID touches the sample a "touchdown" measurement. An example of the capacitive measurement and a touchdown is shown in Figure 2.2.

The SQUIDs are designed such that the pickup loop of the SQUID comes in contact with the sample before any other part of the SQUID chip if the SQUID PCB is aligned properly using the goniometer. More details about the SQUID design is present in section 2.3. Basically, the SQUID pickup loop is positioned at the front of the SQUID chip. The superconducting shields that prevent magnetic flux from threading into the SQUID loop at all locations except the pickup loop are carefully designed such that aligning the outer edge of the field coil or the pickup loop to the sample guarantees that SQUID pickup loop gets within a micron of the sample. An example of this alignment can be seen in the insert of Figure 2.2. To properly check the alignment of the SQUID, one must check the angle

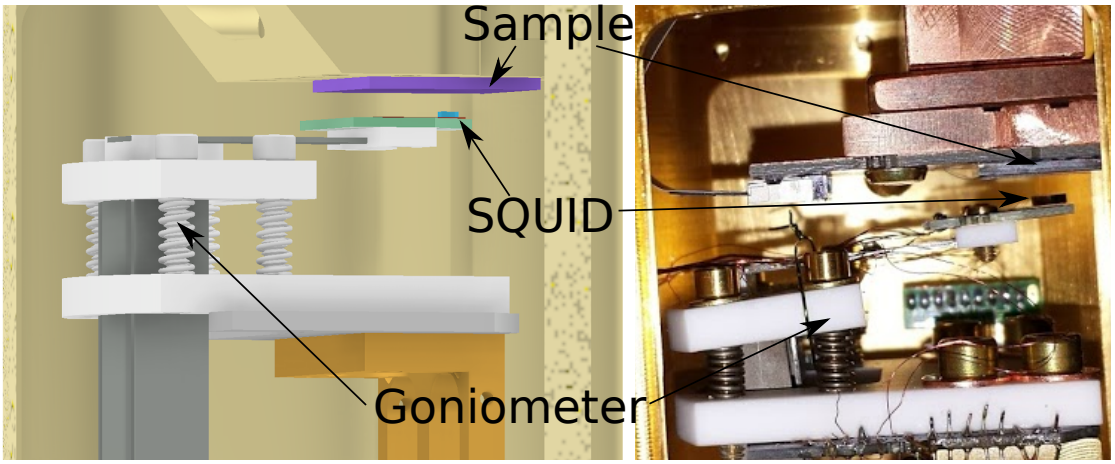

Figure 2.3: Diagram (left) and image (right) of the SQUID scanning setup. The SQUID chip is visible and indicated in both panels. The SQUID is brought close to the sample with course and fine positioners. A goniometer made up of 4 spring-loaded screws and two Macor plates changes the angle of the fine positioner stack and SQUID with respect to the sample.

from the front and each side of the SQUID. As most samples used in the scanning SQUID microscope are smooth enough that a mirror image of the SQUID is visible, checking the alignment can be accomplished by observing the mirror image of the SQUID chip and make adjustments until the front edge of the chip and the step formed by etching over the pick up loop near the superconducting shield will hit the sample at almost the same time. This process guarantees the pickup loop will be within a micron of the sample when in contact. This process requires the SQUID chip to end approximately within a micron of the outer edge of the field coil. We accomplish this by polishing the SQUID chip using diamond lapping film discs from Allied High Tech Products. These film discs are commonly used for preparing SEM/TEM samples and can rapidly remove material while leaving a smooth finish.

The angle of the SQUID PCB can be changed using the goniometer shown in Figure 2.3. Three contact points are necessary to define an angle so the fourth

screw in the goniometer is often unused. Earlier goniometer designs possess three screws oriented in a way that adjusting them is more intuitive. However, the small sample space prevents such a design in the dilution refrigerator. The goniometer changes the angle of the entire fine positioner piezo stack as the X piezos are glued to the upper Macor block of the goniometer. More details can be found in section 4.3.2.

As the maximum angle of the goniometer is constrained by the diameter of the screw clearance holes on the top Macor pieces, it is essential that the SQUID and the sample are glued as flat as possible to ensure that the SQUID is able to be aligned using the goniometer. One must also carefully wirebond to the SQUID and sample to ensure that the wirebonds do not touch before the SQUID pickup loop. If even a single wirebond touched first, the capacitive height measurement would detect a touchdown while the SQUID pickup loop was still very far from the sample. The screws used to attach the SQUID PCB to the fine positioner are often filed down to prevent them from touching first.

2.3 SQUID Magnetometers Design

SQUIDs used as a scanning magnetometer are carefully designed. In general, the two ways to achieve good spatial resolution for a SQUID is 1) make a very small SQUID, often in a single metal layer with constriction type junctions or 2) have a separate pickup loop that is very small and shield the rest of the SQUID from magnetic fields. As it is difficult to add a flux bias line to the small SQUIDs, these coplanar SQUIDs often have limited dynamic range as a flux bias needs to be applied to the entire sample. Susceptibility measurements or measurements

that require a local perturbation to the sample is also very challenging in coplanar SQUIDs [38]. For these reasons, we choose the second design type [29]. A diagram of the SQUID design can be seen in Figure 2.4. There are a few key features to such SQUIDs:

1. Small pickup loop: The size of the SQUID pickup loop dictates the spatial resolution of the SQUID.
2. Shielded, coaxial design: We wish for the SQUID to only be sensitive to magnetic flux from the pickup loop so we can perform local magnetometry of a sample.
3. Field Coil: The SQUID has a on-chip flux bias line at the pickup loop that can be used to apply a local magnetic field to the sample. The field coil is balanced such that it is possible to apply very little net magnetic field to the SQUID but a substantially larger magnetic field to the sample. The field coil is used to perform local magnetic response measurements or magnetic susceptibility. This feature gave these SQUIDs the nickname, "susceptometers".
4. Careful aligning geometry: The coaxial shield, pickup loops, and field coil are carefully designed such that the SQUID pickup loop can get within a micron of the sample.
5. Gradiometric: The SQUID loop has a twist in it like a figure "8". A uniform magnetic field will add zero net magnetic flux to the SQUID. The gradiometric design combined with the field coil allows us to apply a local magnetic field to the sample without adding a net magnetic flux through the SQUID. However, fabrication imperfections prevents the SQUIDs from being completely insensitive to a uniform magnetic field.

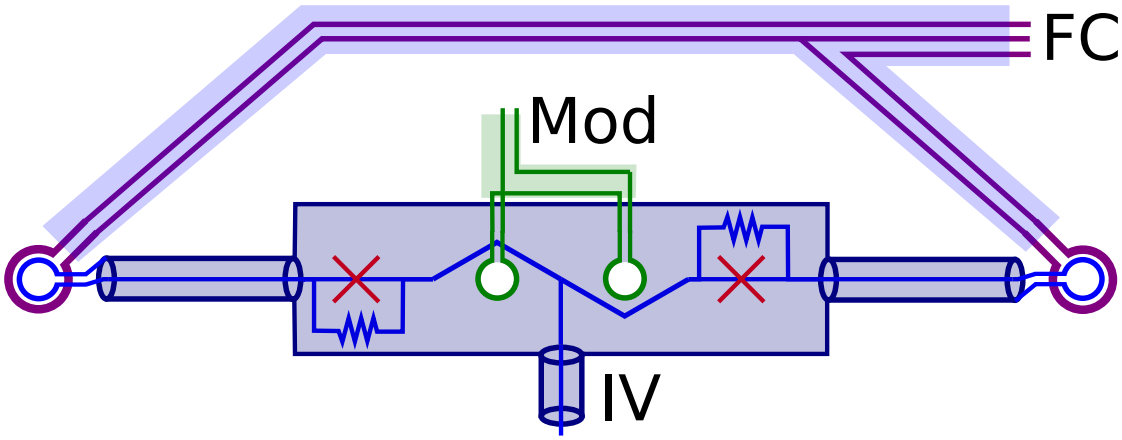

Figure 2.4: Diagram of SQUID magnetometers. The magnetometers are gradiometric so a uniform magnetic fields produces no net flux through the SQUID loop. The sensitive regions, or pickup loops, are located on each end and the rest of the SQUID and are connected to the body of the SQUID by coaxial structures. The SQUID can be voltage biased using coaxial leads, labeled in the diagram by IV. One end of the pickup loop connects to the center conductor of the coaxial structures while the other connects to the ground shields. The junctions are embedded inside this coaxial structure and are resistively shunted. There are two flux bias lines: the mod coil, denoted by Mod, and the field coil, denoted by FC. The field coil applies a local magnetic field to the sample.

6. Modulation Coil: The SQUID has a dedicated flux bias line that couples magnetic flux into the SQUID. As the flux sensitivity of a SQUID is periodic in a flux quantum, it is useful to operate the SQUID in a PID flux locked loop. We use the modulation coil to keep the flux through the SQUID constant. More details in this measurement can be found in section 3.2.1. This flux bias line is far from the pickup loop to prevent the feedback loop from effecting the sample.

2.4 Hypres SQUIDs

Our SQUIDs were fabricated by Hypres Incorporated, a foundry that specializes in superconducting and semiconducting processes. The coaxial design of our SQUID requires 5 separate metal layers, many of which are above the Josephson junction. We provide GDS files that describe the metal layers, junction positions, and vias that are required for our SQUID and Hypres mails us 5×5 mm chips. We collaborated with three other labs in our Hypres order.

The basic building block of the design is a 1×1.6 mm chip that is tiled 5×3 to form a 5×5 mm block. This is tiled 2×4 to form a larger block that is then tiled throughout the wafer. This 10×20 mm chip is shown in Figure 2.6. Hypres dices the large chips to 5×5 mm and mails the completed chips to us as shown in Figure 2.5. To extract a single SQUID magnetometer, we dice the individual 5×5 mm chips in the Cornell clean room facilities.

The 10×20 mm design contains 8 distinct 5×5 mm designs. Four of them, marked by "D1", "D2", "D3", "D4" in Figure 2.6, contain 14 conventional SQUID magnetometers and a single test structure. The other 5×5 mm chips were reserved for each lab that contributed to this project to use for customized designs. In our custom 5×5 mm chip, we placed three conventional SQUID magnetometers, two test structures, five magnetometers with coplanar waveguides as field coil bias lines, and 20 "mini", non-gradiometric magnetometers with extremely small pickup loops. These mini magnetometers were designed to have superior spatial resolution and to be as small as possible so they could fit easier on the tip of a tuning fork.

In the following sections, I will describe the layout of the Hypres SQUIDs in further detail.

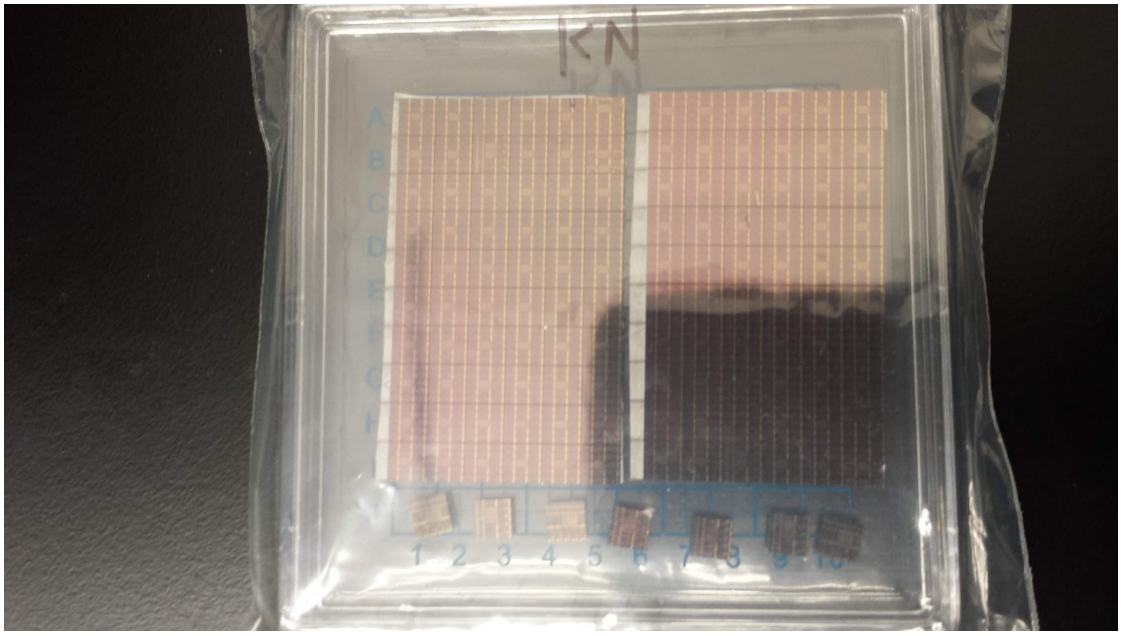

Figure 2.5: SQUIDs from Hypres. We receive diced 5x5 mm chips from Hypres. Each chip is one of 5 designs shown in more detail in Figure 2.6.

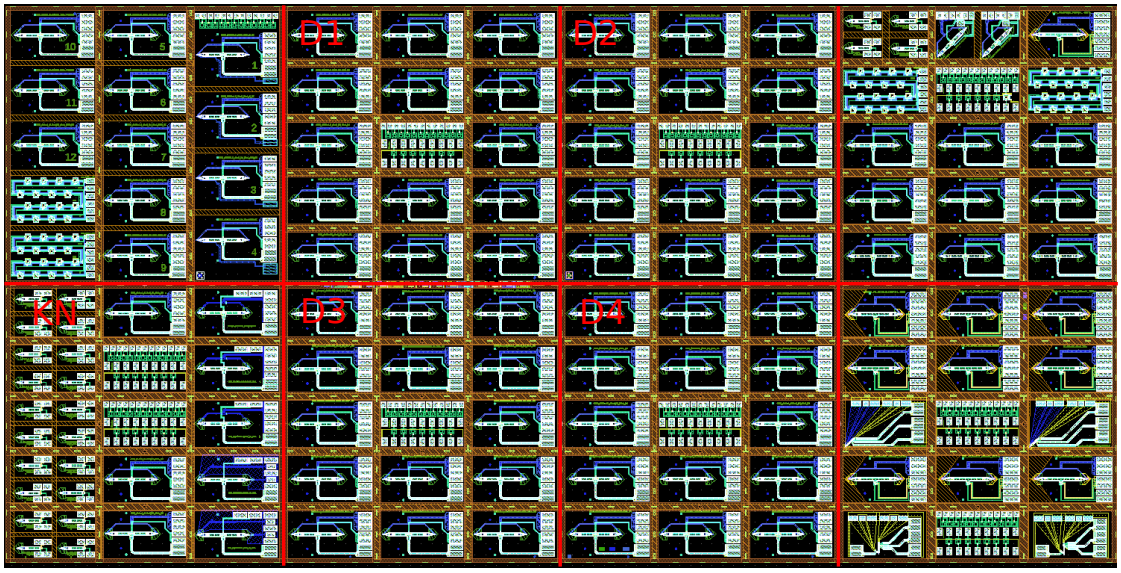

Figure 2.6: Overview of all SQUID designs from Hypres. The designs are placed in 5×5 mm squares, 15 designs per 5×5. There are eight 5×5 in the master design. These designs are tiled over the entire wafer. The 5×5s we received are marked by "D1", "D2", "D3", "D4", and "KN".

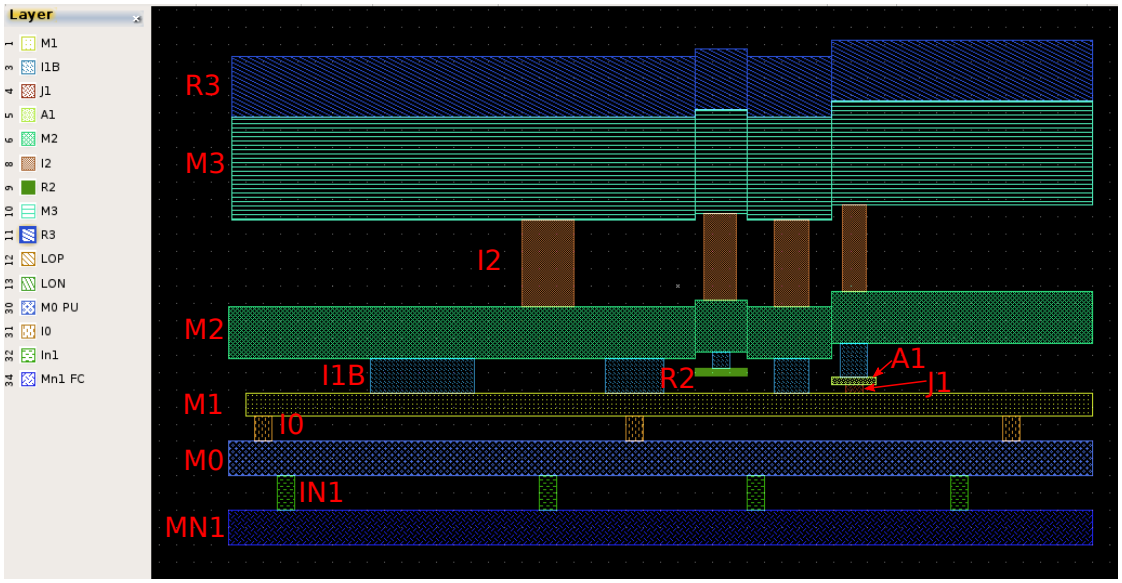

Figure 2.7: Hypres layer structure. Metal layers are made from niobium and are denoted by "M". Via layers are denoted by "I". A resistive layers is denoted by "R" while the junction is comprised of layers "A1" and "J1".

2.4.1 Layer Structure

I will first describe the layer structure of the Hypres Process.

Our SQUIDs are made using five niobium metal layers as depicted in Figure 2.7. Layer MN1, the deepest layer, forms the field coil of our SQUID. Layer M0 is used for the pickup loop. M1 and M2 form the metal surrounding the junction and M2 generally contains the bulk of one arm of the SQUID and the "inner conductor" of the coaxial design that our SQUIDs are built from. The "outer conductor" of the coax is formed by layers M1 and M3 with the edges of the coax being formed by via layers I2 and I1. R3 is used for wirebonding and is mostly used on the bonding pads. The resistors are formed using layer R2 and the junctions are formed with layers A1 and J1. The layers are not all planarized and sometimes additional height forms from the presence of R2 or junction layers. The LOP layer denotes

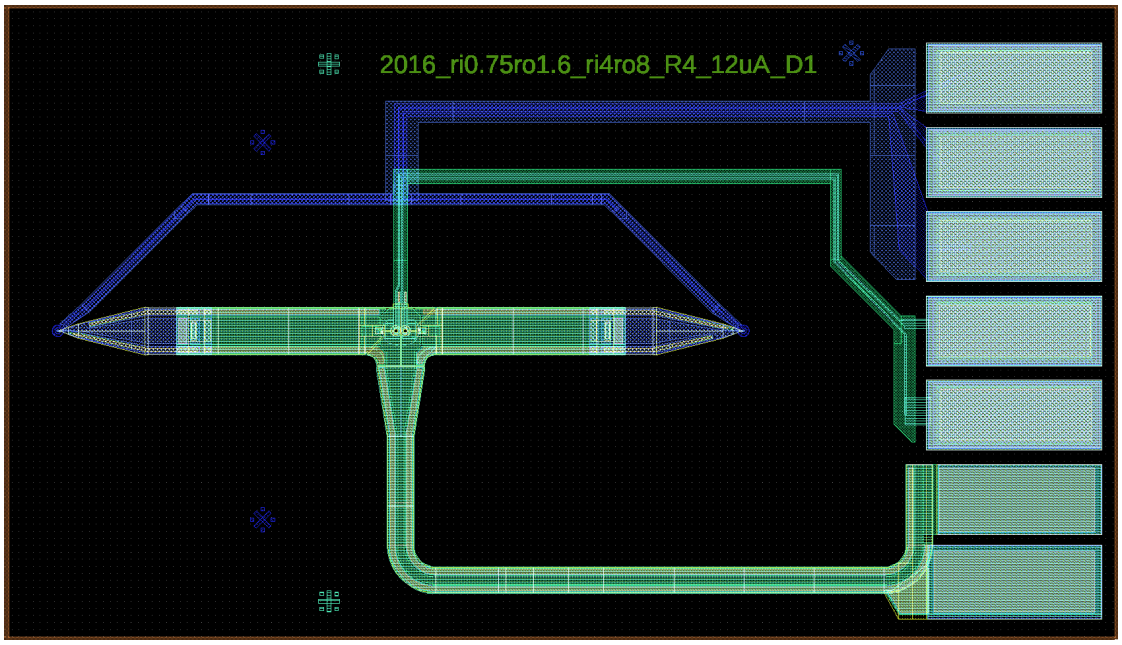

Figure 2.8: Design of a standard SQUID magnetometer. The pickup loop is located at the far left of the design and the bonding pads are at the right hand side. The field coil in blue is controlled by the top three pads. The modulation coil is controlled by the next two pads. Voltage or current biasing the SQUID can be accomplished using the bottom two pads.

dicing within a 5×5 mm and the LON layer provides etches the oxide above the the pickup loop area. For clarity, we do not show the LON layer in the diagrams.

In the following sections, the colors of each layer remains constant. We provide a legend in Figure 2.7. Note that every shape in this design is a feature; there are no negative masks where shapes denote the absence of a feature.

2.4.2 Standard SQUID Magnetometer

A basic SQUID magnetometer is depicted in Figure 2.8. The circuit diagram in Figure 2.4 was drawn to reflect these SQUID magnetometers. The gradiometric design is clearly visible from the symmetry in the x axis. The left pickup loop

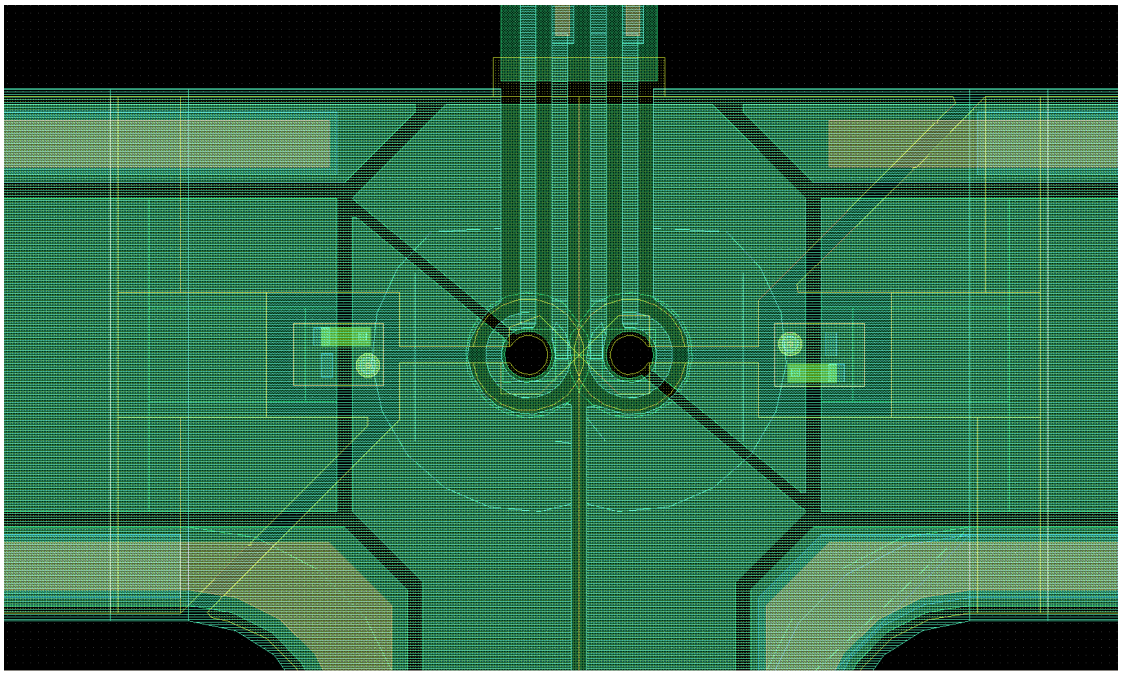

Figure 2.9: Junction area of standard SQUID magnetometers. The top and bottom metal layers in M3 and M1 respectively combined with the vias in I1 and I2 at the top and bottom of the SQUID body form the outer conductor of the coaxial design. The modulation coil is carefully wound to inject magnetic flux in the correct direction depending on the twist to make the SQUIDs gradiometric.

is the one brought near to the sample. The bonding pads on the right hand side of the image are used to control the field coil, modulation coil and to voltage or current bias the SQUID. Note that the field and modulation coils are shielded with a superconducting metal layer. The SQUID IV lines are coaxial, just like the SQUID body itself.

A zoom-in on the junction area is shown in Figure 2.9. The two yellow circles are the junctions themselves while the rectangles above the junctions are the shunt resistors that are in parallel with the junction. Note that metal layer M2 forms the bulk of the "center conductor" of the coaxial design and acts as one arm of the SQUID. Also note that all sensitive areas of the SQUID and all parts of the SQUID loop is covered by a superconducting metal layer. The modulation coils

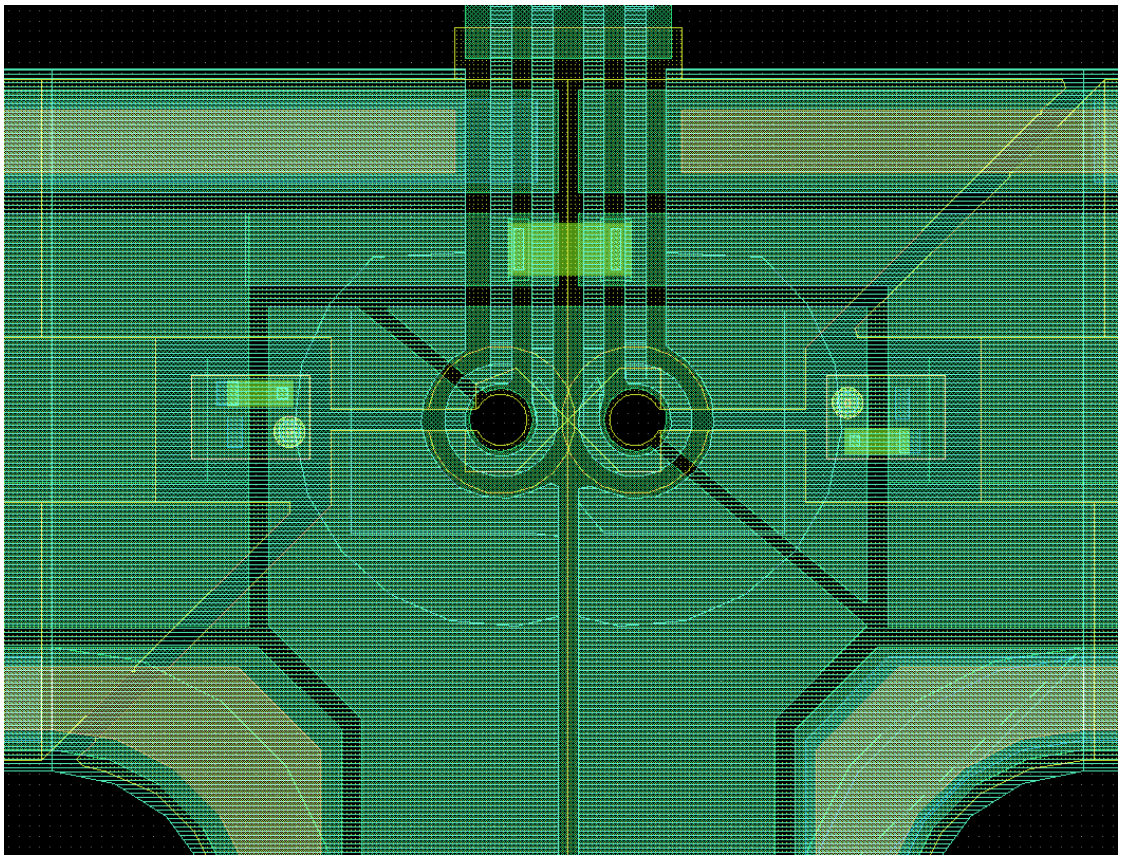

Figure 2.10: Junction area of Damped SQUID

are counter-wound to ensure magnetic flux is properly threaded into the SQUID loop. Note that a hole is cut in the superconducting shield to ensure flux can thread through the SQUID.

The junction area of a damped SQUID is shown in Figure 2.10. The damping resistor is shorted by superconducting metal through the outer conductor of the SQUID body and the pickup loops.

The SQUID IV pads are shown in Figure 2.11. The bottom pad clearly is shorted to the outer conductor of the leads while the upper pad is shorted to the inner conductor of the leads. This pattern is extended up to the junction area, as seen in Figure 2.9.

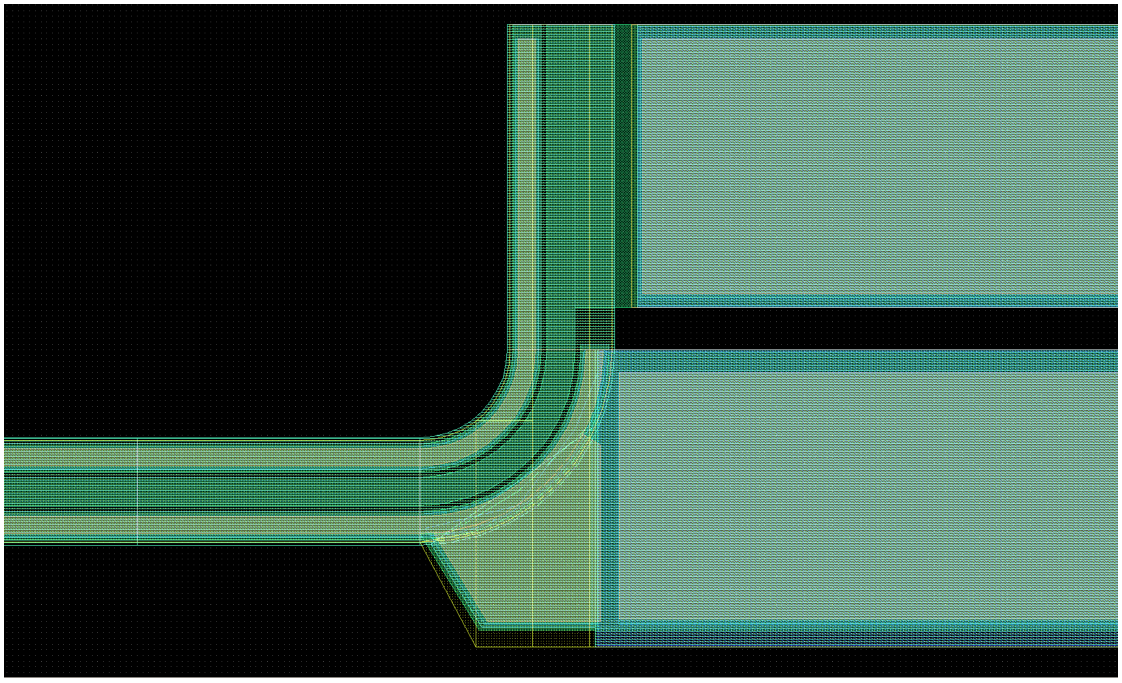

Figure 2.11: IV pads of standard SQUID magnetometer.

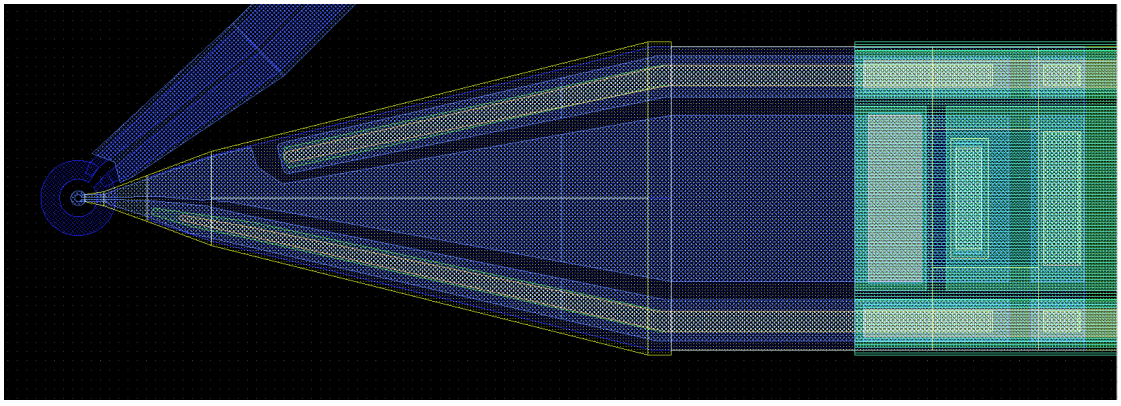

Figure 2.12: Pickup loop and coaxial SQUID body structure of a standard SQUID magnetometer

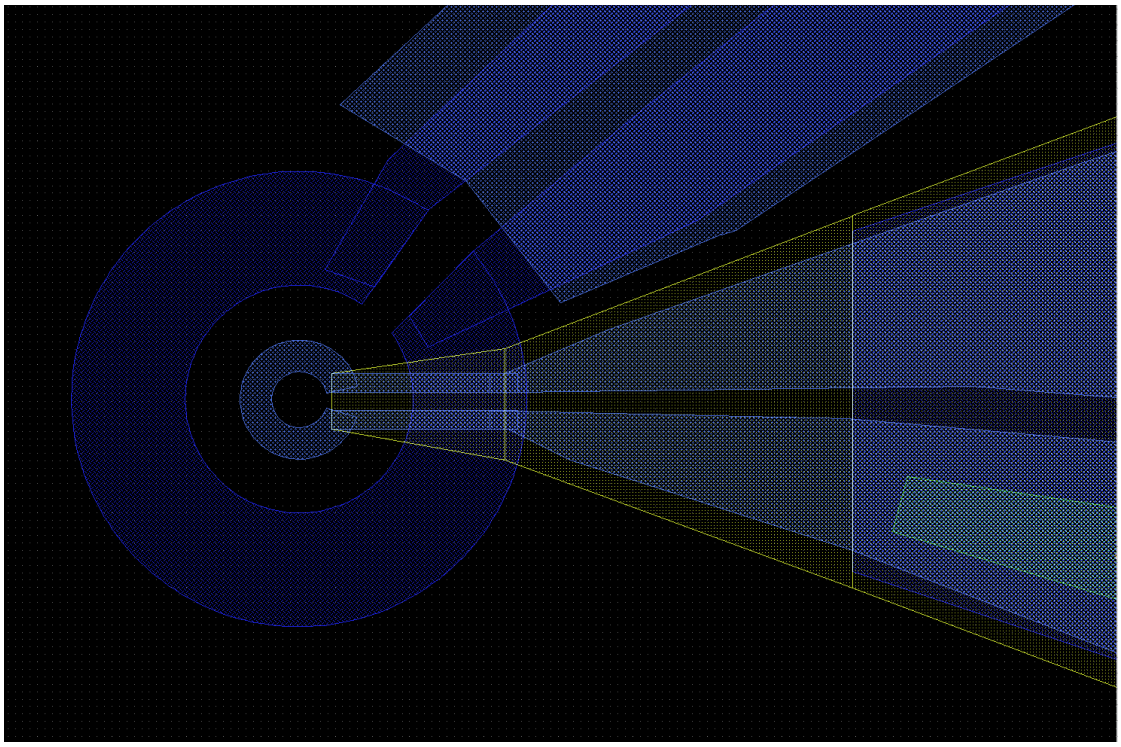

Figure 2.13: Close up view of the pickup loop of a standard SQUID magnetometer. The inner radius of the pickup loop is 0.75 µm while the inner radius of the field coil is 3 µm.

We can check that one end of the pickup loop connects to the center conductor and the outer conductor of the coaxial structure by examining Figure 2.13. Note that the upper and lower side of the loop connect to metal layers that become the center and outer conductor of the coaxial body of the SQUID in Figure 2.12. Vias bring the conductors up a layer far from the pickup loop to prevent the tall metal layers from interfering with scanning. Additionally, the blue metal layers (M0) do not interact directly with the junction layers so it makes sense to bring the SQUID leads up to the M2 and M1 layers. Note that the pickup loop is in layer M0 while the field coil is in the lower, MN1 metal layer.

Note that the superconducting shield to the pickup loop in the M1 layer slightly exposes the slot that forms the SQUID loop in Figure 2.13 and more dramatically

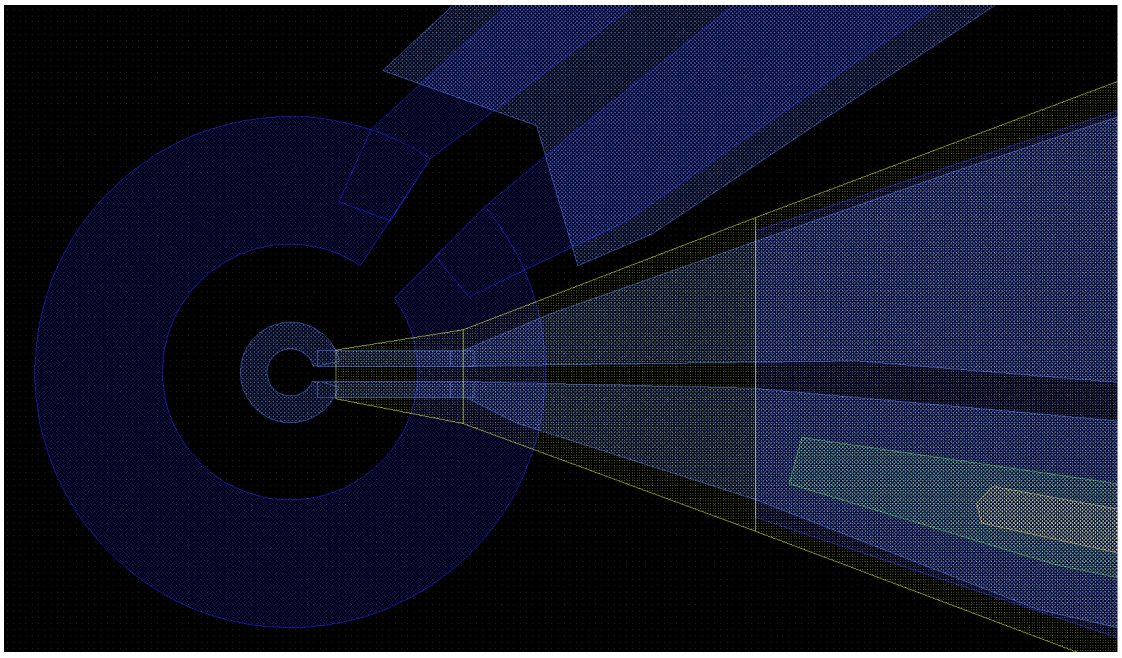

Figure 2.14: Close up view of the pickup loop of a standard SQUID magnetometer. The inner radius of the pickup loop is 0.75 µm while the inner radius of the field coil is 4 µm. Note that the larger field coil outer diameter demands a more shallow angle of approach. This requires the superconducting shield that covers the slot in the pickup loop to be slightly exposed.

in Figure 2.14 and Figure 2.15. The field coil for the SQUID design in Figure 2.13 was chosen such that if you polished within a micron of the outer diameter of the field coil and aligned at the proper angle, the pickup loop would touch the sample first. If the shield was positioned further towards the pickup loop, the shield might touch too soon, preventing the pickup loop from getting close enough to the sample. The shields in Figure 2.14 was chosen specifically to allow the pickup loop to get within a micron of the sample when the SQUID is in contact despite the larger field coil. Similarly, the smaller 0.4 µm radius pickup loop in Figure 2.15 requires an even more recessed superconducting shield.

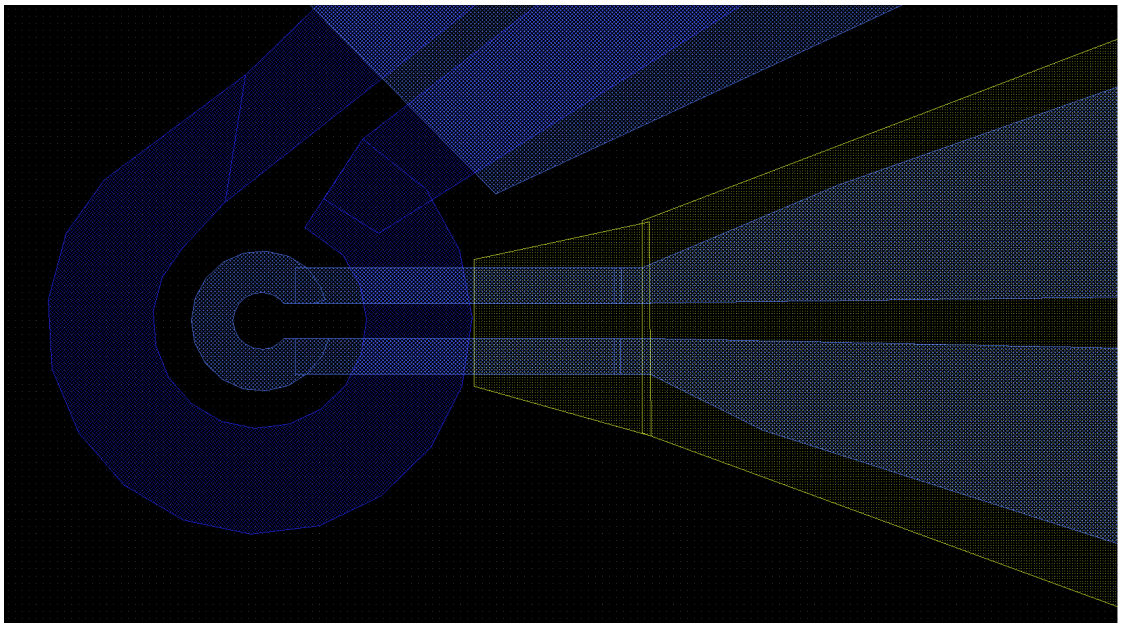

Figure 2.15: Close up view of the pickup loop of a standard SQUID magnetometer. The inner radius of the pickup loop is 0.4 µm while the inner radius of the field coil is 1.5 µm. This was the smallest pickup loop that Hypres would guarantee.

2.4.3 Test Structures

The test structures were designed to help troubleshoot if the SQUID magnetometers were hysteretic or otherwise unusable. We wished to have ways to test both the junctions and the simplest possible SQUID design. We varied the shunt resistances of the junctions as a way to probe parasitic self-inductance and capacitance.

The entire test structure chip is shown in Figure 2.16. The top row contains structures to test single junctions with different shunt resistances while the bottom row contains washer SQUIDs, the simplest SQUID design we could possibly construct. Each SQUID has a different shunt resistor and the same flux bias line. The size of the washer was chosen to approximate the designed self-inductance of our SQUIDs. The rule of thumb for washer SQUIDs is

$$L = L_h + L_{sl} + L_j$$

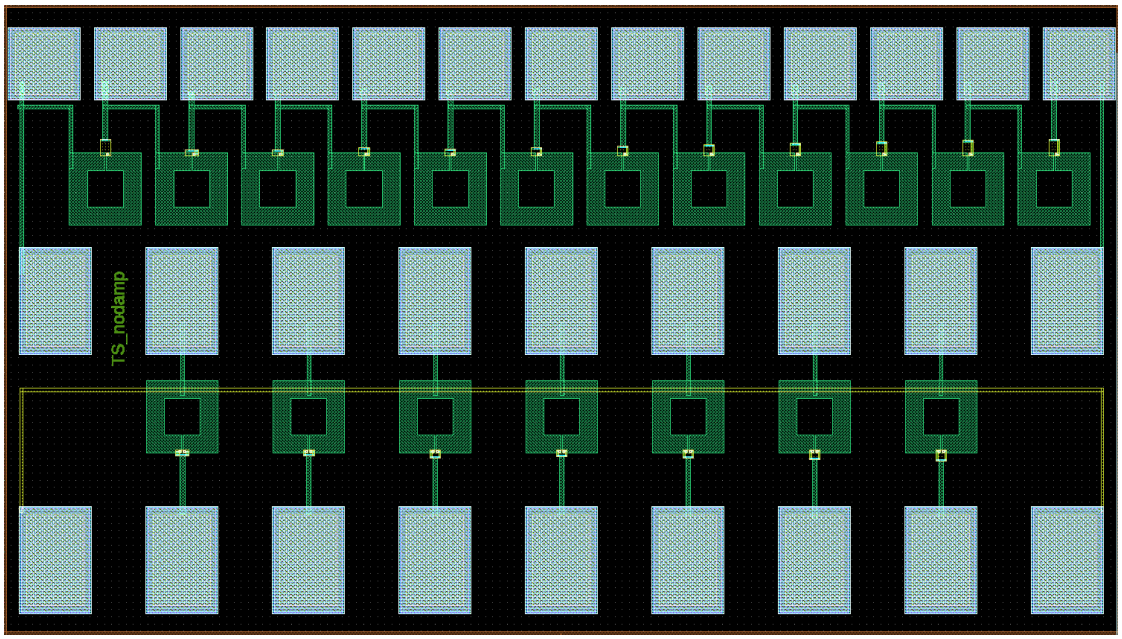

Figure 2.16: Hypres test structures for each 5×5 mm chip. The top structures are to test junctions while the bottom are washer SQUIDs.

where the square washer with a square hole inductance $L_h = 1.25\mu_0 d$ where d is the inner side length of the square washer and the slit inductance without ground plane is L_{sl} =0.3 pH/µm [8].

As the washer SQUIDs are designed to simulate the real SQUID magnetometers, the self-inductance and critical current is fixed. So, parameter $\beta_L = 2LI_0/\Phi_0$ is fixed. The Stewart-McCumbert parameter $\beta_c = (2\pi/\Phi_0)I_0R^2C$ which, if larger than 1predicts the SQUID will be hysteretic, can be probed by different R shunt resistances. This allows us to probe if the junction parasitic capacitance is larger than expected by searching for the lowest shunt resistor that gives a hysteretic SQUID.

The junction area of a washer SQUID is depicted in Figure 2.17. This washer SQUID is damped; undamped washer SQUIDs lack the upper resistor that is

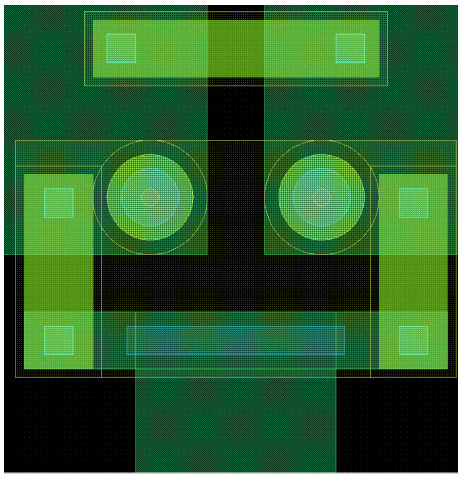

Figure 2.17: Damped washer SQUID.

shorted by the square washer.

2.4.4 Magnetometers with Coplanar Waveguide Field Coils

We designed two types of SQUID magnetometers with field coils capable of supporting GHz excitations using coplanar waveguides. The impedance of the waveguides in both types of magnetometers were designed to be $50\,\Omega$. The first design, shown in Figure 2.18 uses a simple coplanar waveguide design. Extra pads are necessary to have the three ground wires. These can be shorted at the pads but were necessary to avoid vias which might introduce inductance. The alternate design uses an extremely large ground plane as shown in Figure 2.19. To date, we have not tested the high frequency performance of the coplanar waveguide field coils.

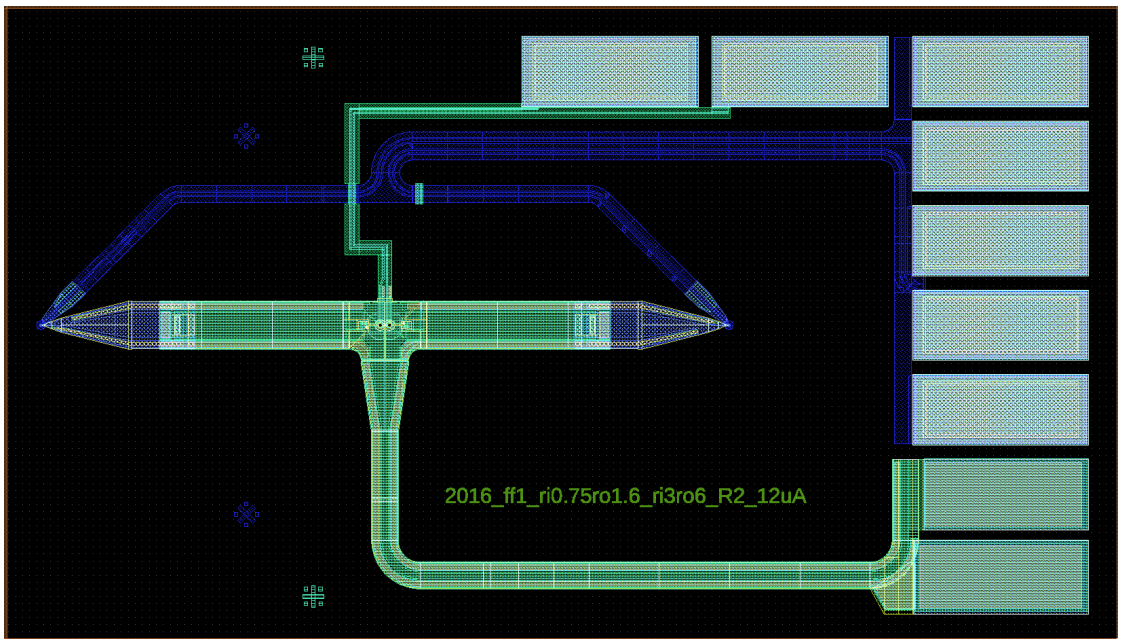

Figure 2.18: SQUID magnetometer with coplanar waveguide field coil

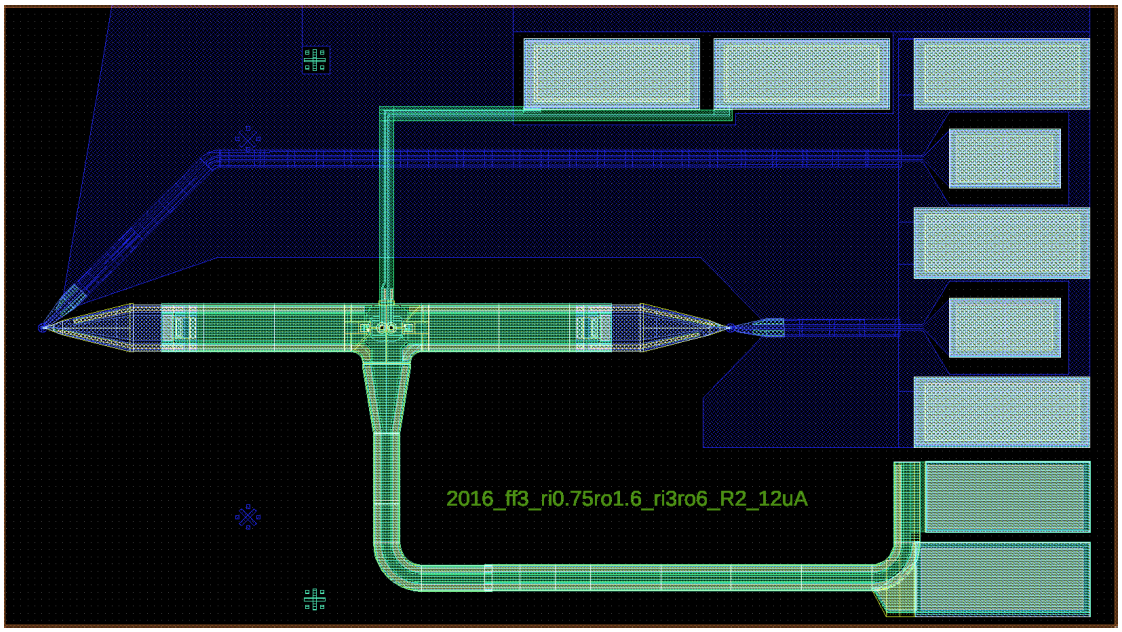

Figure 2.19: Alternate design of SQUID magnetometer with coplanar waveguide field coil using a large ground plane

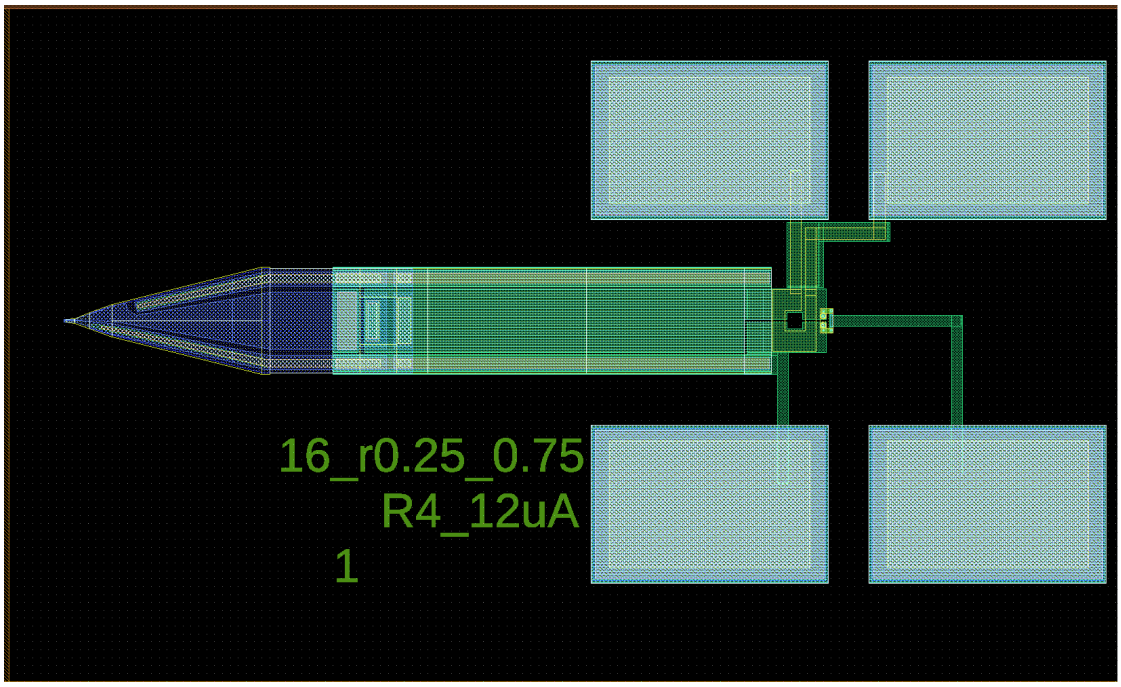

Figure 2.20: Mini SQUID Magnetometer. The pickup loop radius is 0.25 µm.

2.4.5 Mini Magnetometers

We designed SQUID magnetometers with small pickup loops on smaller chips that could be more easily mounted on a tuning fork instead of a metal cantilever that uses a capacitance measurement to measure height as described in section 2.2. The pickup loop was chosen as small as possible. Instead of all other pickup loops, the ones on these SQUIDs are simply a square slot where the width of the slot is 0.25 µm. This slot size is the smallest that Hypres would allow. No field coil was possible in this design as the pads would not fit and the superconducting shield would need to be even further back than in the 0.4 µm pickup loop SQUID magnetometers.

Instead of using the junction areas from the standard SQUID magnetometers, we used a washer SQUID design for simplicity. The junction area is identical to

the washer SQUID test structures with the washer adjusted to give the SQUID the desired self-inductance.

2.5 Conclusions and Outlook

I have described basic SQUID theory, how to use SQUIDs for scanning magnetometry, and some details about how to design SQUIDs for imaging. In the future, one could use the mini magnetometers for experiments requiring higher spatial resolution or use the coplanar waveguide field coil SQUIDs for a large variety of experiments that require GHz excitations. Additionally, careful characterization of the test structures to understand parasitics both within a 5×5 mm chip and throughout the wafer remains incomplete.

CHAPTER 3

CHARACTERIZING SQUID MAGNETOMETERS

As we measure new materials, we often probe signals and phenomena that are increasingly hard to measure. It becomes essential to identify SQUID magnetometers and susceptometers with the lowest noise floor possible for use in these experiments. Unfortunately, about a quarter of the SQUIDs we have measured have a noise floor of around $1\,\mu\Phi_0/\sqrt{\text{Hz}}$ while the rest range from $5\,\mu\Phi_0/\sqrt{\text{Hz}}$ to $20\,\mu\Phi_0/\sqrt{\text{Hz}}$. In this chapter, I describe how to measure and characterize SQUIDs as well as how to search for low noise SQUIDs.

3.1 The Dipping Probe

The dipping probe is a fast turn-around system designed to test SQUIDs. It was designed to fit in the neck of the helium transfer dewars in the Clark-PSB basement facility run by Eric Smith. The design was heavily influenced by him and his decades of experience.

3.1.1 Design

There are a few design requirements for this dipping probe. While I designed an initial version of the dipping probe, Rachel Resnick was instrumental in designing and implementing many improvements to the dipping probe under my supervision.

SQUID under vacuums

There are many dipping probes made at Cornell where the sample has direct contact with the Helium bath. This is great for robust samples, but our SQUIDs are too sensitive for such rough treatment. We need to create a vacuum chamber for the SQUID to sit inside. Because seals at low temperature are difficult, we choose a seal outside the dewar at room temperature.

We built the dipping probe around the KF-40 and KF-50 flanges. For the top of the dipping probe, we use a 6-way cross KF-50 flange. Each of the openings except the top and bottom are used for either pump lines or electrical connections. The top has a tapped piece attached to it and a threaded rod extends down into the helium dewar. The bottom opening is connected to the vacuum can.

Each of the four side openings of the 6-way cross are used for either pump lines or electrical feedthroughs. The pump line has a KF-20 flange and an over-pressure valve attached to it. The other three lines have Fischer 24 pin connectors. We chose to use Fischer connectors on the inside of the dipping probe as well to ensure that we could construct and test the wires separately from the dipping probe.

Fit inside the standard helium transfer dewars

While we could use a separate dewar with a larger neck, it is easier and more convenient to use the standard helium transfer dewars.

Historically, cans with outer diameter at 1 5/8 inch were used. These cans fit well in almost all dewars. Some dewars can fit cans at 1 7/8 inch as well. However, not all dewars fit these as the weld that connects the neck of the dewar to the

inside of the dewar is not always clean and even. Future designs should only use 1 5/8 inch outer diameter vacuum cans.

Reliable Wiring

The objective of this probe is to be a low noise test bed for SQUIDs. Thus, we need reliable low noise wiring. At the room temperature end of the probe, we use potted Fischer 24 connectors. The potting material is Stycast low temperature epoxy. We use phosphor bronze 36 AWG wires for their low thermal conductivity. They are solid core wires. To ensure their durability, we encase them in a stainless steel braid. This is essential for both noise performance and to prevent cutting wires with the sliding metal can over the baffles. To protect the wires from the braid, we encase the wires in a fiberglass sheath before sliding them into the stainless steel braid. On the cold end of the wires, we use a micro-d connector which is also potted in Stycast. The braids and fiberglass sheath can be potted inside the Stycast for maximum strength.

In an iteration of the wires, we potted resistors on a PCB into the wires. This was a horrible mistake as the potted surface mount resistors disconnected sporadically at liquid nitrogen temperatures as well as at liquid helium temperatures.

We use 3 bundles of 24 wires. One bundle is dedicated to the SQUID array amplifier. Additional wires on that bundle give access to the field coil of the SQUID connected to the SQUID array amplifier. The additional two bundles were dedicated to measuring the current-voltage characteristics of SQUIDs. Each SQUID requires 9 wires (2 point on IV, 2 wires for mod, and 3 wires for the field coil). We choose to test 4 SQUIDs using 36 total wires out of our available 48. We choose this method because we use chip carriers to hold the SQUIDs. These

chip carriers have 9 wires per side for a total of 36 wires. We only use 7 per side, choosing to break out the IV wires on the PCB. In hindsight, this was a mistake as it adds more series resistance to the IV measurement. Another large mistake was was our choice of leaded chip carriers. Leaded chip carriers are slightly magnetic as the legs are magnetic. Lead-less chip carriers are often non-magnetic. Luckily, we never observed a problem using leaded chip carriers in our SQUID measurements.

The reason we chose to test the current-voltage characteristic of only 4 SQUIDs is because only 4 SQUIDs would fit on a single chip carrier. While it is possible to fit additional SQUIDs on the second chip carrier, this chip carrier was connected to the SQUID array amplifier. Any SQUID that we test with the SQUID array amplifier would have been tested for reasonable current-voltage characteristics. Thus, any chip in the socket connected to the SQUID array amplifier would have already gone through a full IV testing procedure. In the allotted space, it was impractical to fit more than 2 chip carriers.

Low boil off rate

When operating the dipping probe, we want as low of a boil off rate as possible. This dictates the material of the dipping probe and the use of baffles. Baffles are small pieces of metal that prevent a line of sight from room temperature to 4 K. We have about 10 baffles spaced along the length of the dipping probe.

For our dipping probe, the boil off rate with the probe in the dewar was roughly equivalent to a dewar sitting in the helium facility. The stainless steel construction and phosphor bronze wires were responsible for this feature.

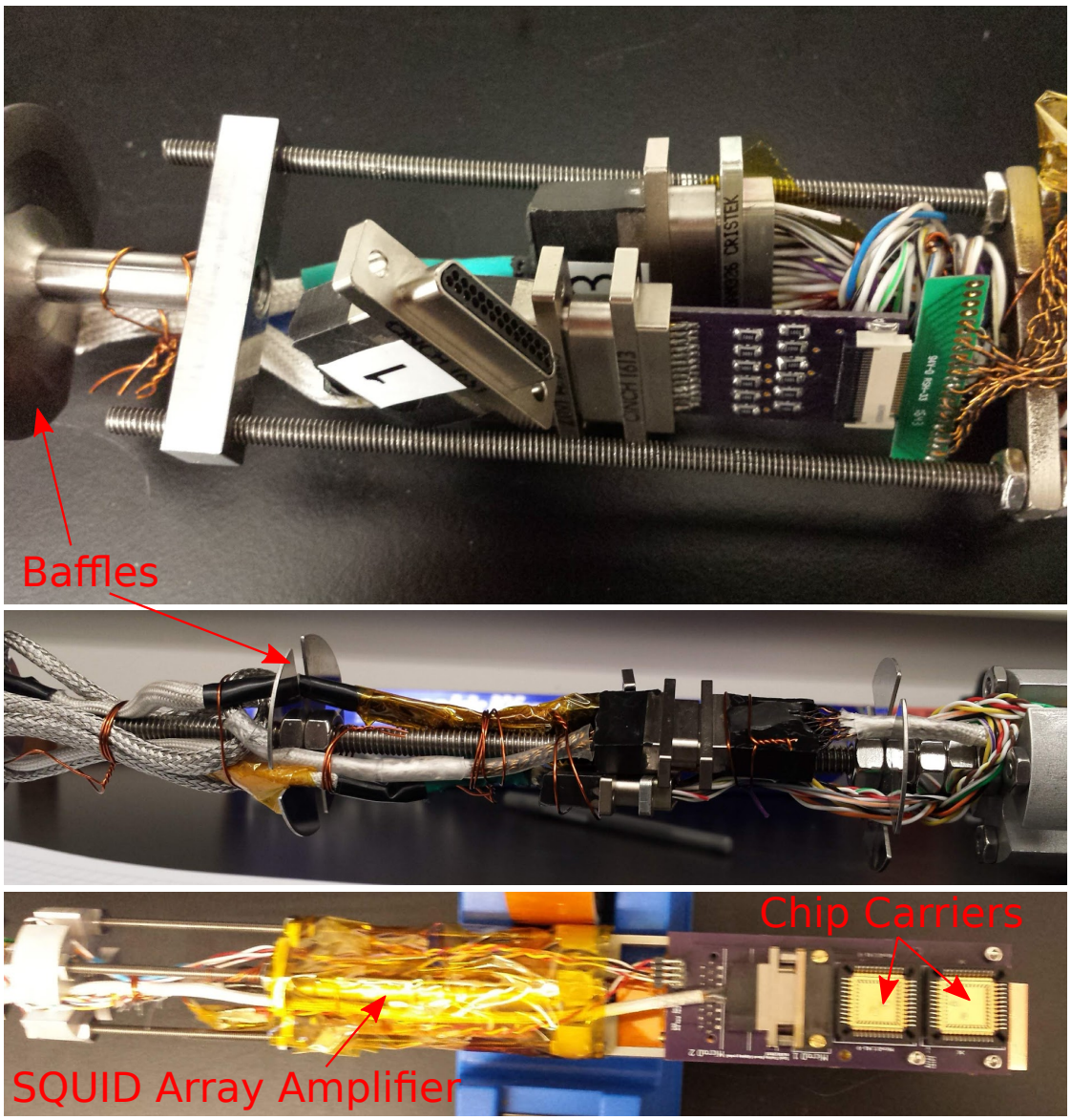

Figure 3.1: Images of the dipping probe. The baffles, chip carriers, and wiring are clearly visible. The SQUID Array Amplifier for testing SQUIDs is wrapped in Kapton tape to prevent snagging the wires leading to the chip carrier.

Over-pressure

In general, we need over-pressure valves on any cryostat to prevent a small leak when cold from turning the dipping probe into an explosive device. KF flanges will also blow if above a certain amount of pressure but we add a dedicated over-pressure valve as well.

3.1.2 Fabrication

Most of the components of the dipping probe were very easy to machine. A few key components designed by Rachel Resnick were made by external machine shops (Xometry and Protolabs). PCBs were fabricated by Oshpark. The final wiring from room temperature to 4 K was all homemade by Rachel Resnick.

The only difficult feature of the microscope to fabricate was the outer vacuum can. When Rachel and I designed the dipping probe, we used a vacuum can that was 2 inch in diameter. This vacuum can did not fit. Luckily, we were able to use a smaller can of 1 7/8 inch diameter. Another undergraduate researcher discovered that this vacuum can required very careful use as it got stuck in a dewar when improperly inserted. In certain dewars where the weld was large on one side, if the vacuum can was inserted improperly it was possible to insert the vacuum can but not be able to remove it. The probe would get jammed against the weld bead and the neck of the dewar. As it warmed, the can would expand, sealing it in place. To mitigate this problem, the Cornell machine shop turned the outside of the vacuum can as small as safe. This was done ad-hoc. This extra space allowed me to use the dipping probe for years without problem. Unfortunately, we discovered that improper usage of the dipping probe still results in jamming the vacuum can in

the neck of the dewar. I recommend modifying the design to allow for a 15/8 inch diameter can.

3.1.3 Proper Operation of the Dipping Probe

As there have been two distinct incidents where the dipping probe was lodged in the dewar, I will illustrate exactly how to safely use the dipping probe. It is worth noting that if the dipping probe had managed to completely block the neck of the dewar (with ice filling the open space), this would have created a pressure vessel that might have resulted in a very large explosion if the full dewar of liquid helium flashes to gas. Blocking the neck of the dewar is a potentially lethal mistake.

Pumping and Exchange Gas

As the cooling in the dipping probe occurs through the walls of the vacuum can, a small amount of exchange gas is necessary. In cryogen free systems, you want as high vacuum as possible as exchange gas would heat the system. We use a turbo pump to pump out the vacuum can of the sealed dipping probe after testing the wires for connectivity. We add about 1 mbar of zero grade (99.99% pure) helium exchange gas.

We pre-cool in liquid nitrogen for about 30 minutes before cooling slowly in helium vapor in the dewar.

Inserting and Extracting

Inserting the dipping probe into the helium dewar is simple but very important to do correctly. Improper insertion prevents the user from feeling if the dewar is too small (large weld bead). An improperly inserted dipping probe has a larger likelihood of getting stuck. An improperly extracted dipping probe has a large likelihood of getting stuck. A stuck dipping probe might cause the dewar to explode, the destruction of the lab, and, incidentally, the death of the user.

The essential part of the dipping probe that prevents damage to lab equipment is the *Quick Connect Coupling* from the Kurt J. Lesker Company. This coupling consists of a few metal parts and an o-ring that fits around the vacuum can and slides around the vacuum can. When tightened, this coupling forms a seal between the body of the quick connect and the vacuum can. A flange is welded onto the bottom of the quick connect coupling that is clamped onto the helium dewar. Once clamped, you can loosen or tighten the quick connect to allow the vacuum can to slide or to hold the vacuum can in place. This allows you to slowly insert the dipping probe to use the cold helium gas in the dewar to pre-cool the dipping probe and hence limit helium boil off. An image of the quick connect purchasable from Lesker is found in Figure 3.2.

For more information about how to use a dipping probe designed with a large neck size safely, please see appendix B.

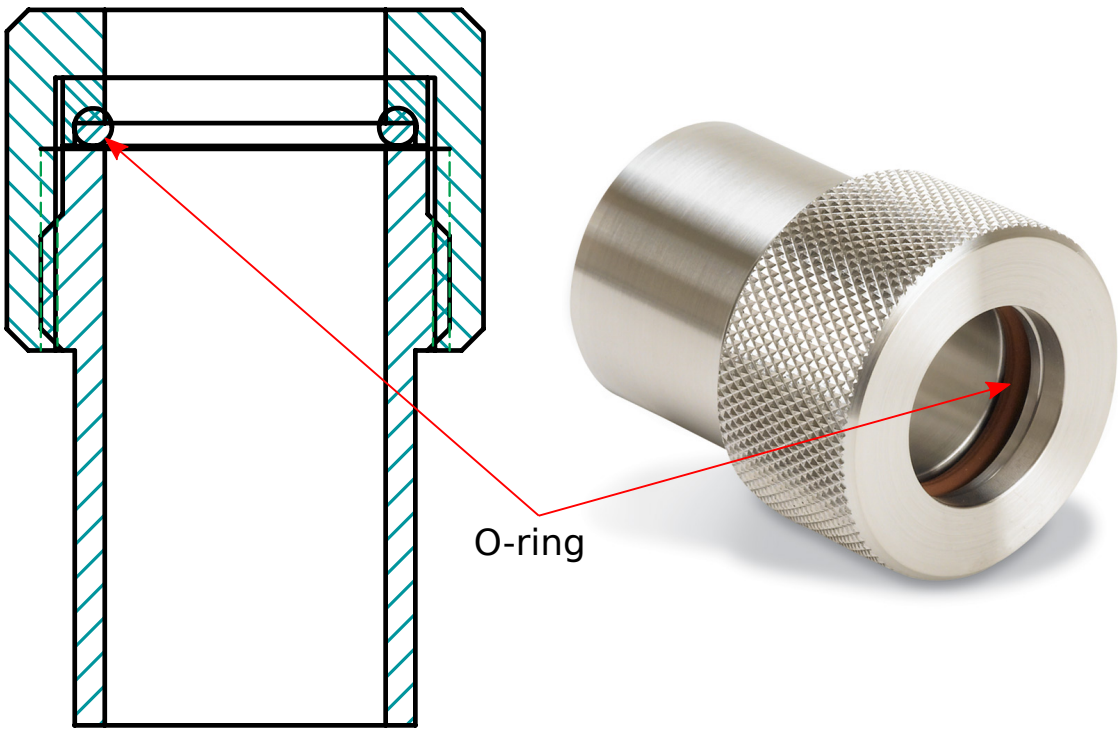

Figure 3.2: CAD drawing and image of quick connect coupling. Image and diagram from Kurt J. Lesker Company. The dipping probe vacuum can fits through the quick connect. Tightening the knurled section pushes the o-ring into contact with the dipping probe vacuum holding it in place. A flange is welded to the bottom of the quick connect that attaches to a helium transfer dewar.

3.2 SQUID Noise Measurement

The sensitivity of a SQUID to magnetic flux is bounded by the magnetic flux noise floor or noise spectrum $S_\Phi^{1/2}$ in the absence of magnetic signals. As a high noise floor requires a larger measurement bandwidth or longer acquisition time to resolve a signal of fixed strength, the time required to image a given sample and the precision in which the image is taken are limited by the noise floor $S_\Phi^{1/2}$. Thus, it is critical to minimize the magnetic flux noise of SQUIDs used for magnetic imaging experiments.

While changing the self-inductance, capacitance, junction resistance, and criti-

cal current to optimize β_C and β_L sets the designed noise of a SQUID, in practice it is challenging to reliably predict the noise of an individual SQUID from a fabrication batch. Within a wafer and between batches, the junction critical current varies, the exact properties of the superconducting layers and dielectric varies, and fabrication precision varies. This can lead to unpredictable parasitic capacitance and inductance which makes modeling noise performance challenging. The small variations are particularly significant for our SQUID designs; our designs are at the limit of what Hypres Incorporated is able to make in their superconducting fabrication foundry. Due to these variations, the noise floor and the location of the operating point to obtain the lowest noise floor varies across SQUIDs and are hard to predict.

In this section, we describe how to characterize the noise performance of individual SQUIDs as a function of the operating point in the parameter space of SQUID voltage bias and magnetic flux bias. The characterization allows us to find isolated optimal operating points with 2-5x lower noise than operating points identified using heuristic properties to manually tune the SQUID. We therefore suggest that systematic noise characterization is a valuable tool to optimize the noise of a given SQUID before starting sensitive imaging experiments.

3.2.1 Measurement Overview

Figure 3.3 shows a diagram of the measurement setup used to characterize a SQUID for use in scanning magnetometry and susceptibility. Recall that the SQUIDs used possess two magnetic flux bias lines called the modulation coil and the field coil and denoted by Smod and FC respectively. As the shunt resistors of the SQUID are typically between 2-8 Ω, we choose the bias resistor $R_{\text{bias}} \approx 0.1\,\Omega$, much smaller

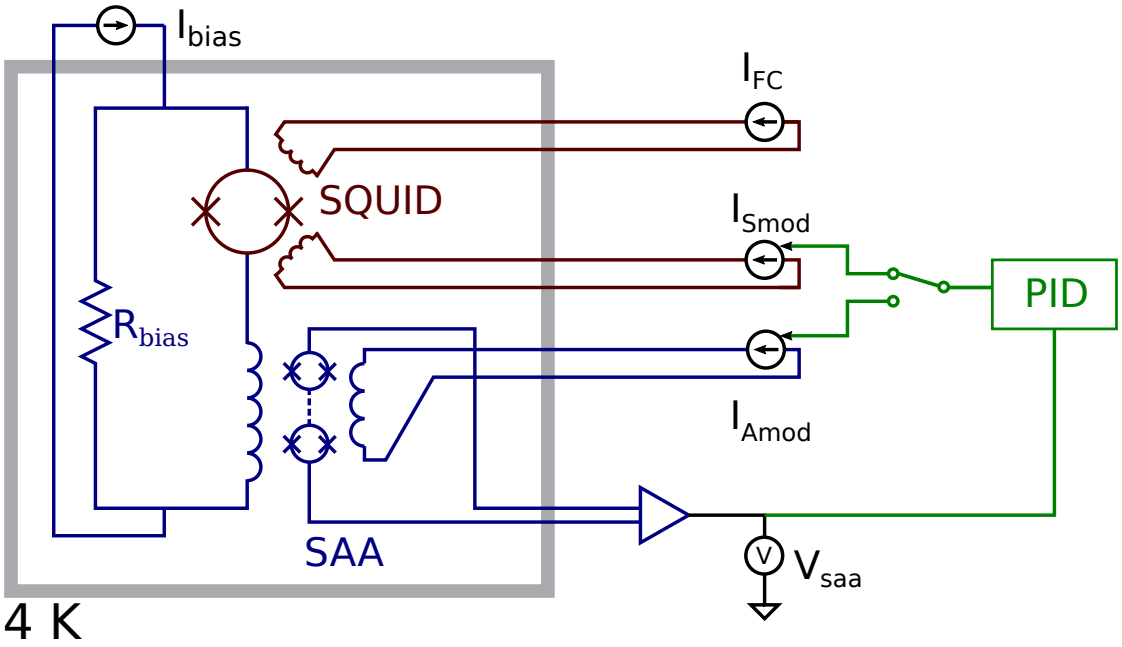

Figure 3.3: Diagram of the SQUID measurement circuit. The SQUID being tested is shown in red with the two on-chip flux bias lines. The field coil flux bias line is controlled with the current source I_{FC} and the modulation coil is controlled by current source I_{Smod}. The SQUID is voltage biased with current source I_{bias} and bias resistor R_{bias}. The SQUID array amplifier (SAA) in blue is flux biased by I_{Amod} and outputs a voltage V_{saa}. A PID loop monitors V_{saa} and controls either I_{Smod} or I_{Amod}.

than the SQUID shunt resistors. When I_{bias} is larger than the critical current of the SQUID I_c, the SQUID is effectively voltage biased as the current predominantly flows across R_{bias}.

Changes in the magnetic flux through the SQUID causes changes in the current flowing through the SQUID which we measure using a SQUID Array Amplifier. SQUID Array Amplifiers (SAA) are devices made up of many SQUIDs in series and act as extremely sensitive transimpedence amplifiers. In other words, they transform a small current signal into a larger voltage signal. The SQUID is connected in series with a line that is inductively coupled to the SAA and we readout the current through the SQUID by a voltage from the SAA. We use a StarCryo

cryogenic SAA model AR32 which consists of 32 DC SQUIDs which we current bias, flux bias, and measure using provided room temperature electronics.

The SQUID and SAA are mounted in the dipping probe system described in section 3.1.

At room temperature, the voltage across the SAA is amplified by two sets of pre-amplifiers and serves as the input signal or process variable for a PID loop to monitor. The output of the PID controller (control variable) can be either connected to the modulation coil of the SQUID or the flux line of the SAA to keep the flux constant through the SQUID (SQUID locked) or SAA (SAA locked) respectively. Maintaining constant flux through the SQUID or SAA using the PID controller is necessary because the current through the SQUID is a non-linear function of the flux in the SQUID. The flux locked loop linearizes the SQUID response and allows for quantitative measurements with large dynamic range. We report the SQUID response as a function of magnetic flux in terms of $V_{\mathrm{Amod}} \propto -I_{\mathrm{Amod}}$ for SAA locked and $V_{\mathrm{Smod}} \propto -I_{\mathrm{Smod}}$ for SQUID locked. The conversion factors depend on the operating points of the SAA and both the SQUID and the SAA respectively. These two measurement modes allow us to characterize the SQUID response to magnetic flux and the SQUID noise floor.

With the SAA locked, we can directly monitor the current through the SQUID in response to an excitation applied to the modulation coil. At fixed I_{bias}, we can sweep the SQUID flux bias with I_{Smod} and obtain the SQUID characteristic as shown in Figure 3.4. From this, we can extract the modulation amplitude and the periodicity in terms I_{Smod} which determines the mutual inductance between the SQUID and the modulation coil.

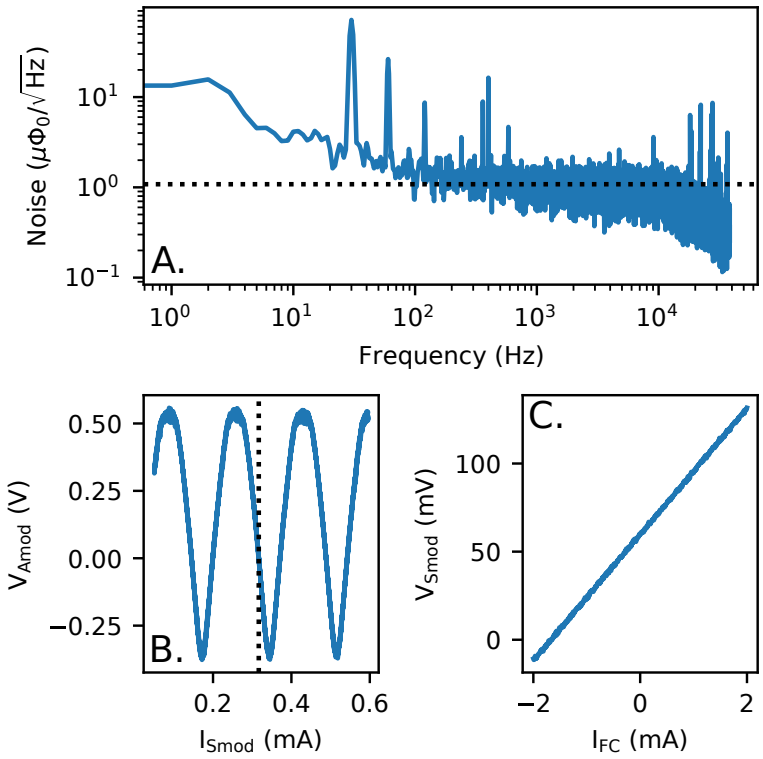

Figure 3.4: SQUID noise measurement. (A) Current noise of the SQUID amplified by the SAA measured at V_{saa}. The PID flux locked loop keeps the flux through the SQUID constant (SQUID locked). The dotted line denotes the RMS noise between 500 and 5000 Hz of about $1\,\mu\Phi_0/\sqrt{\text{Hz}}$. (B) SQUID characteristic measurement. SQUID current amplified through the SAA verses the flux through the modulation coil of the SQUID. The dotted line denotes the flux through the SQUID when the noise spectrum at (A) was taken. (C) Linearity of the field coil and SQUID signal with the SQUID locked. The SQUID is flux sensitivity at this lock point.

When we lock the SQUID, the PID controller keeps $V_{\text{Amod}} = V_{\text{saa}} = 0$ at a location where V_{Amod} decreases with increasing values of the control parameter. We can use this property of the PID controller and the SQUID periodicity to accurately measure the conversion factor between V_{Smod} and the flux through the SQUID in units of Φ_0. As an example, we lock the SQUID at the vertical dotted line in Figure 3.4B at which the falling edge of the SQUID characteristic crosses zero at $I_{\text{Smod}} \approx 0.3\,\text{mA}$. If the PID controller was reset, it would also lock at other zero crossings, e.g., near 0.15 mA causing an offset in the measurement signal that

corresponds to an integer multiple of Φ_0 of magnetic flux in the SQUID. The difference in V_{Smod} corresponds to an integer multiple of Φ_0 flux in the SQUID.

The magnetic flux noise floor of the SQUID is measured with the SQUID locked. We record V_{Smod} and apply a fast Fourier transform to obtain a flux power spectral density which estimates the noise floor at this lock point. An example is shown in Figure 3.4A. The dotted line denotes the RMS noise between 500 Hz and 5000 Hz of about $1\,\mu\Phi_0/\sqrt{\mathrm{Hz}}$. We apply a current to the on-chip field coil to confirm the SQUID is truly locked. The linear feedback response to the applied flux as shown in Figure 3.4C demonstrates the linear response of the SQUID in a PID flux locked loop. As described in section 2.3, the field coil and SQUID are gradiometric so the observed response is due to fabrication inaccuracy introducing slight asymmetries between the left and right arm of the SQUID. This asymmetry varies between different devices and is independent of lock points.

The noise performance of the SQUID depends on the applied SQUID bias current I_{bias} and the flux through the SQUID set by I_{Smod} of the lock point. In the next section, we describe the exhaustive search of the I_{bias}-I_{Smod} parameter space for the lowest noise operating point of the SQUID.

3.2.2 Searching for the Lowest Noise

The noise performance, or lowest RMS noise of a SQUID for all valid operating points, dictates the sensitivity of the SQUID and bounds the speed at which an image can be taken. The noise performance and operating point at which the lowest noise can be found differs between SQUIDs and thus must be determined for each SQUID. In this section, we systematically characterize the SQUID noise as

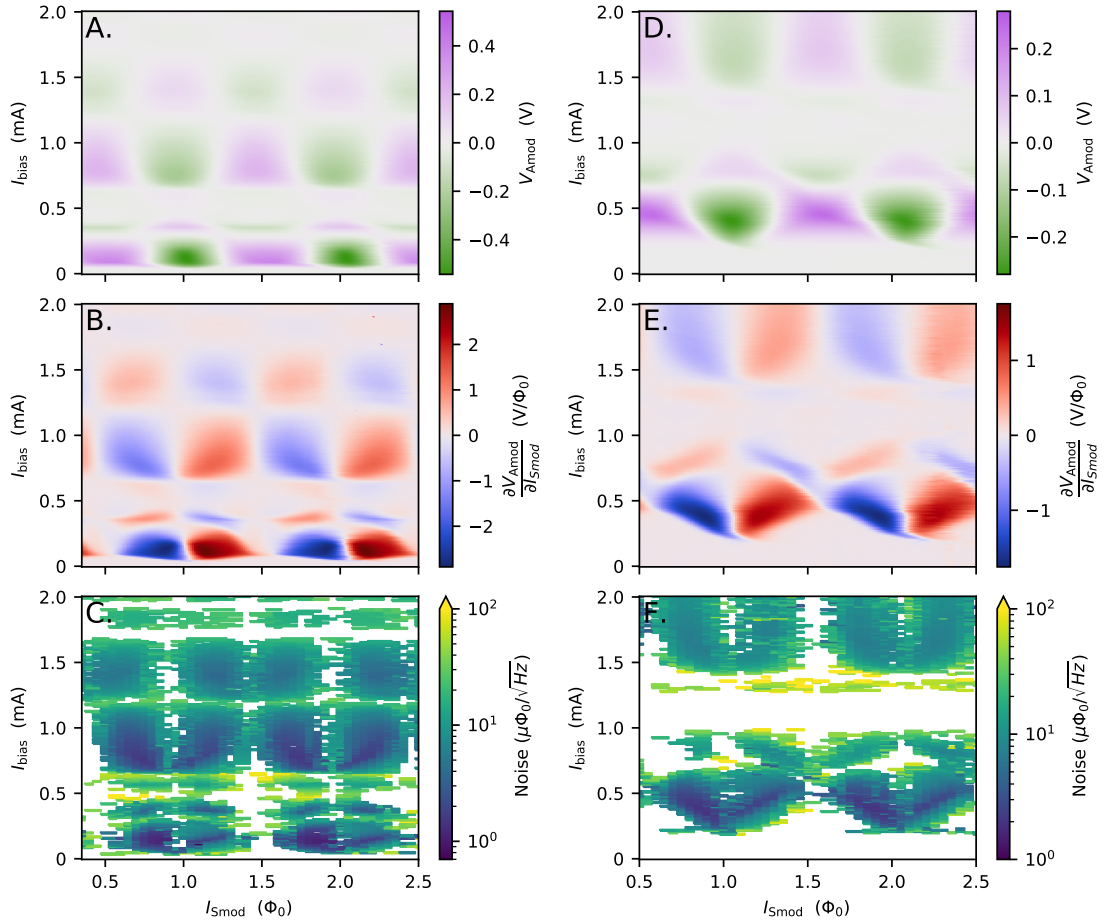

Figure 3.5: Measurements of (A,D) SQUID characteristic (B,E) the slope of the SQUID characteristic, and (C,F) the noise for the a selection of lock points at different SQUID voltage biases (plotted in terms of I_{bias}) and flux through the SQUID. White regions in (C,F) denote regions where the PID loop could not lock the SQUID. SQUIDs generally lock in regions where the amplitude of the slope of the SQUID characteristic is large. (A-C) and (D-F) are from two SQUIDs in the same 5×5 mm chip.

a function of I_{bias} and I_{Smod}. The PID controller can only lock at $V_{\text{saa}} = V_{\text{Amod}} = 0$ on the falling edge. To change the flux through the SQUID process variable of the PID controller, we add a flux offset to the SAA using I_{Amod} which shifts the SQUID characteristic up and down. By switching the polarity of the feedback wires, we can also effectively lock on the rising edge of the SQUID characteristic.

In Figure 3.5C,F we show an example of an exhaustive search for a lockpoint with optimal noise performance for two distinct SQUIDs from the same 5×5 mm chip. The color represents the root mean square (RMS) flux noise in the bandwidth of 500 Hz to 5000 Hz. The SQUID characteristic at each value of I_{bias} is shown in Figure 3.5A,D and its numerical derivative with respect to I_{Smod} is shown in Figure 3.5B,E. The PID controller cannot lock the SQUID in regions where the slope of the SQUID characteristic is zero which explains the large white regions in Figure 3.5C,F where the slope is near zero. We confirm that the SQUID at all lock points are flux sensitive by threading flux through the SQUID using the on-chip field coil as depicted in Figure 3.4C. Note that the conversion between I_{FC} and SQUID response is independent of the SQUID lock point. We use this to ensure that the lock points are valid. Lock points where the conversion factor differs from the average by some small threshold are excluded. We convert I_{Smod} to Φ_0 using the periodicity of the SQUID characteristic. The characteristic and its derivative, as plotted in Figure 3.5A,B,D,E, are smoothed to eliminate outliers due to noise.

We plot the noise measurements two different SQUIDs from the same 5×5 mm chip to emphasize the variation of noise floor and lock point locations between two SQUIDs from generally the same location. Note that both the SQUID characteristic and the lock point locations are very different between the two SQUIDs. Through experience, we have identified some heuristic properties of the SQUID characteristic to determine regions where the SQUID noise should be low.

Typically, we rely on heuristic properties of the SQUID characteristic to choose the lock point prior to starting an imaging experiment. The maps of SQUID noise as a function of tuning parameters in Figure 3.5(C,F) allow us to evaluate the reliability of these heuristics. Three such heuristics are: (1) the peak-to-peak

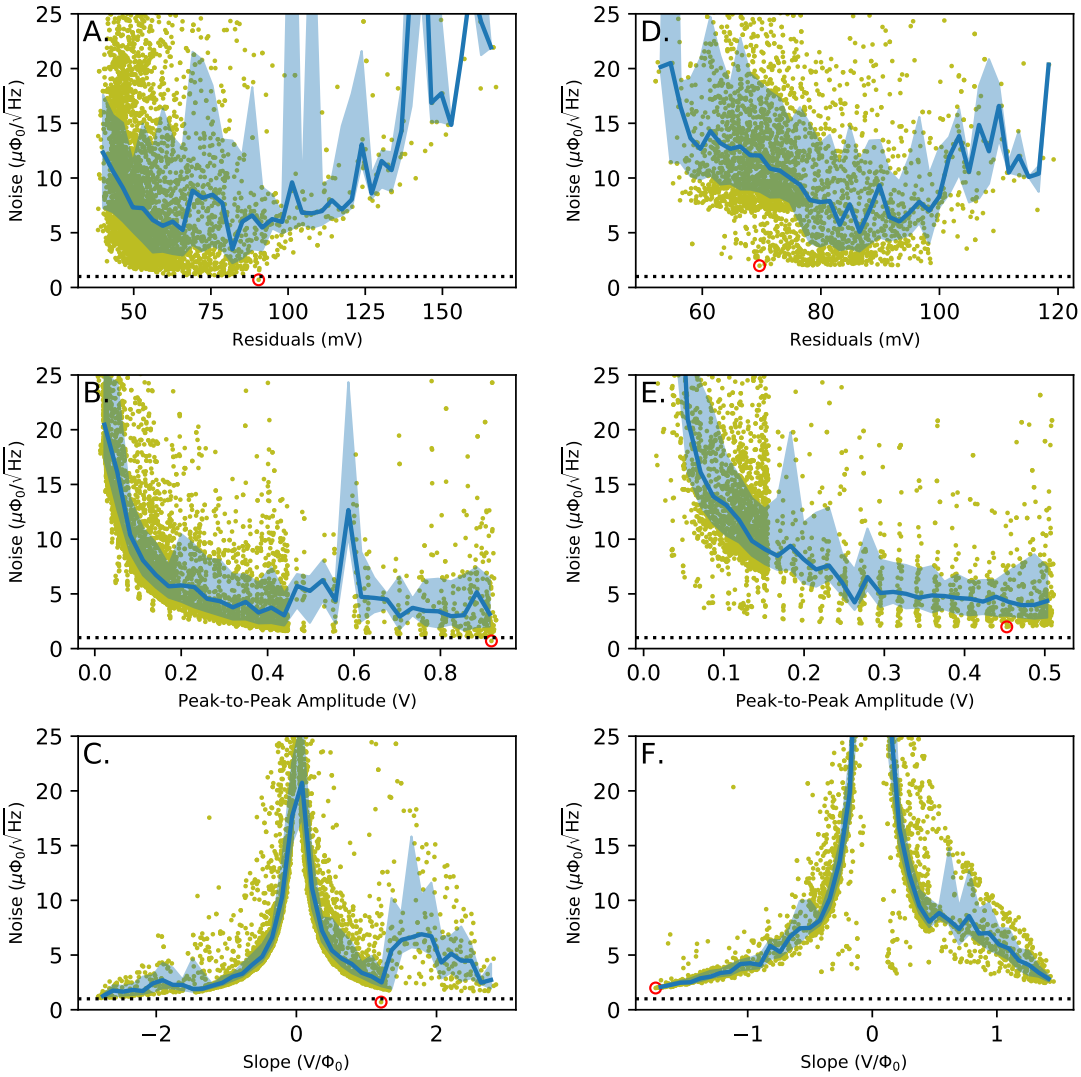

Figure 3.6: SQUID noise heuristic predictors with data in green, data median in blue, and the 25-75 percentile region in light blue. (A,D) SQUID noise verses RMS difference of smoothed SQUID characteristic and raw SQUID characteristic. (B,E) SQUID noise verses peak-to-peak amplitude of smoothed SQUID characteristic. (C,F) SQUID noise verses slope of smoothed SQUID characteristic. Red circle denotes lowest noise data point. (A-C) and (D-F) are from two SQUIDs in the same 5×5 mm chip and correspond to Figure 3.5 (A-C) and (D-F) respectfully.

amplitude of the SQUID characteristic, (2) the slope of the characteristic at the lock point, and (3) how noisy the characteristic appears. The latter is dependent on the bandwidth and speed at which the characteristic is acquired but, as we hold bandwidth and sampling rate constant throughout these measurements, can be meaningful as a relative measure when changing tuning parameters. Here, we quantify how noisy the characteristics appear by the residuals after subtracting a smoothed version of the characteristic. We plot the measured SQUID noise verses these heuristics in Figure 3.6. Subplots in Figure 3.6 (A-C) corresponds to the SQUID measured in Figure 3.5 (A-C) while Figure 3.6 (D-F) correspond to the SQUID measured in Figure 3.5(A-C). The green points represent unique measured lock points. The points are binned along the x axis and the blue line represents the median of the bin while the shaded blue region represents the 25-75 percentile region, i.e. a lock point within the bin has a 50% probability to have noise within the shaded region or a 50% chance of having noise less than the dark blue line. We plot the median and 25-75 percentile regions instead of the average and standard deviation because the median is more robust to outliers and there is no guarantee that the data is Gaussian distributed. We notice in Figure 3.6C that the noise of lock points is higher around $+1.75\,\mathrm{V}/\Phi_0$ which we can see in Figure 3.5B and C. The discretization in Figure 3.6(B,E) is due to the large spacing of I_{basis} where the SQUID characteristic changes rapidly.

Choosing a lock point where the SQUID characteristic has a large slope is generally better than areas where the slope is small as demonstrated in Figure 3.6(C,F). Large peak-to-peak SQUID characteristic amplitude also suggests a low noise lock point but the uncertainty is larger and the median noise is higher than if we used the large slope heuristic. The residuals suggest that choosing a lock point with very high residuals leads to poor noise performance. However, there

are many low residual lock points that have very poor noise performance. Note also the noise performance of both SQUIDs follow the same heuristics.

While the correlations visible in Figure 3.6 suggest that the heuristics are generally helpful to find low noise operating points, a systematic characterization of the noise reveals the optimal operating point cannot be found by relying on heuristics. In Figure 3.6, we circle (in red) the lock point with the lowest noise. In Figure 3.6C, the lowest noise point does not have the largest slope. It has the largest peak-to-peak amplitude and lies and the minimum of the median line in Figure 3.6A but we believe this is a coincidence. In the other shown SQUID, the lowest noise point has the largest amplitude of slope, but does not have the largest peak-to-peak amplitude nor lies at the minimum of the median line of the residuals.

The simple heuristics do not identify the lowest noise lock points and no simple, hand programmed combination of these heuristics are significantly better at locating low noise lock points.

3.2.3 Learning to Find Low Noise Lock Points

Typically, we rely on heuristic properties of the SQUID characteristic to find the lowest noise lock point for a given SQUID. While the heuristics described in the previous section generally are useful for finding low noise lock points, following these heuristics do not always give the lowest noise lock point. One method to determine if it is possible to find a combination of heuristics to predict the location of low noise lock points is to use machine learning to predict low noise lock points given quick measurements as in Figure 3.5A,B,D,E.

The goal of the machine learning algorithm is to predict the closed loop SQUID

noise (SQUID locked) given any data recorded with the array locked. Specifically, we wish to predict the SQUID noise for every pixel in the I_{bias}-I_{Smod} parameter space given data for only that pixel. We do not directly use information from neighboring points. An example of the values we wish to predict are the SQUID noise in Figure 3.5C,F while examples of the data is in Figure 3.5A,B,D,E. For each data point, we also include other features such as peak-to-peak amplitude of the SQUID characteristic, residuals, and the coefficient of determination of a linear fit to a small region of the SQUID characteristic at the lock point.

Our dataset is split into a training and validation set where the validation set has data points drawn from an unseen SQUID. This prevents our machine learning algorithm from memorizing the noise of a SQUID. We used a total of 3 SQUIDs; 2 were used for training and the remaining SQUID was used for validation. The two SQUIDs in training were from different $5\times5\,\text{mm}$ chips. All of the SQUIDs had very different SQUID characteristic maps and different regions of lowest noise.

Originally, we trained regression models to predict the real number value of the SQUID noise. However, these models gave extremely poor accuracy and rarely identified regions of low noise. To make the task easier, we binned the noise values so we could perform multi-class classification instead. The bin sizes and their labels are found in table 3.1. In general, we care about locating SQUIDs with less than $10\,\mu\Phi_0/\sqrt{\text{Hz}}$. In the future, we will reduce this bin size to identify SQUIDs with less than 2 or $5\,\mu\Phi_0/\sqrt{\text{Hz}}$. The ground truth binned labels for a SQUID in the validation set is shown in Figure 3.7A.

We first tried using classic linear classifiers such as logistic regression, SVM, and perceptron. The most successful of the linear classifiers was logistic regression. The predictions for the best logistic regression model on a SQUID in the validation

Bin Label	Bin Start	Bin End
0	$0\,\mu\Phi_0/\sqrt{\text{Hz}}$	$10\,\mu\Phi_0/\sqrt{\text{Hz}}$
1	$10\,\mu\Phi_0/\sqrt{\text{Hz}}$	$50\,\mu\Phi_0/\sqrt{\text{Hz}}$
2	$50\,\mu\Phi_0/\sqrt{\text{Hz}}$	$100\,\mu\Phi_0/\sqrt{\text{Hz}}$
3	$100\,\mu\Phi_0/\sqrt{\text{Hz}}$	Max
4	SQUID cannot lock	

Table 3.1: Bin labels for multi-class classification of SQUID noise. Bin "3" contains all noise points with more than $100\,\mu\Phi_0/\sqrt{\text{Hz}}$. The points labeled "4" did not lock, which shows up in Figure 3.5C,F as white or empty pixels. All noise is measured as RMS between 500 and 5000 Hz.

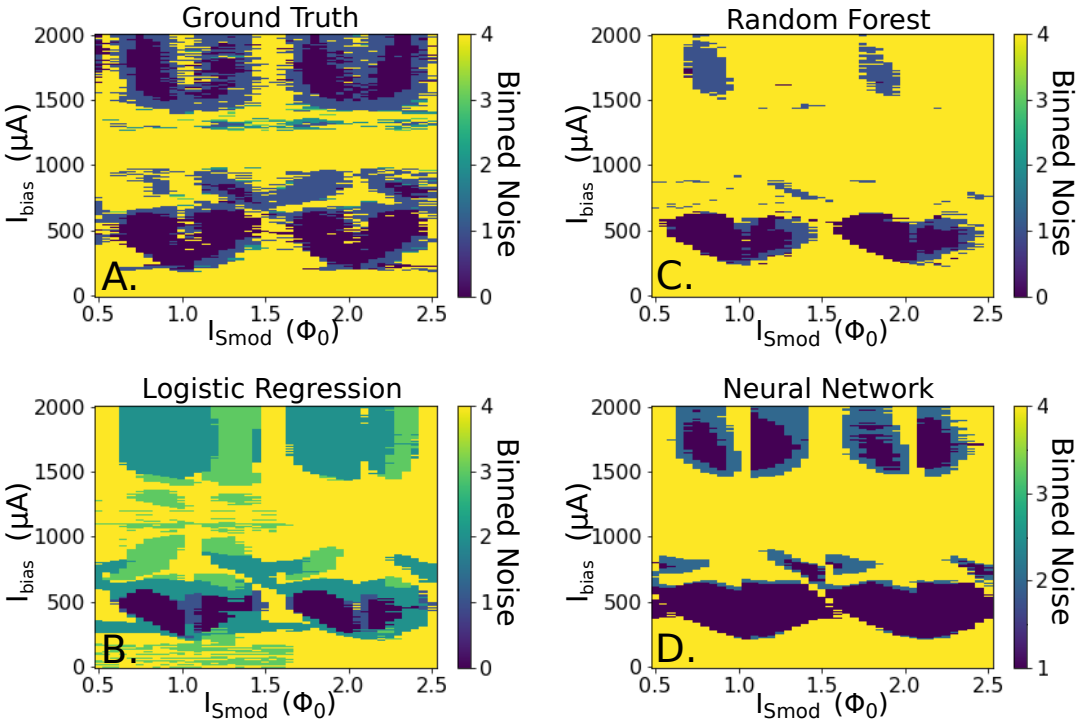

Figure 3.7: Predicting SQUID noise with Machine Learning. Binned SQUID noise for the SQUID plotted in Figure 3.5D-F and Figure 3.6D-F. (A) Binned ground truth labels of the SQUID. (B) Predicted labels from a Logistic Regression, (C) a Random Forest, and (D) a Neural Network model.

set is plotted in Figure 3.7B. We used a random search to tune the L2 regularization strength and stopping tolerance. Unfortunately, logistic regression mis-identified the upper lobe with I_{bias} between 1500 and 2000 µA as a high noise region instead of a low noise region. However, unlike SVM or perceptron, the logistic regression algorithm was generally able to identify regions where the SQUID could not lock.

We also tried random forest algorithms where we tuned the number of trees in the forest and the depth of each tree. While this algorithm characterized the upper lobe as a medium (label 1) noise region, it misclassified large regions as areas where the SQUID is not able to be locked. The predictions for the best random forest model are plotted in Figure 3.7C.

Finally, we trained a neural network to learn this task. We used a deep network made up of 3 fully connected layers of size 512, 256, and 128. Between each layer, we performed dropout [67] and batch normalization [30] between each fully connected layer. We again performed a random search to determine the best hyper parameters. The network with lowest validation error had batch normalization, batch sizes of 2048 and used the Adam optimizer [33] The network with largest validation error did not use batch normalization and used stochastic gradient descent (SGD). We plot the predictions for the best neural network in Figure 3.7D. We notice that the neural network accurately predicts the locations of the low noise regions and does a reasonable job at predicting where the SQUID cannot be locked.

We plot the validation error for the best neural network, worst neural network, best random forest and best logistic regression models in Figure 3.8. Note that the validation error metric is "exact match", which means that the error for a given point is 0 if and only if it is properly labeled. The different models evaluated are

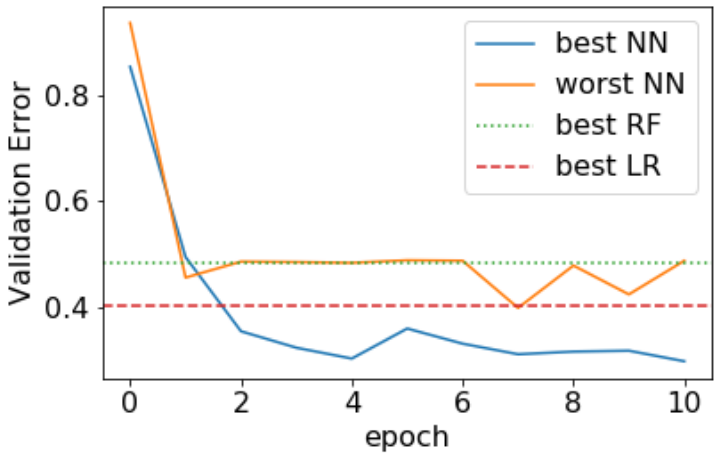

Figure 3.8: Validation error for predicting binned SQUID noise. The validation error for the multi-class classification task uses exact match. We plot the validation error for the best neural network, worst neural network, best random forest and best logistic regression model. The models are selected from a set of models generated by a random search over their respective hyperparameters.

from the random hyperparameter search. We see that the best neural network is dramatically more accurate than the best random forest or logistic regression model but the worst neural network is somewhere between. We also note that the logistic regression model is better than the random forest model. One possible explanation for this is that the different SQUIDs have very different ranges of values for the slope or amplitude of SQUID characteristics. Random forest creates decision trees based on splitting on one of these real valued features and the large range of values might be making this difficult.

Another possible explanation for the poor performance of random forest and logistic regression is that the model to describe how to find low noise lock points is very complicated; logistic regression and random forest might not have sufficient predictive power or complexity to express an accurate model. However, one should be cautious when generalizing this result as we used a total of 3 SQUIDs in this procedure.

3.3 Conclusion and Outlook

I have described the experimental apparatus and methodology for characterizing the noise floor of SQUIDs in a reliable and systematic method. However, the systematic approach for characterizing SQUIDs requires a little less than one day per Φ_0 period of the SQUID parameter space explored. Besides reducing the number of periods measured, there are other ways to speed up the search. We could exclude lock points from the search that have values of the heuristics that strongly correlate with poor noise performance. In particular, we propose to exclude points with a low slope of the SQUID characteristic. For the SQUID we present, a conservative choice would be to exclude all points with a slope lower than $0.6\,\mathrm{V}/\Phi_0$ which corresponds to excluding 80% of all possible lock points. We also measured the conversion from V_{Smod} to Φ_0 at each data point by observing a jump in the feedback voltage. We estimate that the search could be shortened to a few hours if we implement all of these modifications. We worked on finding heuristics that would allow us to predict low noise regions, but we were not successful. I also explored using machine learning to find these low noise regions but was not successful. I believe that if there was more training data, an far more accurate algorithm could be created. However, I still believe that the model created with just these two SQUIDs would prove useful if one wanted to characterize SQUIDs without human intervention. The model as of now seems to be better than trying to lock the SQUID in random locations in the I_{bias}-I_{Smod} parameter space. In future dipping probes where more than one SQUID can be measured in a single cooldown, a machine learning algorithm could prove very useful for characterizing SQUIDs.

CHAPTER 4

DESIGNING AND BUILDING A SCANNING SQUID MICROSCOPE

Scanning SQUID microscopy is a well established technique. It was first designed in the early 1990s [50, 72, 47, 6, 36, 35] in cryostats with liquid cryogens. There have been many advancements in scanning SQUID microscopy [13, 19, 71, 68, 64, 74] over the last 40 years. Before our microscope, however, there was never a scanning SQUID microscope in a cryogen-free dilution refrigerator. While there had been scanning probe microscopes in cryogen-free dilution refrigerators, they often used spring stages to achieve low vibrations. In this chapter, I describe why a cryogen-free microscope is attractive, the requirements we had for our microscope, and the design our microscope.

4.1 Reasons to go Cryogen Free

There are both financial and practical reasons why one might decide to build a microscope in a cryogen free system instead of using liquid cryogens.

First, A cryogen-free DR is attractive due to rising prices and uncertain supply of liquid helium. For a microscope, we often wish to stay cold for months and interruptions in Helium supply could be quite annoying. While a wet system with a gas bag and pulse tube reliquifier can be implemented, this is a lot more cumbersome and requires a lot more space than connecting experimental plates directly to the pulse tube.

Second, a cryogen-free system is a lot more convenient to use. In a wet system,

besides those with a gas bag and reliquifier, liquid helium transfers are required to refill the cryostat. Most scanning probe microscopes cannot image while filling the cryostat as filling introduces a lot of vibrations due to boiling helium. Another important consideration that has only become more obvious because of Covid-19 restrictions is that a cryogen-free system can be operated completely remotely because of the lack of liquid cryogens. Additionally, cryogen-free systems are effectively turn-key and require less training to safely use than wet systems. Most of the operations are fully automated in modern cryogen-free systems like our Bluefors system. We have never had any incident with our dry systems that endangered our cold electronics, samples, or graduate students that was caused by the cryostat. In the same time, we had a few incidents with our single wet system. Wet systems are perfectly safe if everyone is careful and aware, but dry systems are far more fool-proof.

Finally, a cryogen-free system often have very large sample volumes as they do not require a liquid Helium bath to envelop the inner vacuum chamber. While there are liquid Helium cryostats with large volumes, these tend to use a lot of helium and are custom made. The large sample volume allows us to run multiple experiments simultaneously and fit amplifiers and filters without custom design.

However, cryogen free systems come with a few challenges or drawbacks. First, a wet cryogen system can be cooled faster. Not only will the liquid Helium bath cool the microscope faster than a pulse tube, one could pre-cool with liquid nitrogen to get below 77 Kelvin. Some dry systems have the ability to pre-cool with liquid nitrogen but it is not as simple as a wet system. Second, wet systems can have more cooling power at 4K for the same reason that they can be cooled faster. However, we have found no problems with the cooling power of our cryogen free

system. Finally and most importantly for a scanning probe microscope, there are significantly more mechanical vibrations in a cryogen-free system from the cryocooler or pulse tube. During the pulse tube cooling cycle, high-pressure helium gas is pushed in and out of the pulse tube at a frequency of approximately 1 Hz. Along with this 1 Hz noise source, there are also a number of higher harmonics caused by various motors in the pulse tube. Isolating the pulse tube mechanically from the system is extremely difficult as you need a solid mechanical link to ensure good thermal conductivity. While there are a few cryostats that use bellows and helium-3 to create a thermal link without any mechanical contact besides the bellow, most dry cryostats use copper braids to decouple the pulse tube from the experimental plates.

4.1.1 Prior Work

There are many reports of scanning probe microscopes in 4 K systems including a tuning fork AFM [59], a NV center microscope [58], and a scanning SQUID microscope[4]. However, only a few scanning probe microscopes have been reported that operate in cryogen-free DRs, including a scanning gate microscope [56] and a scanning tunneling microscope [14]. In both cases, custom spring stages were used to mechanically isolate the microscope from the cryostat.

Scanning SQUID microscopy has been implemented in two different types of cryogen-free cryostats with base temperatures of ∼3–4 K, but not in a cryostat reaching lower temperatures. In Ref. [64], the authors used a cryostat with built-in mechanical isolation between the cryocooler and the cold plate on which the microscope is mounted. In Ref. [4], the microscope was placed in a pulse tube based cryostat similar to our own but without the dilution unit and associated cold

plates. A custom spring stage was used to significantly reduce vibrations in the microscope. However, such mechanical isolation often comes at the cost of reduced thermal anchoring: a less rigid mechanical connection implies less thermal conductivity between the microscope and the cold plate. A weak thermal connection can prevent rapid measurements over a large scan window due to the heat piezoelectric elements generate while moving. This is particularly challenging when operating near the base temperature in a DR due to the limited cooling power. In addition, a spring stage is difficult to combine with mechanically rigid low-loss coaxial connections to either the SQUID or the sample. Such connections are necessary to implement a dispersive SQUID readout [26, 21, 43] or to deliver gigahertz and fast rise time excitations to a sample. Combining a spring stage with a superconducting magnet is challenging as well, since a strong magnetic field may exert forces on the microscope and causes undesirable motion [57]. In principle, scanning probe microscopes are only affected by relative motion of the probe and the sample. This suggests that a rigid microscope in which the probe and sample move together in response to the pulse-tube-induced vibrations offers an alternative to using spring stages.

4.2 Bluefors Cryostat

We use a Bluefors BF-LD 400 DR with a base temperature of 10 mK and 400 µW cooling power at 100 mK. Cooling to ∼3 K is provided by a Cryomech PT-415 pulse tube cooler implemented with a remote motor option. A superconducting vector magnet from American Magnetics Inc. can apply 6 T perpendicular to and 1 T in any in-plane direction of the sample. A few modifications designed and implemented by Bluefors reduce the vibrations of the mixing chamber plate. The DR

rests on two nested aluminum frames to reduce the mechanical coupling between the pulse tube cooler and the interior of the cryostat. All cold plates, vacuum cans, and the superconducting magnet are supported by the inner frame while the pulse tube and related components are mounted onto the outer frame. The two nested frames are only connected via an edge-welded stainless steel bellows to maintain vacuum and via copper braids inside the vacuum chamber to thermally link the cold plates and the pulse tube. The top plate of the cryostat is bolted to heavy metal plates (approx. 400 kg). These metal plates rest on air springs mounted to the inner frame. The remote motor head of the pulse tube, which is a source of vibrations, is housed in a sound isolation box that is mounted on the outer frame and connected to the pulse tube by high- and low-pressure flexible lines. The nested frames, heavy metal plates, air springs, copper braids, and the pulse tube are depicted in Figure 4.1. We implemented a linear motor driver for the cold head motor as suggested in Ref.[56]. The high-pressure lines connecting the remote motor head and the compressor are run through thick fiberglass sleeving to reduce the acoustic noise in the lab. The still pump line is passed through a concrete block between the cryostat and the gas handling cabinet. The gas handling cabinet and the compressor are in a utility space that is well separated from the lab space.

4.3 Designing the Microscope

At the time of design, this scanning SQUID microscope is the first that reaches 50 mK and does not contain a spring stage.

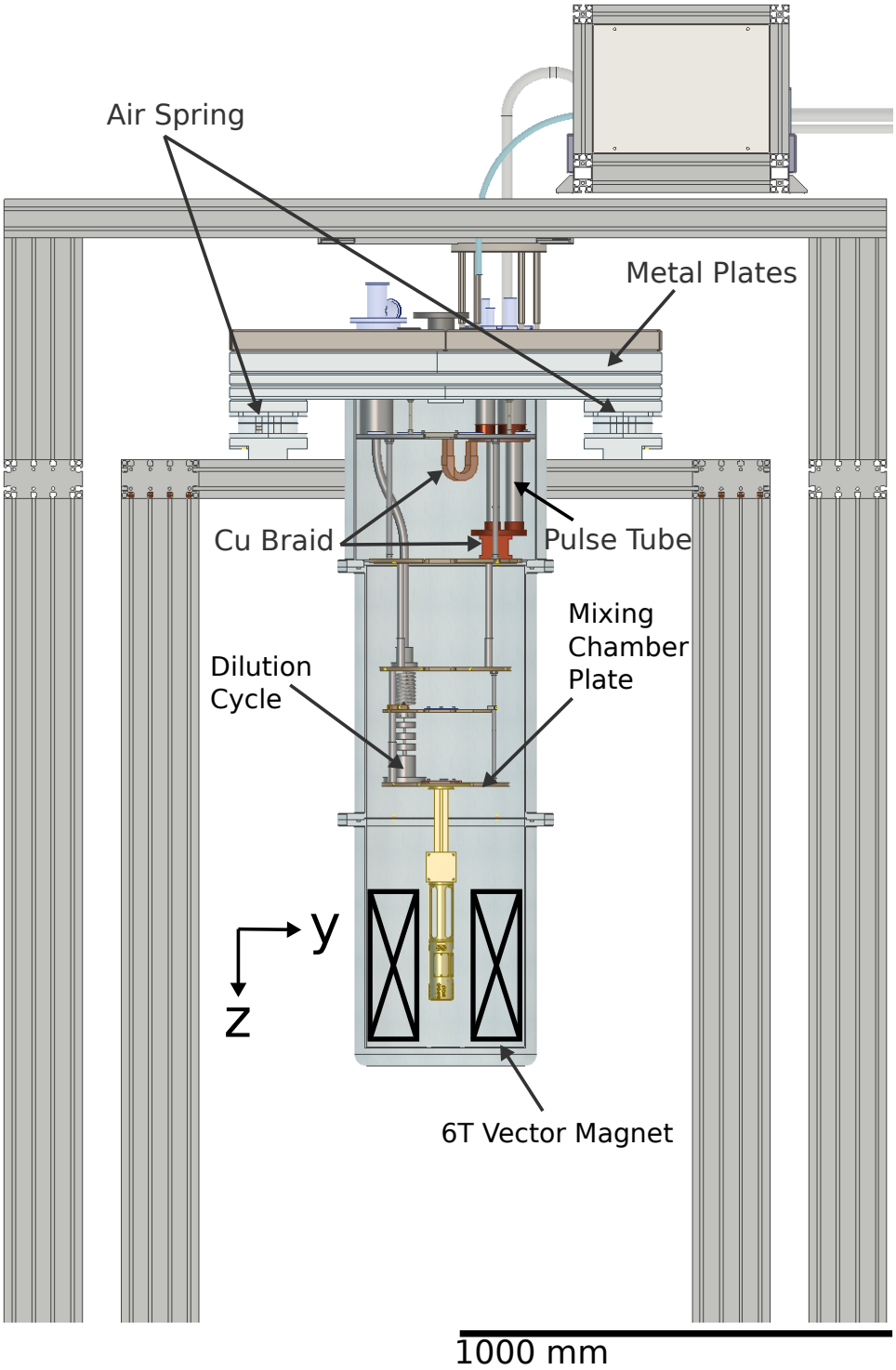

Figure 4.1: Diagram of the Bluefors cryostat with microscope. The air springs and flexible copper braids are identified as well as the pulse tube that causes the vibrations. The dilution cycle allows the mixing chamber plate to reach 10 mK. The sample lies at the center of the vector magnet.

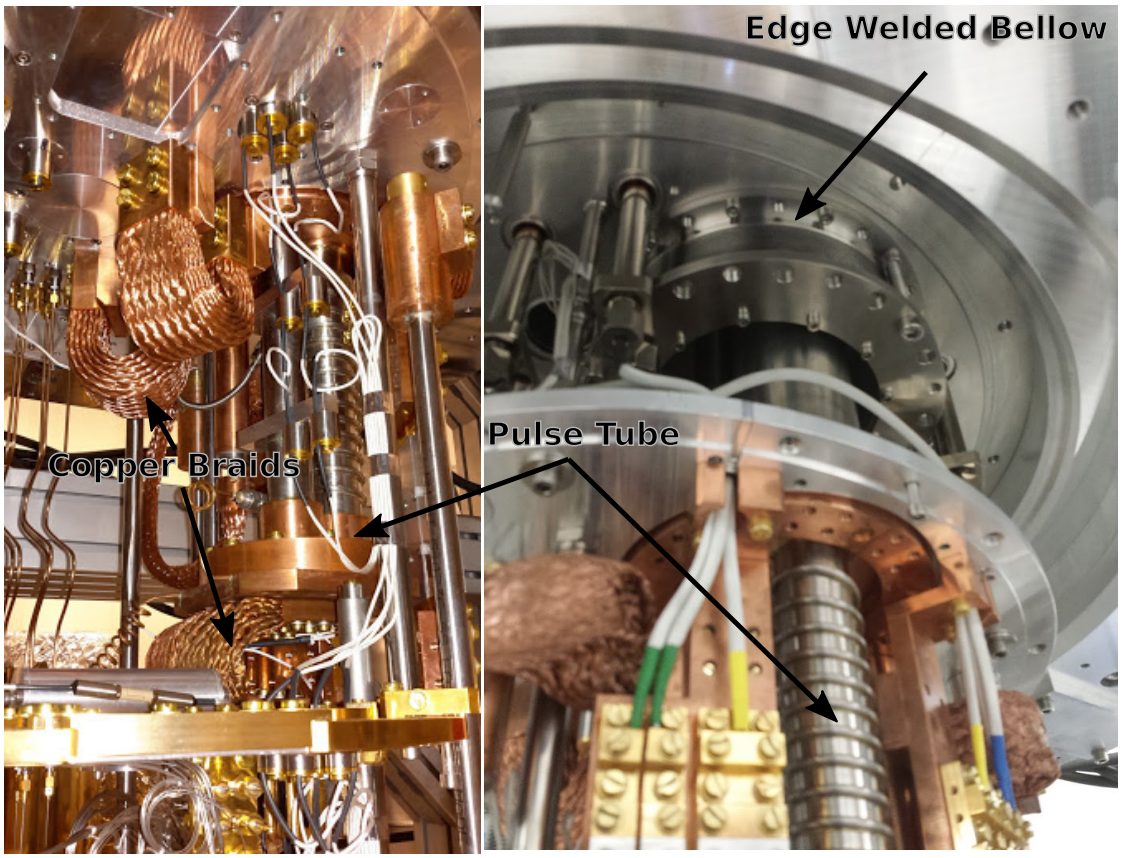

Figure 4.2: Images of the pulse tube, edge welded bellows, and copper braids of the Bluefors cryostat. The pulse tube is the source of vibrations while the copper braids and edge welded bellow attempts to reduce the vibrations at the 4 K plate.

4.3.1 Design Considerations and Constraints

There are a number of important design considerations for building a scanning SQUID microscope in our dilution refrigerator. I have listed the ones we used to design our microscope in order of most important to least important.

Scanning Considerations

The microscope must be able to perform SQUID imaging. This means that it must contain both our piezo scanner and our Attocube positioners and enough

room for the positioners to move freely. The sample also must be close enough to the SQUID such that the SQUID can touch the sample.

We wish to have the largest possible XY area to place our sample, so we chose the Attocube ANP311 positioners. These were the Attocube positioners with largest range that would fit inside the bore of our magnet. They were also designed to be stiffer than the ANP101 series.

Space Constraints

The entire microscope must be able to fit inside the bore of our magnet. The bore has a diameter of about 68 mm. Combined with the large Attocube positioners, we are left with very little room for the metal of the microscope.

Thermalization Considerations

Considering that the microscope is contained within a 1 K radiation shield and the microscope itself is bolted to a coldfinger that is very securely bolted to the mixing chamber plate, we are not very concerned with thermalizing the SQUID well. Instead, we need to prioritize thermalizing the sample as well as possible.

Usability Considerations

A very large problem when designing this microscope was to ensure that we had enough line of sight to the SQUID and sample to properly align the SQUID to the sample. It is necessary to position the SQUID chip such that the front pickup loop of the SQUID makes contact with the sample first. If not, the SQUID may

never get close enough to the sample. This requires aligning the SQUID by hand using a camera and a zoom lens. We know we needed front and side views of the SQUID and sample. However, we did not know exactly how much space we needed nor exactly what sort of angles we needed. While we could make educated guesses using our existing 4 K scanning SQUID microscope in the Montana system, its hard to exactly say what solid angle we require to be open.

Another usability concern that I prioritized was the speed at which we could change the sample. Ideally, the SQUID we use should be fairly robust and would last a number of cooldowns. Each cooldown, however, we would change the sample. So, I wanted to make changing the sample as easy and quick as possible.

Finally, I wanted the setup to be as fool-proof as possible. Often, we are going to be closing the cryostat late a night so it can pump or cool overnight. As such, I wanted to design to microscope so you did not need to have very steady hands or need to be extremely careful.

Rigidity

We try to make the microscope as rigid as possible. Designs that are thermally conductive are often rigid. We use many large bolts and large geometries known to be rigid such as triangles and cylinders. Covers for the necessary access and wiring windows are made to try and reduce the vibrational modes from these openings.

Wiring Considerations

Wiring is a huge part of the microscope. We want the wires to be protected from abrasion and positioned in a neat and tidy way. We want the wires to be able to

be easily disconnected.

4.3.2 Microscope Design

Full drawings of the microscope and coldfinger are available at Ref [46].

The microscope consists of a cold finger and the microscope housing. Each is machined from a single block of copper and bolted together on machined flat, keyed surfaces using four large 1/4-20 brass screws. All fasteners in this design are brass because brass contracts more at low temperature than copper, so the interface only gets tighter as the cryostat cools. The cold finger is mounted to the mixing chamber plate using six 1/4-20 brass screws. The outer diameter of the housing is set by the 68 mm diameter bore of the superconducting magnet. The exact center of the magnet bore is offset from the hole for the top loading probe. This offset is accounted for by copper piece that bolts the coldfinger to the mixing chamber plate. The length of the cold finger is chosen such that the sample is positioned at the center of the magnet. Windows in the microscope housing (see Figure 4.3) can be opened by removing copper plates to get visual access when aligning the SQUID to the sample at room temperature.

All wiring runs along the cold finger and enters the microscope housing through a box at the middle of the cold finger. This box has two removable plates, which allows us to include and change desired wiring feedthroughs. A light tight gold plated copper can (not shown) is bolted below the wiring feed-through box on the cold finger. This design allows to in principle route fully filtered and shielded wiring to the microscope. All machined parts are gold-plated.

The SQUID is mounted on a home-built piezoelectric scanner similar to the ones

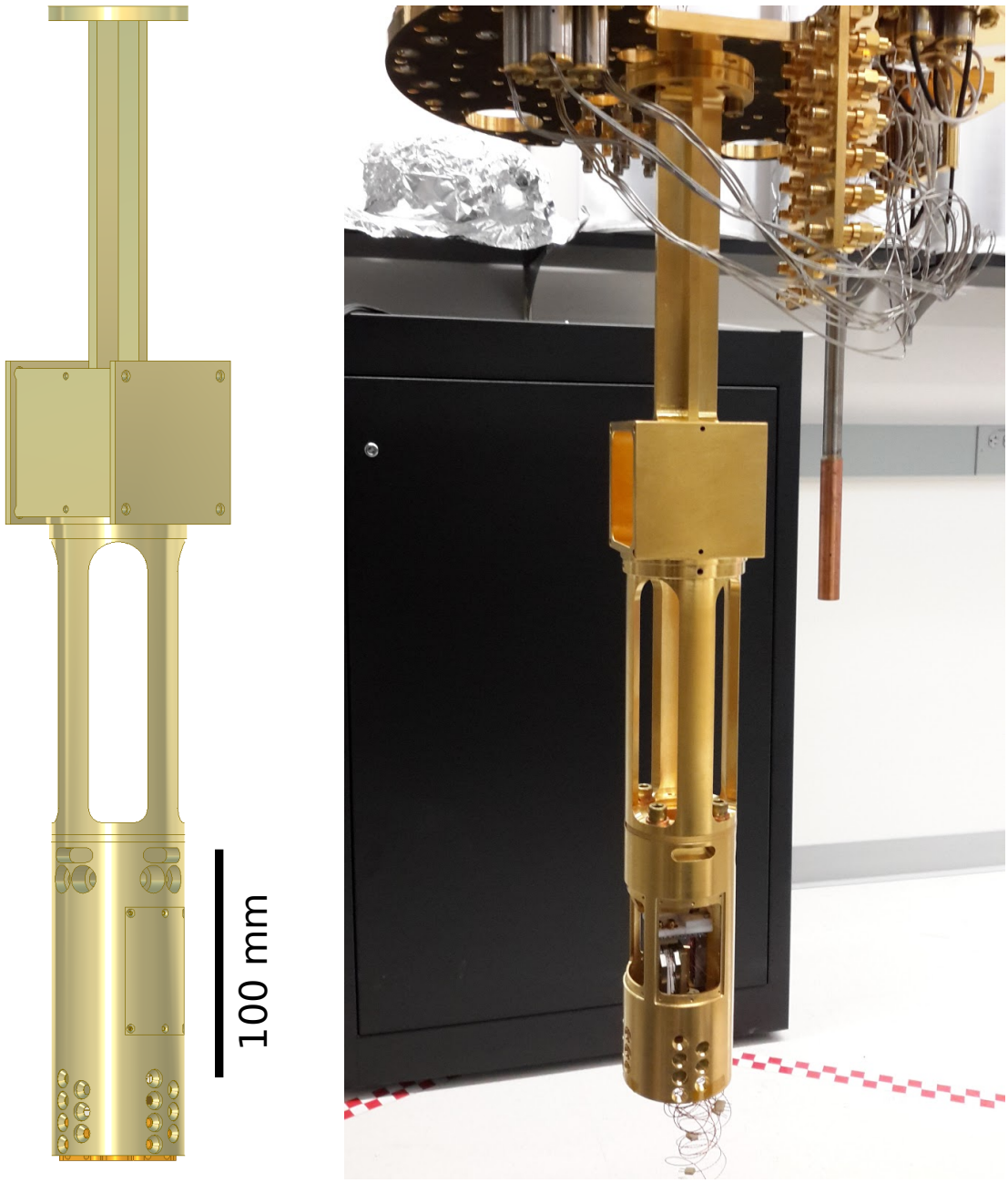

Figure 4.3: Diagram and photo of the coldfinger and microscope. The windows are removable. There is a light tight copper can that screws into the coldfinger.

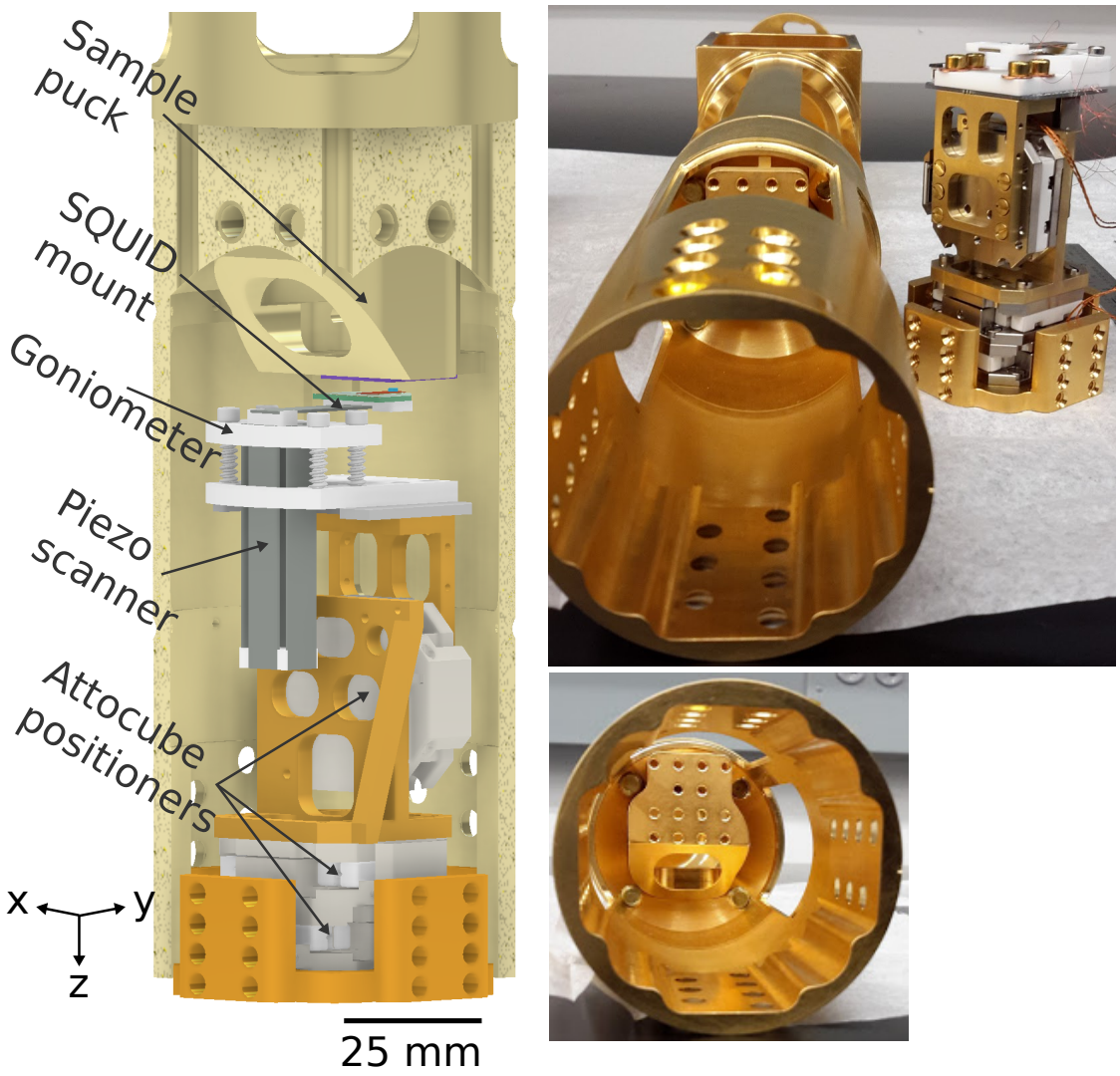

Figure 4.4: Diagram and photos of the microscope and scanning assembly. The sample, shown in purple, is mounted to the sample puck. A SQUID PCB holds the SQUID and is attached to the SQUID mount Macor piece which is a part of the piezo scanner. We can change the angle of approach of the SQUID using the goniometer. Three Attocube ANPx311 positioners give us 6 mm course range.

described in Refs.[64, 4], which in turn is mounted on a three-axis stack of Attocube coarse positioners (see Figure 4.4). We chose bearing-based Attocube ANPx311 positioners with 6 mm coarse range. Two machined brackets adapt a high-load ANPx311 positioner to act as a z positioner. These bearing-based positioners were advertised as being stiffer and than the other smaller piezo scanners. The z Attocube is also a high load positioner so it would function properly at a 90 degree angle. The Attocube positioners are made of Grade 2 (99% pure) titanium instead of the more common grade 5 titanium which is an alloy of titanium, 6% aluminum, 4% vanadium, <0.25% iron and <0.2% oxygen. Grade 5 is stronger than pure titanium but superconducts at 5.4 K [62]. The exact superconducting transition of Grade 2 titanium depends strongly on impurities in the material. Unfortunately, the supplier of titanium for Attocube is not specific enough to definitively state the expected superconducting transition temperature. The scanner is assembled from piezoelectric bimorphs and machined Macor parts [65, 5]. Two pairs of "s-benders" move the SQUID in a horizontal plane, while an additional cantilever piezo allows for vertical motion. Imaging range and stiffness compete in the scanner design, since both depend on the dimensions of the benders. Here we chose x, y s-benders with lateral dimensions 38.1×6.4 mm and 0.13 mm thickness. The z bender has 25.4×6.35 mm lateral dimensions and is 0.19 mm thick. The benders are joined by Macor blocks using EPO-TEK H70e epoxy. The scanner is attached to a top Macor plate visible in Figure 4.4. This plate is mounted with spring-loaded screws to a bottom Macor plate, which in turn is rigidly mounted on the coarse positioners. This arrangement allows us to adjust the alignment angles between the SQUID and the sample through adjusting the spring-loaded screws. Our scan range at cryogenic temperatures is approximately 150 µm in the x, y-directions and 110 µm in the z-direction. The scanner and Attocube stack are mounted on a copper puck

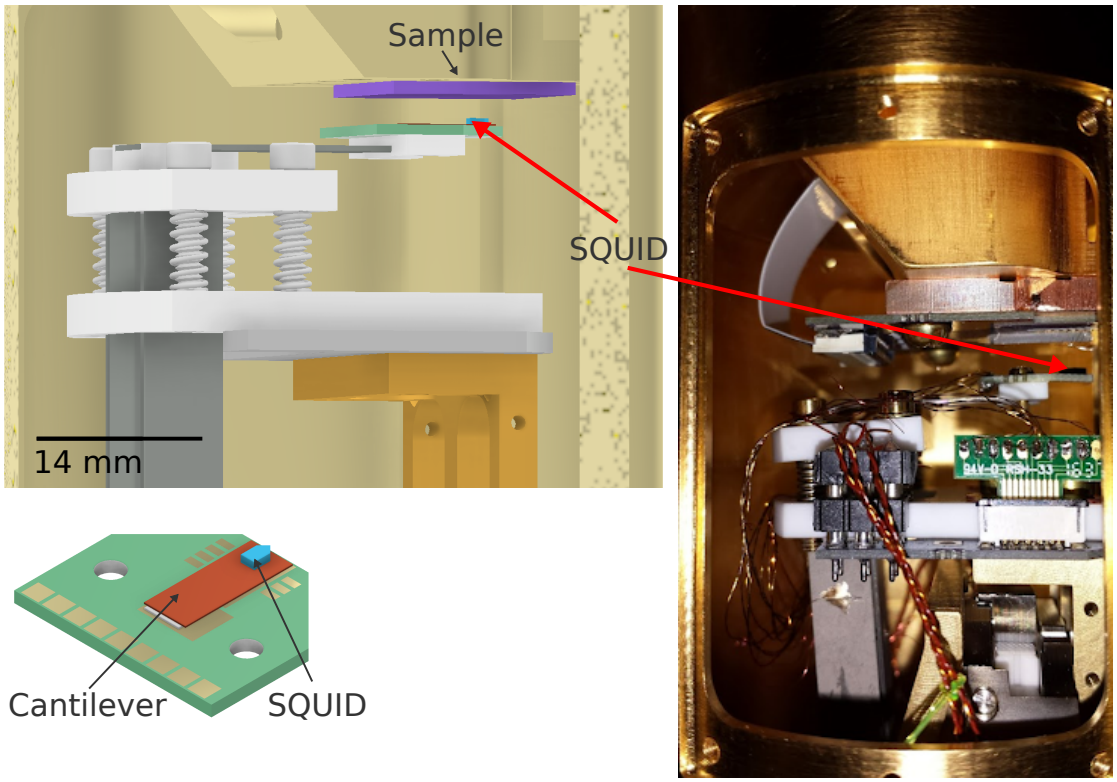

Figure 4.5: Diagram and images of piezo scanner. The SQUID is mounted on a brass cantilever attached to a PCB which is screwed to the end of the home-built piezo scanner. The sample is glued to the sample puck upside down either on a PCB or straight on the gold plated copper surface.

that slides out at the bottom of the microscope housing allowing for easy SQUID replacement. The copper puck is threaded and bolted on two adjacent sides to the microscope housing with four brass screws on each side. To detect when the SQUID touches down on the sample, the SQUID is mounted on a flexible brass cantilever. We monitor the capacitance between this cantilever and a ground plane on the printed circuit board. At touchdown, a sharp increase in the capacitance is detected. These cantilevers are typically 5 mm long, 2 mm wide and 50 µm thick.

The sample is mounted upside-down on a puck that slides into the top of the microscope housing to allow easy sample replacement and is fastened using four 1/4-20 brass screws. The large clamping force provided by these large bolts and

the gold plated copper surfaces allow for high thermal conductivity. A ruthenium oxide thermometer is mounted on the sample puck. The base temperature on the mixing chamber plate is ∼10 mK. The sample mount reaches 50 mK at the same time as the mixing chamber plate and continues to cool as the mixing chamber plate cools further. The sample mount thermometer is calibrated to 50 mK, but based on the continued change in its resistance, we estimate that the sample mount cools to at least 30 mK and likely lower. Importantly, no appreciable heating is observed during scanning at a rate of ∼20 µm/s even at base temperature.

Three wire bundles with 12 twisted pairs are connected to the microscope. From room temperature to 4 Kelvin, two bundles use 36 AWG phosphor bronze and one bundle uses 36 AWG Cu and NbTi/CuN wires for low resistance connections. After that, all bundles use a combination of copper wires, either solid core copper twisted pair at 32 AWG or stranded 30 AWG copper wire. The stranded wire is most often used with micro d connectors while the solid core is most often used with DIP pins. Two of these bundles are used to operate the piezo scanner, the Attocube coarse positioners and the SQUID. One bundle is available for sample connections. More specifically, the Attocube is driven by the superconducting wire bundle as it requires the lowest resistance in order for the RC times to be small enough that the sawtooth signal can pass relatively unfiltered. The Attocube need the steep falling edge of the sawtooth so the piezos can slip. While naively the Attocubes should only need 2 drive wires and 3 sense wires per Attocube for a total of 15 wires, we were advised to use 4 drive wires (2 for positive and 2 for negative) to reduce the resistance. This requires 21 wires for the Attocubes. and gives us 3 free wires. We rarely use these wires. In addition, the cryostat includes rigid and semi-rigid coaxial wiring to the mixing chamber plate. Besides their use for sample wiring, we also use coax for the SQUID capacitance height measurement.

The combination of 24 wires available to connect to the sample and large coarse positioning range allows us to image devices with several contacts and electrostatic gates, perform full transport characterization of these devices, and image multiple devices in a single cooldown.

Cylindrical Microscope

I chose to make the microscope from a cylindrical rod of copper to maximize the amount of space available for the design. The bore of the magnet is circular, so this shape is the best for maximizing the amount of available space. The area around the scanner is bored out. While it might have been possible to mill a smaller area out instead, which would have been stiffer, I chose this method to ensure that the scanner would not run into the sides of the microscope if we needed to increase the size of components on the scanner. Another reason that I chose a circular shape is that conventional wisdom states that a cylinder is stiffer than a similarly thick rectangular tube.

Large bolts

For thermalization we use 1/4-20 bolts to fasten the coldfinger to the mixing chamber plate, the coldfinger to the microscope, and the coldfinger to the sample puck. Many other systems use smaller 4-40 or M4 bolts. However, these large bolts allow us to apply significantly more force on the gold plated copper interface. For instance, the ultimate yield strength of a 4-40 screw is 1400 N compared to 7700 N for a 1/4-20 screw. In this way, I could ensure that the largest thermal resistance in the microscope comes from the sample mount itself. For instance, the sample puck was designed with a thermal resistance of about 1 W/K while the gold-gold

interface fastened by 1/4-20 screws has a thermal resistance of about 5 W/K. Unfortunately, the thermal resistance of the sample mount cannot be decreased due to insufficient space. Every other segment of the coldfinger and microscope was designed to have a thermal resistance greater than 1 W/K. The section that was the closest to this threshold was the coldfinger section after the wiring box. Note that we use the gold-gold interface thermal conductivity quoted in Ekin of $0.007\,\mathrm{W\,K^{-1}}$ at 20 mK for 100 lbf [17].

Larger bolts are also significantly harder to strip, which is a large problem with small brass socket head bolts. We have stripped many bolts smaller than 4-40 or M3. In general, I chose to use the largest bolts possible in all locations. For instance, to secure the microscope to the scanner stack mount, I use 8-32 flat head bolts. They are slightly too large for the space but instead of reducing to 4-40 or 6-32, I had the threaded part (scanner stack mount shown in the diagram in Figure 4.4) slightly counter sunk to ensure that the bolts fit snugly and tighten to ensure the full face of the scanner stack mount makes good contact with the microscope. Brass bolts are necessary so that the bolts shrink more than the copper at low temperature to ensure that the pieces do not loosen when cold. While some use conical washers or washers made of more exotic material, it is prudent to design the microscope to not rely on such techniques.

Keying and Usability

Wherever possible, I tried to design small features that would make it easier to assemble the microscope. For instance, there sample puck was designed to only fit into the microscope in one single way. There is no way to rotate or insert the sample puck except in a way that will not damage either a properly installed

sample or SQUID. Similarly, the scanner stack mount is keyed so it cannot rotate. Another small detail is that there are small bolts in the cold finger and associated slots in the microscope. They are designed such that you can lift the microscope into place and hang it off the tiny screws. This way, you do not need to thread the 1/4-20 bolts into the microscope to secure it.

The windows in the microscope were made extremely large to ensure that there was plenty of space to look into the microscope to align it. I also had window covers made that screw into the microscope. The idea was to have a third light tight shield to ensure no radiation reached the sample. A side benefit is that these window covers might serve as cross braces for the windows. Additionally, it helps prevent accidental damage to the SQUID or sample when closing the cryostat.

4.4 Lessons Learned from Using the Microscope

We learned many lessons from using this microscope.

1. The windows could have been made smaller. We end up not using the bottom third of the window when aligning. Decreasing the window size would increase the stiffness of the microscope.
2. The sample puck was too restrictive. This design only has space for the main sample for scanning and a space in the front for another sample. It turns out that adding a third space for a sample was useful. Adding space for a thermometer was also very useful.

   More importantly, it was very useful to have top access to the scanner in order to adjust the goniometer for changing the angle of the SQUID.

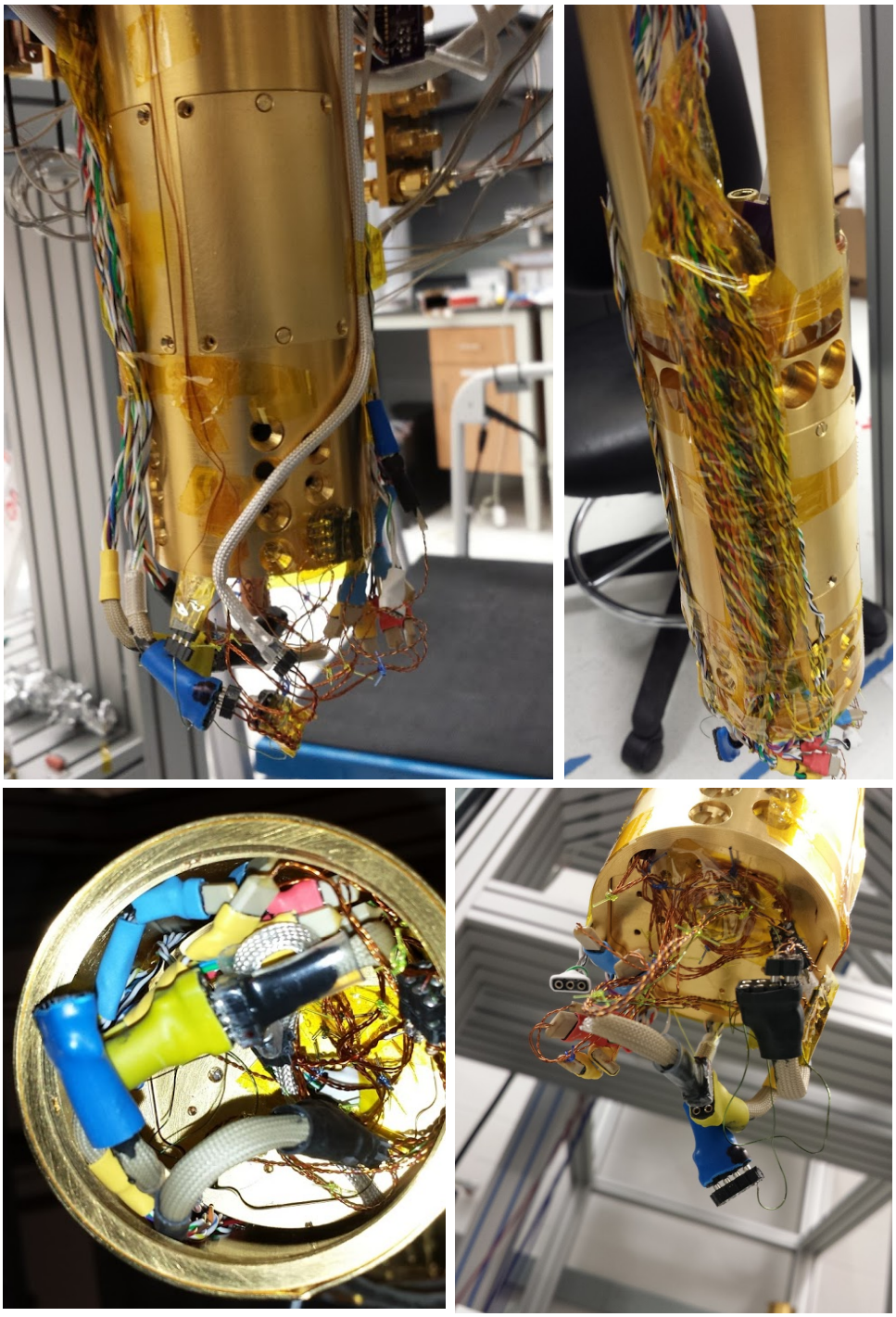

Figure 4.6: Wiring in the microscope. The piezo, Attocube, and SQUID wires all are placed between the outside of the microscope and the light tight can attached to the coldfinger. We use 32 AWG stranded wire with Teflon insulation (colored wires) and solid core copper wires sleeved in fiberglass or bare. All wires are terminated in DIP connectors. Note that the wires are extremely messy and bent in a tight radius, particularly in the lower left image with the millikelvin light tight can attached to the coldfinger. This should be fixed in future designs.

3. I did not design for wiring sufficiently. I left enough space around the outside of the microscope beneath the light tight can thermalized to the mixing chamber plate. However, you must remove these wires each time you open the microscope and tape them to the microscope when you close the cryostat.

   These wires often break and are difficult to plug into the correct dip pins. In order to design channels to hold the wires, it would necessitate removing material which would sacrifice stiffness.

   We designed a new wiring harness that uses micro d connectors but we never installed it into the microscope.

4. The wiring box was unnecessary. The wiring box on the coldfinger was designed so the copper powder filters could directly screw into the coldfinger so we would never need to worry about shielding the wires. We have never filtered the wires with copper powder filters nor have we ever worried about shielding the wires. This may change in future experiments.

5. There are lots of sample-to-probe vibrations in the 500 Hz range. If we had expected those vibrations, we would have worked harder on making the coldfinger. Our original design was a cylinder but was rejected because it was hard to attach the copper powder filters to it and because we wanted the coldfinger to be light weight while still having good thermal conductivity.

CHAPTER 5

CHARACTERIZING A SCANNING SQUID MICROSCOPE

Scanning SQUID magnetometry in dilution refrigerators cooled with liquid helium have existed for many years. Our cryogen-free dilution refrigerator adds considerable complications to scanning SQUID magnetometry because the pulse tube that allows the cryostat to reach 4 K creates vibrations that would not be present in other scanning SQUID microscopes. As such, I focus on characterizing the vibrations in our cryogen-free SQUID microscope. In this chapter, I briefly show some data of imaging in our cryostat, then focus on measuring, modeling, and characterizing vibrations. Parts of this chapter was adapted from [45]

5.1 Imaging Test Structures

The first characterization of the SQUID microscope performed was a qualitative characterization using a test sample made by Brian Schaefer. He made superconducting niobium traces on a silicon substrate and provided bonding pads in order to flow current through the traces. We imaged this simple test sample as a proof of concept and to find and evaluate any aberrations in the magnetic field image.

In Figure 5.1A, we demonstrate magnetic imaging at 50 mK. The signal is from the diamagnetic response of the superconductor measured by our SQUID magnetometer. There is a small background field, likely from the earth's magnetic field. The width of the traces is about 5 µm while the spacing between the traces is about 80 µm as shown by the optical microscope image in Figure 5.1B. The small circular defects that seem to interrupt the traces are superconducting vortices in the niobium, not breaks in the wire.

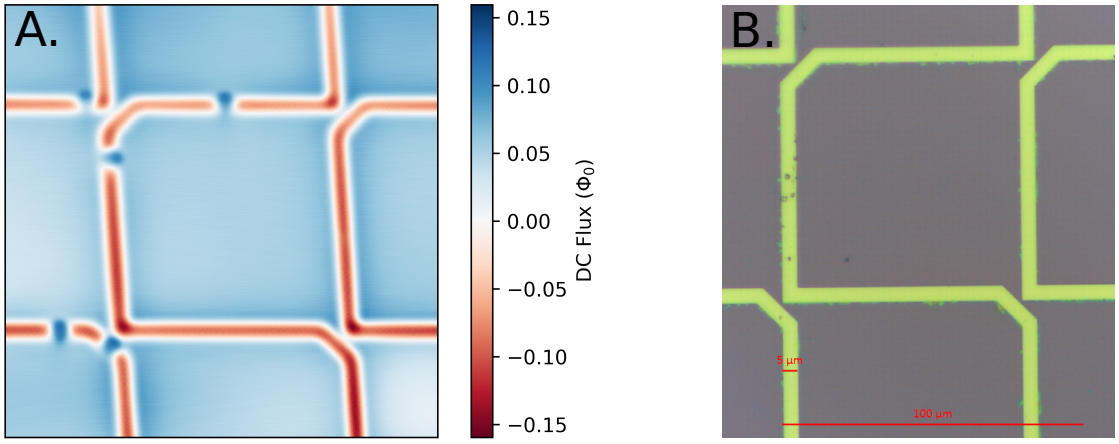

Figure 5.1: SQUID image of test structures. (A) Magnetic image at DC frequency of a meander of niobium at 50 mK. (B) Microscope image of the test structures at room temperature. The gold traces are niobium and the gray background is silicon. The traces are 5 µm and the spacing of the traces is 80 µm.

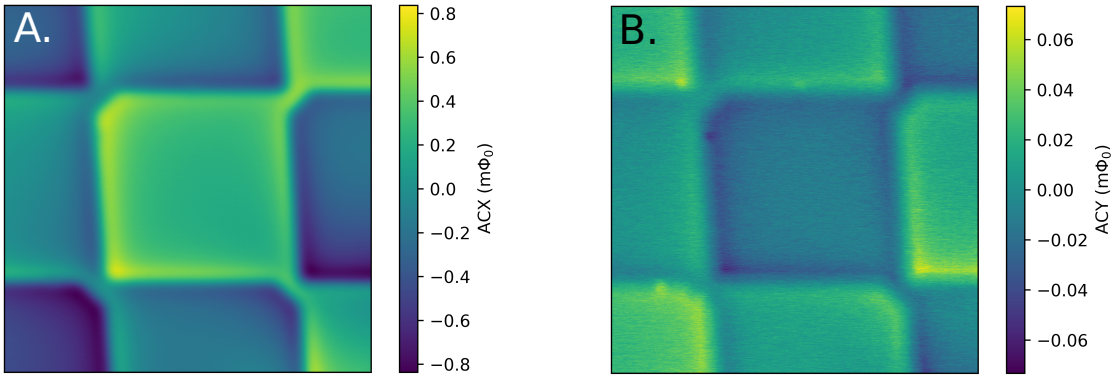

Figure 5.2: SQUID image of current flow through test structures at 50 mK. Current flows through the superconducting traces at 6931 Hz and the SQUID signal is filtered using a lock-in amplifier. We plot the (A) in-phase and (B) out-of-phase components of the signal.

We are able to flow current through the wires and detect the magnetic field from the AC current as shown in Figure 5.2. We use flow current at 6931 Hz and use a lock-in amplifier to filter out the other signals to cleanly observe the signal due to the current carrying traces. We plot the X and Y components, or in-phase and out-of-phase components of the response in Figure 5.2A and B respectively.

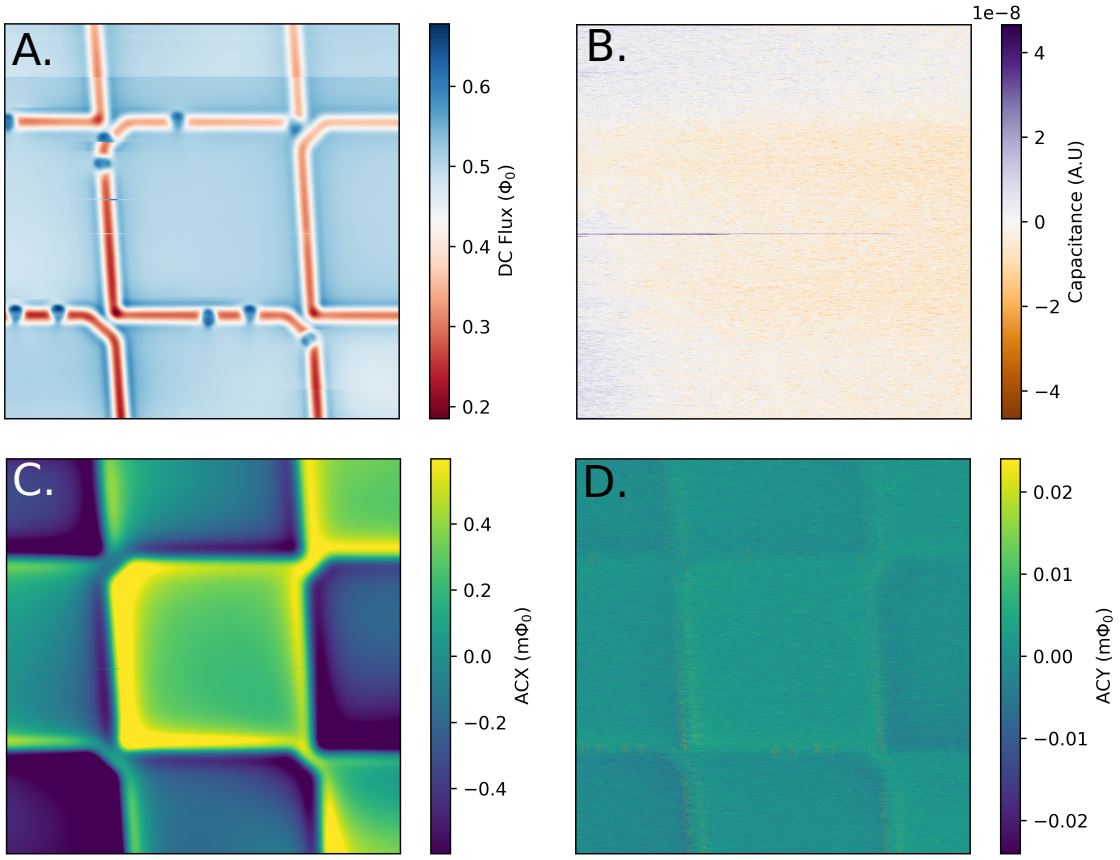

Figure 5.3: SQUID image of test structures at 4 K. (A) Magnetic image at DC frequency. (B) Capacitance of cantilever over the image. A large signal implies the SQUID touched the sample. Current flows through the test structure at 6931 Hz and the SQUID signal is filtered using a lock-in amplifier to plot the (A) in-phase and (B) out-of-phase components of the signal.

We can image the same field of view from 4 K to 50 mK. We plot the same images at 4 K in Figure 5.3A,C,D. We flow a different amount of current in each set of images. The line at the top quarter of Figure 5.3A are not uncommon when imaging and often are from the SQUID touching the sample or cellphones near the cryostat.

We also plot the capacitance measurement used to determine if the SQUID came into contact with the sample in Figure 5.3B. While there are some slight gradients, we do not see any features that suggests the SQUID was in-contact with

the sample during the image. For scale, the full range of the capacitance image in this figure is about 0.15 fF.

From these images, we were able to establish the scan range in micrometers of our piezo scanner. We also notice that the X and Y motion are not perfectly orthogonal. We changed the position of the wires in the scanner to minimizes this abnormality.

5.2 Vibrations

The pulse tube causes vibrations in the cryostat. These only affect the imaging if they cause a relative motion between the SQUID and sample. We characterize this relative motion by following a method first reported in Ref. [63] based on analyzing the excess flux noise caused by vibrations in areas with large magnetic field gradients.

In general, our goal is to derive the amplitude of vibrations as a function of frequency in the X, Y, Z directions. The intuition behind this procedure is that the flux noise at frequency f due to vibrations in the x direction should scale like $\frac{\partial \Phi}{\partial x} X(f)$. Thus, we need to gather flux noise data in regions with large amplitudes of $\frac{\partial \Phi}{\partial x}, \frac{\partial \Phi}{\partial y}, \frac{\partial \Phi}{\partial z}$ and fit the X, Y, Z vibrations at each frequency.

5.2.1 Vibration Model

To find the power spectral density of the vibrations, we model the flux power spectral density at each pixel (i, j) and frequency f as a sum of vibration-induced

noise and intrinsic SQUID and electrical noise [4]:

$$\left[\hat{\Phi}_{\text{model}}(f)\right]_{ij} = \sqrt{\left(\left|\left[\frac{\partial\Phi}{\partial x}\right]_{ij}\hat{X}(f) + \left[\frac{\partial\Phi}{\partial y}\right]_{ij}\hat{Y}(f) + \left[\frac{\partial\Phi}{\partial z}\right]_{ij}\hat{Z}(f)\right|\right)^2 + \left(\hat{N}(f)\right)^2}. \tag{5.2.1}$$

Here, $\hat{\Phi}(f)$ denotes the flux noise amplitude spectral density, $\partial\Phi/\partial(x,y,z)$ are the flux gradients shown in Figure 5.5, $\hat{X}(f), \hat{Y}(f), \hat{Z}(f)$ are the vibrations along the (x,y,z) direction, and $\hat{N}(f)$ models intrinsic SQUID noise and is strictly positive.

The intrinsic SQUID noise term is necessary and the vibration and intrinsic noise terms add in quadrature because these noise sources should be independent.

In applying this model we assume that the vibrations are independent of the motion of the benders. This is reasonable because the typical deflection of the benders is small compared to their size. The mechanical properties are therefore not expected to change significantly within the scan range. This assumption is also supported by the absence of significant scan distortions even at the extremes of our scan range.

We fit the spatial map of the noise to Eqn. (5.2.1) to obtain the spatial vibrations $\hat{X}, \hat{Y}, \hat{Z}$ and electrical noise $\hat{N}$ at each frequency. The exact cost function we are minimizing takes the form

$$\text{Fit}(f) = \underset{\hat{X},\hat{Y},\hat{Z},\hat{N}}{\arg\min} \sum_{(i,j)} \left(\left|\left[\hat{\Phi}(f)\right]_{ij}\right| - \left|\left[\hat{\Phi}_{\text{model}}(f)\right]_{ij}\right|\right)^2 \tag{5.2.2}$$

We use statistical bootstrapping with 200 trials to avoid local optima and determine the 95% confidence intervals of the fits [16]. Statistical bootstrapping, in general, is a method to overcome limited data or the inability to take additional

data. One assumes the recorded data is a proxy for an experiment and samples with replacement from the recorded data to simulate repeating the experiment multiple times. We choose to use the Monte-Carlo re-sampling algorithm where the re-sampled data is the same size as the original dataset. In practice, performing this bootstrapping is extremely time intensive as we need to solve the least squares optimization problem 200 times for every frequency in the 0.25 to 1000 Hz bandwidth with steps of 0.25 Hz. We parallelize over the different frequencies for a single re-sampled image.

Derivation

It is straightforward to derive the vibration term of equation 5.2.1 before taking the magnitude.

Theorem 5.2.1. *For magnetic flux noise* $\hat{\Phi}(x, y, z, f) = \mathcal{F}(\Phi(x, y, z, t))$ *caused solely by vibrations, we can approximate it to first order in* X, Y, Z *vibrations by*

$$\left|\hat{\Phi}(x, y, z, f)\right| = \left|\frac{\partial \langle\Phi\rangle_t}{\partial x} X(f) + \frac{\partial \langle\Phi\rangle_t}{\partial y} Y(f) + \frac{\partial \langle\Phi\rangle_t}{\partial z} Z(f) + O(X^2, Y^2, Z^2)\right|$$

where $\langle\Phi\rangle_t$ *is the time average of* $\Phi(x, y, z, t)$.

Proof. Consider a point (x, y, z) in space. If there are some time varying motion that differs from the ideal position, we can write those as

$$x = x_0 + \Delta x(t)$$

$$y = y_0 + \Delta y(t)$$

$$z = z_0 + \Delta z(t)$$

where x_0, y_0, z_0 are the true locations being perturbed by some $\Delta x, \Delta y, \Delta z$.

Assuming the vibrations are small, we can Taylor expand around the point (x_0, y_0, z_0)

$$\begin{aligned}\Phi(x,y,z,t) = \Phi(x_0,y_0,z_0,t) &+ \frac{\partial \Phi}{\partial x}\Big/_{x_0,y_0,z_0,t}(\Delta x(t) - x_0) \\ &+ \frac{\partial \Phi}{\partial y}\Big/_{x_0,y_0,z_0,t}(\Delta y(t) - y_0) \\ &+ \frac{\partial \Phi}{\partial z}\Big/_{x_0,y_0,z_0,t}(\Delta z(t) - z_0)\end{aligned}$$

Assume that at a specific point in space, the flux at a specific time is the average flux at that location plus a random noise term that encodes fluctuations in the measurement or any time dependent dynamics of the system. Then, we can write

$$\Phi(x,y,z,t) = \langle \Phi(x,y,z,t) \rangle_t + N(t)$$

Another way of thinking about this is

$$\frac{\partial \Phi}{\partial x} = \frac{\partial \langle \Phi \rangle_t}{\partial x} + \frac{\partial \cancel{N}}{\cancel{\partial x}}$$

where the last term is zero as the noise is not position dependent. We can think of the flux change as a function of position is independent of time. Any change in the flux position derivatives happen at all times, not just at some specific times.

Substituting,

$$\Phi(x,y,z,t) = \Phi(x_0,y_0,z_0,t) + \frac{\partial \langle\Phi\rangle_t}{\partial x}\Big|_{x_0,y_0,z_0,t} (\Delta x(t) - x_0) + \frac{\partial \langle\Phi\rangle_t}{\partial y}\Big|_{x_0,y_0,z_0,t} (\Delta y(t) - y_0) + \frac{\partial \langle\Phi\rangle_t}{\partial z}\Big|_{x_0,y_0,z_0,t} (\Delta z(t) - z_0)$$

The Fourier transform of a function without t dependence is a delta function times that function, so

$$\hat{\Phi}(x,y,z,f) = \frac{\partial \langle\Phi\rangle_t}{\partial x}\Delta\hat{x}(f) + \frac{\partial \langle\Phi\rangle_t}{\partial y}\Delta\hat{y}(f) + \frac{\partial \langle\Phi\rangle_t}{\partial z}\Delta\hat{z}(f) + F\left[\Phi(x_0,y_0,z_0,t)\right] - \delta(f)\left(\frac{\partial \langle\Phi\rangle_t}{\partial x}x_0 + \frac{\partial \langle\Phi\rangle_t}{\partial y}y_0 + \frac{\partial \langle\Phi\rangle_t}{\partial z}z_0\right)$$

The last term we can neglect if we only look at $f > 0$. The second to last term is the Fourier transform of any noise that does not come from vibrations, as it is for static x_0, y_0, z_0.

Thus if we only fit for $f > 0$, assume all noise comes from vibration, then take the absolute value, we arrive at the formula we wished to show.

□

Justifying the Magnitude

In equation 5.2.1 we use the absolute value of the flux noise due to vibrations despite the fact that $\hat{\Phi}(f)$ might be in general complex valued. To understand exactly what assumption we are making by taking the magnitude of the Fourier

transform of the time trace, consider the equation for the flux noise from vibrations

$$\Phi(x, \hat{y}, z, f) = \frac{\partial \langle \Phi \rangle_t}{\partial x} \Delta\hat{x}(f) + \frac{\partial \langle \Phi \rangle_t}{\partial y} \Delta\hat{y}(f) + \frac{\partial \langle \Phi \rangle_t}{\partial z} \Delta\hat{z}(f)$$

where $\Delta\hat{x}, \Delta\hat{y}, \Delta\hat{z}$ are the vibrations in the x, y, z directions as a function of frequency.

Assume that instead of thinking about measuring vibrations, we think about creating vibrations. We could think of it as applying some small time dependent oscillation to the piezos with amplitude $\Delta x(t), \Delta y(t), \Delta z(t)$. We could expand in an infinite Fourier series and write

$$\begin{aligned}
\Delta x(t) &= \sum X_\omega \sin(\omega t) \\
\Delta y(t) &= \sum Y_\omega \sin(\omega t + \tau) \\
\Delta z(t) &= \sum Z_\omega \sin(\omega t + \tau')
\end{aligned}$$

where τ, τ' are some arbitrary time or phase offset of the vibrations in y, z directions. We can then write the vibrations in the frequency domain as

$$\begin{aligned}
\Delta\hat{x}(t) &\sim X_\omega \\
\Delta\hat{y}(t) &\sim Y_\omega e^{i\tau} \\
\Delta\hat{z}(t) &\sim Z_\omega e^{i\tau'}.
\end{aligned}$$

Note that $X_\omega, Y_\omega, Z_\omega \in \mathbb{R}$ as the vibrations are real valued. If we assume $\tau, \tau' \sim 0$,

$$\hat{\Phi}(\omega) = \left|\hat{\Phi}(\omega)\right|$$

which is what we assumed.

If we assume $\tau, \tau' \to 0$, we are essentially assuming that the vibrational modes are linear, not circular. We can see this by plotting $\Delta x(t), \Delta y(t)$ for vibrations only at frequency ω for different values of τ and $X_\omega = Y_\omega$. We show the result

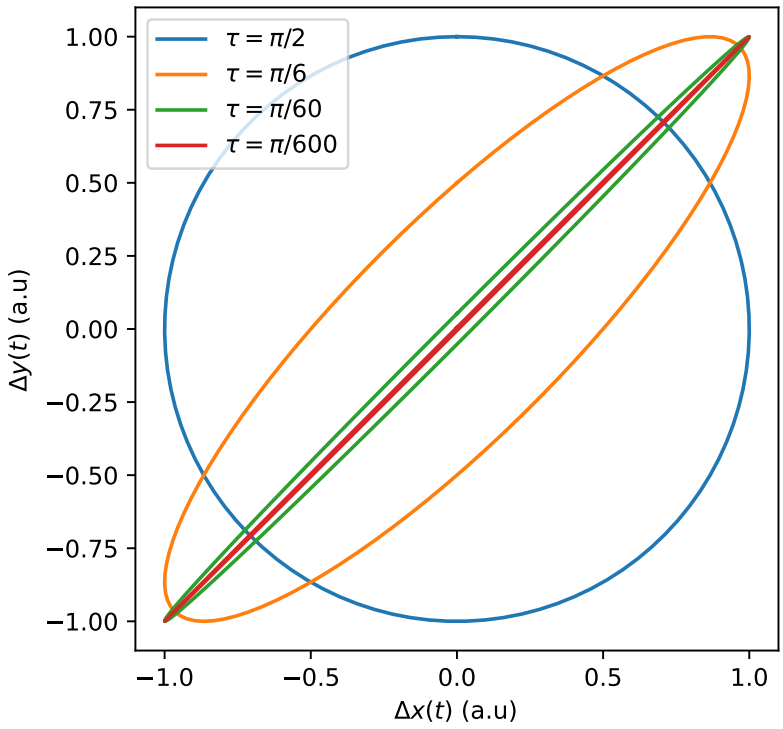

Figure 5.4: Simulated vibrations for decreasing phase offset. When the phase offset between the X and Y vibrations τ is small, the vibrational modes are linear instead of circular.

in Figure 5.4. Thus, if we expect only linear vibrational modes, we can take the absolute value of $\phi(f)$.

Practically speaking, in order use the full Fourier transform of $\phi(x, y, z, t)$ instead of the magnitude like we have done, you need to record the time offsets between pixels extremely accurately. While we recorded the time offsets using python, this might not have been accurately enough. Additionally, doing this adds 3 extra fit parameters, as now we are fitting complex values to $\hat{X}(f), \hat{Y}(f), \hat{Z}(f)$.

5.2.2 Measuring Vortices as Sources of Magnetic Flux Gradient

When measuring a source of magnetic flux gradient to perform the fitting described previous, it does not matter what is measured as long as it has high flux gradient. We chose to measure a superconducting vortex due to convenience but dipoles or other magnetic dirt would also suffice. We find that objects with order $10\,\mathrm{m}\Phi_0/\mu\mathrm{m}$ flux gradient is sufficiently strong. In our StarCryo Squid Array electronics, this usually corresponds to objects that require "medium" sensitivity to image without clipping.

Figure 5.5(a) shows a vortex in a microstructure fabricated from Sr_2RuO_4. The image of the vortex has a tear-drop shape, which is due to the shape of the SQUID's sensitive area [29, 38]. The sensitive area is formed by a circular loop that connects with two leads to the main body of the SQUID. Magnetic flux couples into a small unshielded opening between the leads which causes a deviation from a perfectly circular shape of the sensitive area.

We obtain the magnetic flux gradients in the (x, y) direction (Figs. 5.5(b,c)) by numerically differentiating Figure 5.5(a). To obtain the flux gradient in the z direction (Figure 5.5(d)) we took a second measurement at $\Delta z = 0.6\,\mu\mathrm{m}$ higher than Figure 5.5(a). Relative motion between the SQUID and the sample causes noise in the measured flux signal that depends on the strength and direction of the gradient and the magnitude and direction of the motion. The intrinsic flux noise of the SQUID has a white noise floor on the order of $1\,\mu\Phi_0/\sqrt{\mathrm{Hz}}$ and a $1/f$ tail below 100 Hz. Given the magnitude of the flux gradients of approximately $10\,\mu\Phi_0/\mu\mathrm{m}$, flux noise of $1\,\mu\Phi_0/\sqrt{\mathrm{Hz}}$ corresponds to an approximate sensitivity of $0.1\,\mathrm{nm}/\sqrt{\mathrm{Hz}}$

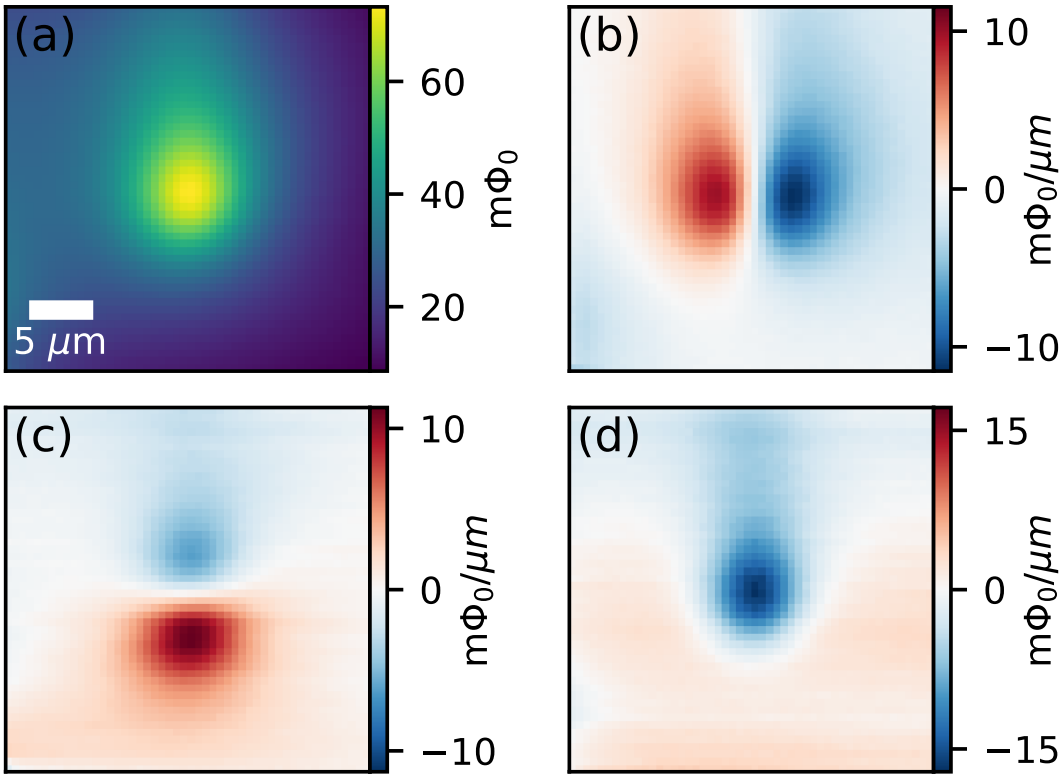

Figure 5.5: Superconducting vortex for vibration measurement. (a) Image of a superconducting vortex in a FIB defined microstructure. ((b-d) Flux gradients in the (b) x, (c) y, and (d) z directions. The x and y gradients are obtained from numerically differentiating (a), whereas the z gradient is obtained from measurements taken at two heights separated by $\Delta z = 0.6\,\mu\text{m}$. The tear-drop shape is due to the shape of the SQUID's sensitive area.

for detecting relative motion between the SQUID and the sample. Each pixel in Figure 5.5(a) is the average of a four-second time trace. The Fourier transforms of each time trace provide a position-dependent flux noise spectral density. Examples of spatial maps of the noise spectral density at a few frequencies are shown in the left panels of Figure 5.6.

5.2.3 Fitting Vibrations

To obtain vibration amplitude spectra, we fit equation 5.2.2 using the magnetic flux derivatives and noise above regions of large magnetic flux gradient. At each frequency, we are finding the X, Y, Z vibrations and N intrinsic SQUID noise that minimizes the difference between the noise value at each pixel and the modeled noise at that pixel. To ensure stability and accuracy, we use statistical bootstrapping and report the average fit parameters.

In Figure 5.6(a-d) we show examples of maps of flux noise spectral density (left panels) and the respective fits to the model in Eq. (5.2.1)(right panels). Figs. 5.6(b,c,d) closely resemble the flux gradients in the (y, z, x) directions respectively as shown in Figure 5.5. This suggests that the vibrations at these frequencies are mostly in the (y, z, x) directions respectively. Figure 5.6(a) shows an example of motion along both the x and y direction. We find good agreement between the flux noise spectral density maps and the fits. These fits allow us to estimate the relative motion in the (x, y, z) directions of the SQUID with respect to the sample as a function of frequency.

Figure 5.7 shows the vibration spectral densities for in-plane and out-of-plane directions obtained by fitting at each frequency. Error bars estimated from the 95% confidence intervals of the fits are less than $1\,\mathrm{nm}/\sqrt{\mathrm{Hz}}$ at all frequencies and omitted to improve readability. Systematic uncertainty comes from uncertainty in the conversion of voltage applied to the piezoelectric scanners to the induced displacement in μm. This conversion is only used in the final step of the analysis, since all measurements, fits and computations are carried out in terms of voltages applied to the piezoelectric scanners. We determine the conversion factors for motion in x and y as 175 ± 10 nm/V from imaging lithographically-defined samples

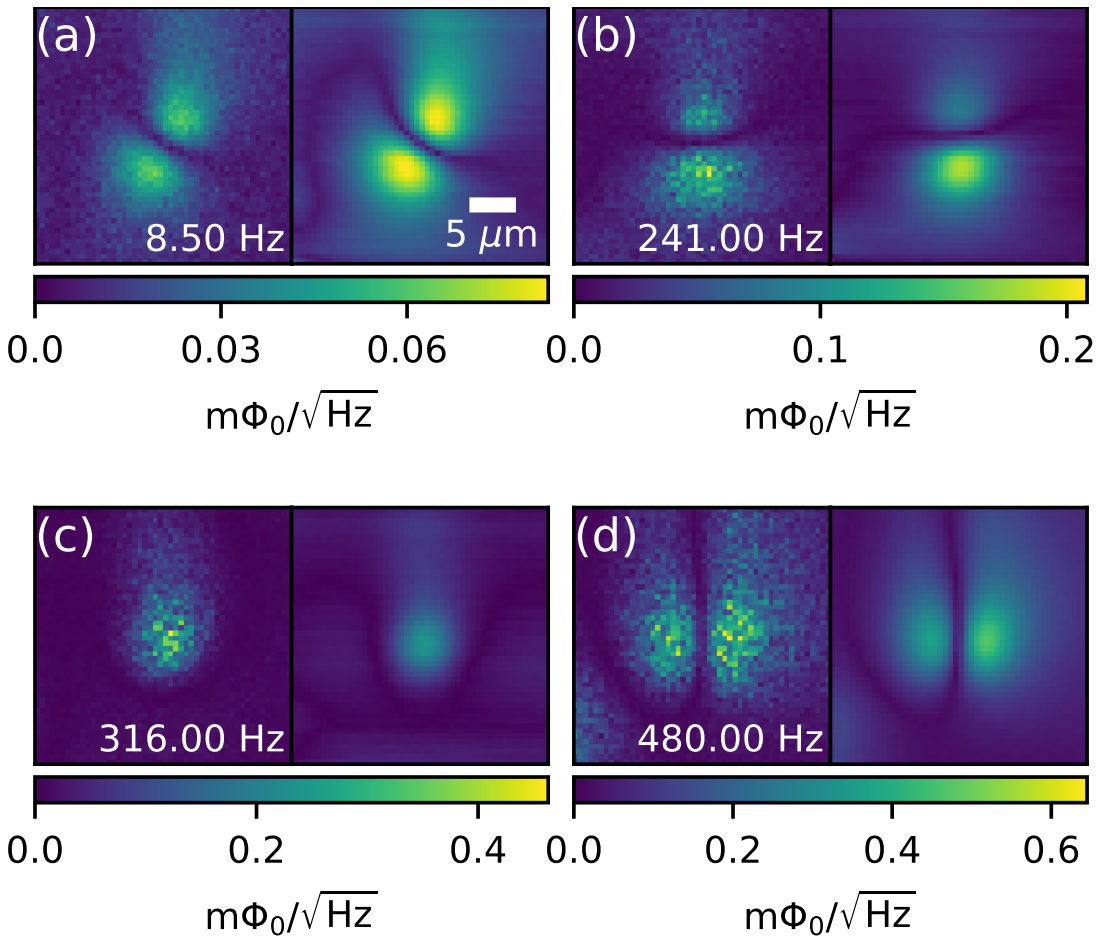

Figure 5.6: Spatial maps of the flux noise spectral density (left panel) at (a) 8.5 Hz, (b) 241 Hz, (c) 316 Hz and (d) 480 Hz and corresponding fits to the model in Eq. 5.2.1 (right panel). Vibrations along the (x, y, z) directions are extracted from the fits.

with known dimensions and features. To obtain the conversion factor for vertical motion we analyze a series of images of a vortex taken at different heights. Using the known height dependence of the magnetic field above current carrying loops, we estimate the conversion to be 149 ± 6 nm/V.

Pressurizing the room-temperature air springs that float the top plate of the cryostat has the most notable impact on the sample-to-SQUID vibrations. The

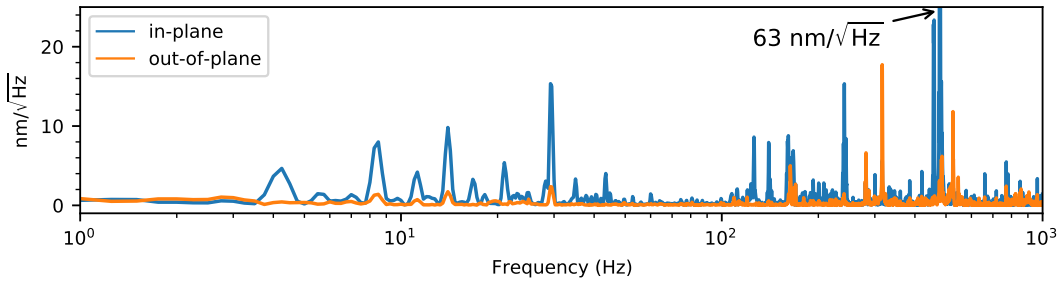

Figure 5.7: Vibration spectral densities for in-plane (blue) and out-of-plane (orange) relative motion of the SQUID and sample. Measurements were taken with the air spring pressurized and the mixing chamber temperature at 80 mK with the ^{3}He/^{4}He mixture circulating. The vertical axis ranges to 25 nm/$\sqrt{\text{Hz}}$ cutting off the highest peak that reaches 63 nm/$\sqrt{\text{Hz}}$ at $\sim$ 480 Hz in the in-plane vibration spectrum.

air springs significantly suppress vibrations below 200 Hz. However, we find a surprising amount of motion in a frequency band between 450 Hz and 490 Hz. The amplitude of the vibrations in this range vary significantly in amplitude over long time scales. However, we could not correlate their behavior with any changes in the cryostat (such as the temperature) or the lab environment. From the structure of the noise spectral density maps, we can determine that the most pronounced peak at $\sim$ 480 Hz corresponds to motion along the x-direction (see for example Figure 5.6(d)). Figure 5.7 is based on a dataset in which these vibrations are particularly pronounced.

To further demonstrate that the vibrations fits in Figure 5.6, we plot the vibration spectral density for the X, Y, Z directions in Figure 5.8. Note that the Y vibrations are allowed to be negative while the vibrations in the X direction are forced to be positive in this fit. This is the same as requiring $-\pi/2 \leq \theta \leq \pi/2$. The dotted lines are at the frequencies plotted in Figure 5.6 and we can see that at frequency 8.5 Hz, the vibrations are in x and y directions. At 316 Hz, the vibrations are mostly in the z direction and at 480 Hz the vibrations are mostly in the

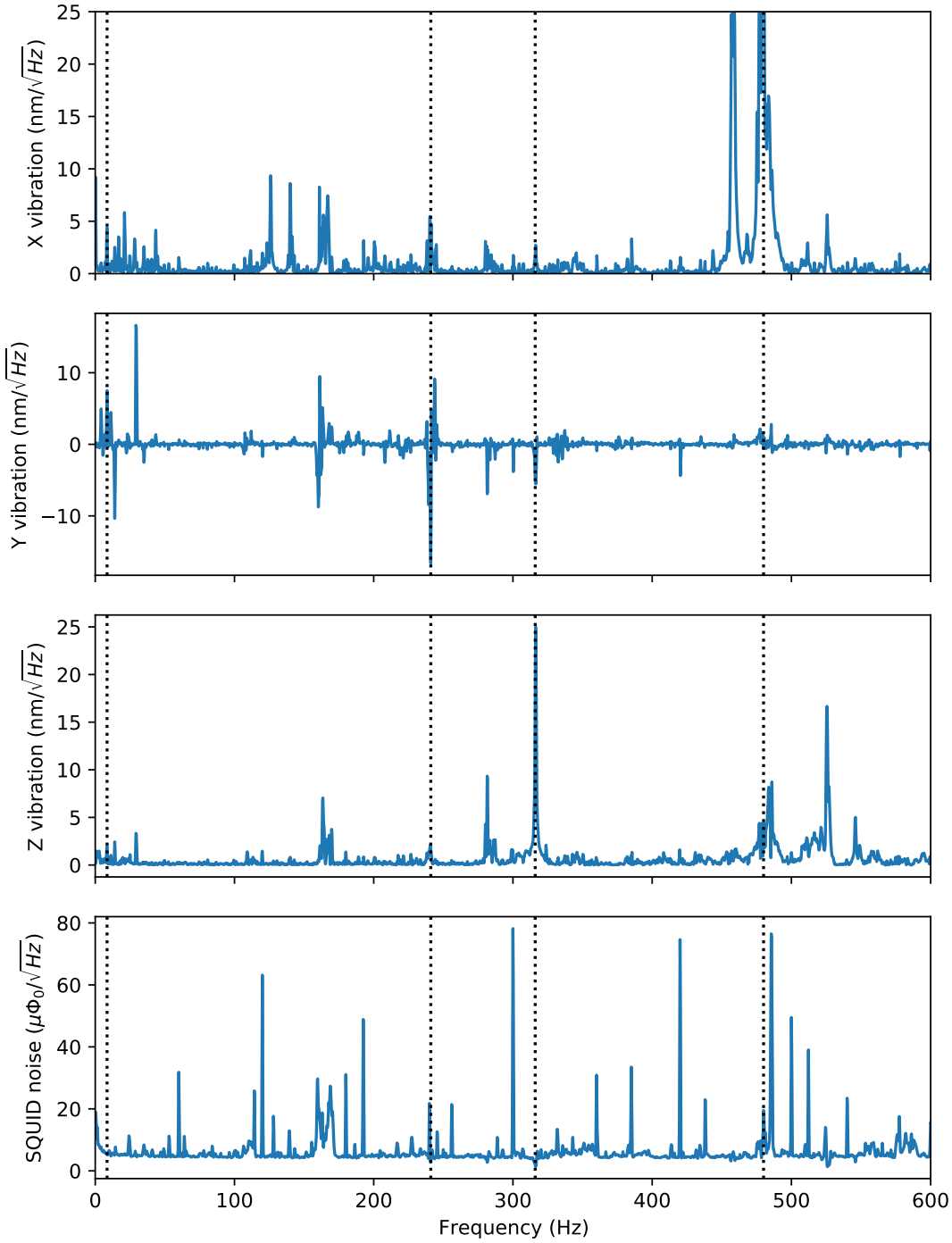

Figure 5.8: Fitted spectral densities for X, Y, Z vibrations and intrinsic SQUID noise. Measurements were taken with the air spring pressurized and the mixing chamber temperature at 80 mK with the ^{3}He/^{4}He mixture circulating. The dotted lines are at frequencies 8.5, 241, 316, and 480 Hz as plotted in Fig 5.5.

x direction as we expect. If we zoom in at 241 Hz, we can see that the vibrations in the x direction are almost zero. This confirms our intuition from comparing the derivatives in Figure 5.5 and the fits in Figure 5.6. We also plot the fitted intrinsic SQUID noise term to demonstrate that this term does not have a large component at the fit frequencies shown in Figure 5.6.

We plot the confidence interval of the fit parameters from statistical bootstrapping in Figure 5.9. Confidence interval can be thought of as a scaled standard error $\sigma/\sqrt{n}$ where σ is the standard deviation and n is the number of samples in the dataset. To determine different percentiles, a different scaling factor is used. Assuming different distributions of the data, like Gaussian vs student-t distribution, will also change these scaling factors slightly. Here, we've used the student-t distribution and set the percent confidence interval to 95%. Note, this confidence interval is not the same as saying that the true amplitude of vibration is less than $1\,\mathrm{nm}/\sqrt{\mathrm{Hz}}$ from the estimated vibration from the fit. This confidence interval states that if we were to repeat the fit i.e., re-sample the image and repeat equation 5.2.2, we have a 95% chance of being within the confidence interval. It is the combination of good fits from Figure 5.6 and the small confidence intervals in Figure 5.9 that suggest our model has low bias and low variance respectively.

5.2.4 Discrepancies Between Measurements

In the previous sections, we have shown vibration data from a single dataset, where the cryostat was at base temperature and we float the cryostat on compressed air springs. In this section we discuss the other datasets and other configurations of operating the scanning microscope.

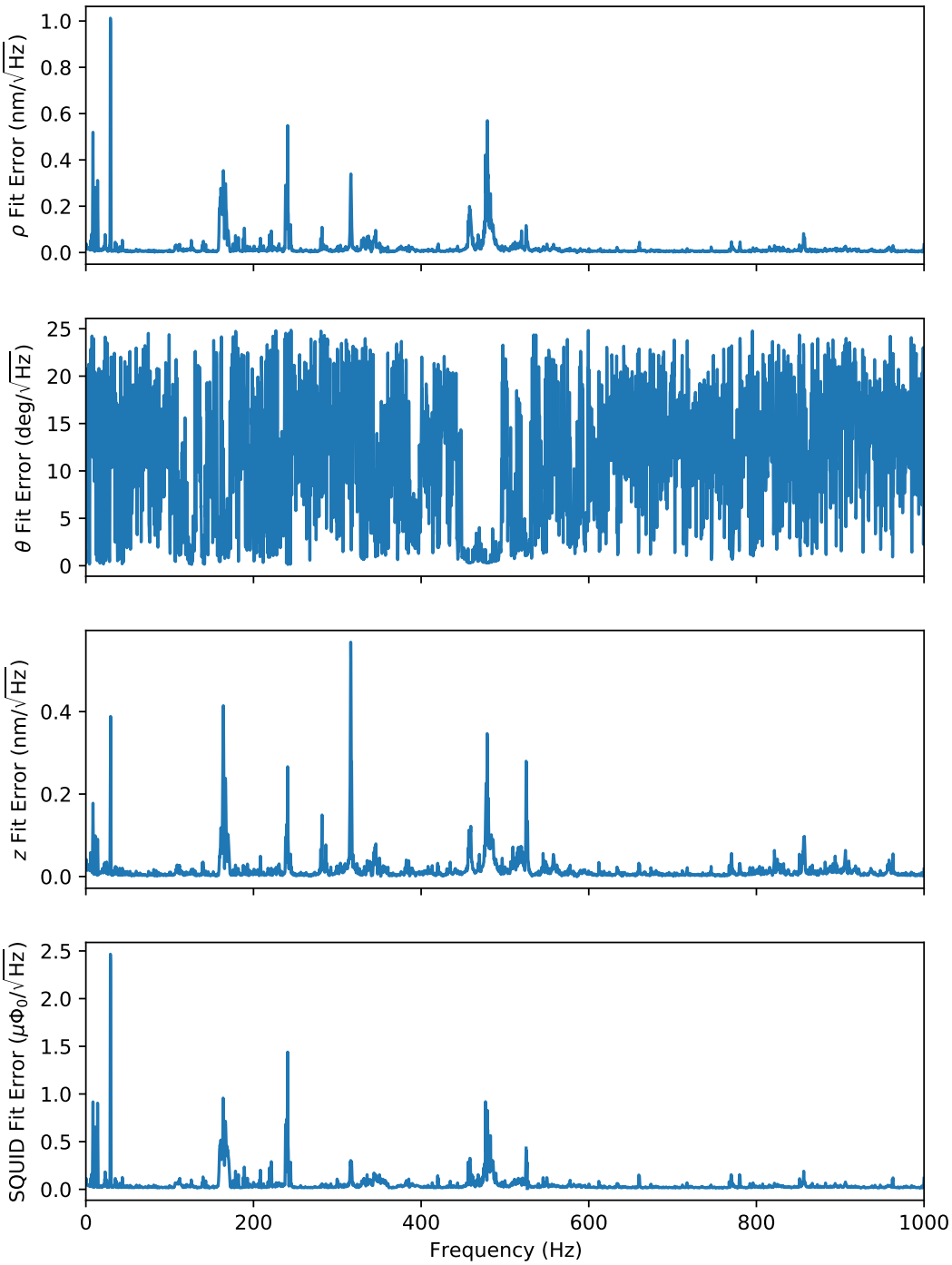

Figure 5.9: Confidence Interval at 95% of the fit parameters from statistical bootstrapping. The in-plane (ρ) and out of plane (z) error in the fit is less than $1\,\mathrm{nm}/\sqrt{\mathrm{Hz}}$ and the error in the SQUID noise is less than $2.5\,\mu\Phi_0/\sqrt{\mathrm{Hz}}$. There is a fairly large uncertainty in the direction of in-plane vibration (θ) except around the 480 Hz peak.

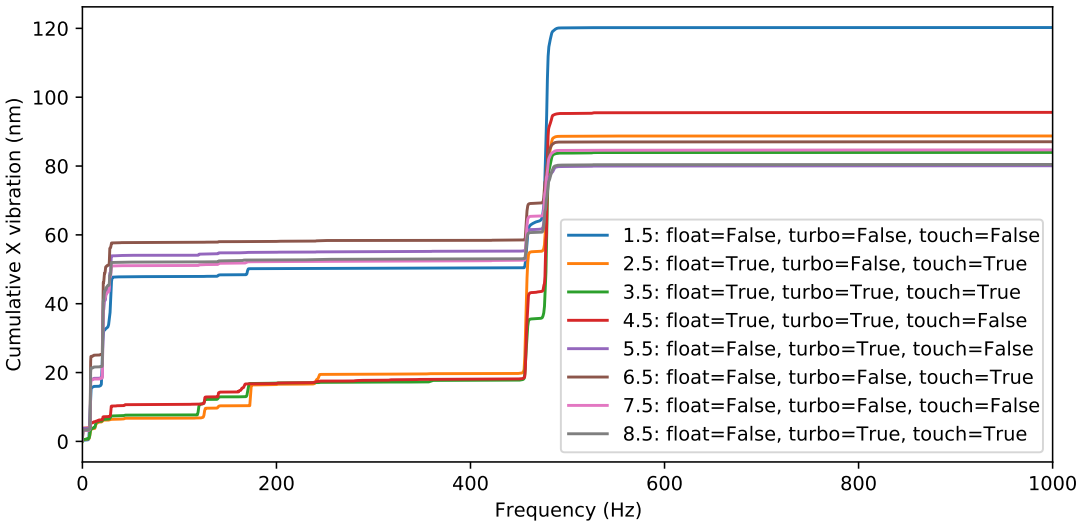

Figure 5.10: Cumulative vibration in the x direction for all datasets taken with the superconducting vortex. We note the status of the air springs (floating or not floating), if the turbo pump for the dilution cycle is on or off, and if the capacitance measurement recorded a touch or if no touch was recorded.

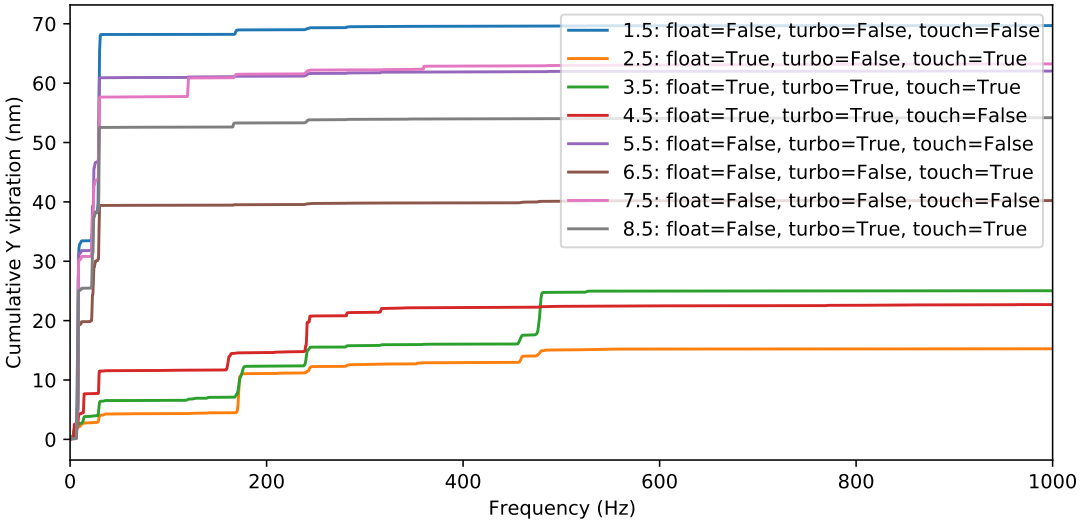

Figure 5.11: Cumulative vibration in the y direction for all datasets taken with the superconducting vortex. We note the status of the air springs (floating or not floating), if the turbo pump for the dilution cycle is on or off, and if the capacitance measurement recorded a touch or if no touch was recorded.

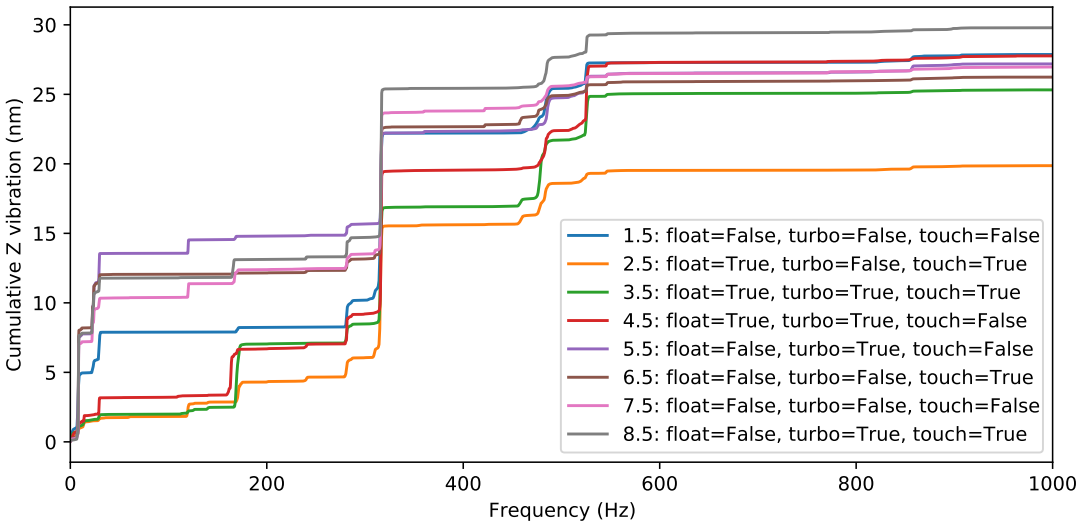

Figure 5.12: Cumulative vibration in the z direction for all datasets taken with the superconducting vortex. We note the status of the air springs (floating or not floating), if the turbo pump for the dilution cycle is on or off, and if the capacitance measurement recorded a touch or if no touch was recorded.

We plot the cumulative vibrations for 8 datasets that we measured over the span of a week in Figure 5.10, 5.11, 5.12. They are numbered in order of when we took the measurement and we include details about the status of the cryostat during those datasets. The datasets are numbered with a .5 to denote that they fit with the newer model that includes intrinsic SQUID noise. Each dataset could be taken with the air springs pressurized which "floats" the experiment, decoupling it from vibrational noise from the floor and with the turbo pump on or off, which circulates the mixture and may add vibrations. We measure the capacitance through all the measurements so we can determine if the SQUID ever touches the sample during any of these measurements. For each dataset plotted in Figures 5.10, 5.11, 5.12, we label each dataset with all of these attributes. There is not a significant and consistent difference between datasets where the helium mixture was circulating and not circulating suggesting that the dilution cycle does not contribute to the

vibrations. There also are not significant differences between datasets where the capacitance measurement recorded a touch and ones where it did not, suggesting that the capacitance measurement here was faulty. This is not surprising, as we were almost certain we were not in contact for any of these datasets and we were staying over the same vortex for the entire week of measurement. We do see some difference due to floating and not floating the cryostat on the air-springs.

We notice a large increase in vibrations at about 480 Hz. We see an increase in the x, y directions for all datasets. However, we can clearly see two distinct groups of datasets when examining the x and y vibrations: datasets (2.5-4.5) and datasets (5.5-8.5). For the x direction in the first group of datasets, there is an increase of about 60 nm around 480 Hz where in the second group the increase is is half as large. However, there is a large increase in noise in the second group 25 Hz that results in the total vibrations in the x direction being very comparable. In the y direction, we see something more dramatic where the first group of datasets have very little increase in vibration while the second group have a large increase at around 25 Hz.

By examining the cryostat status at each dataset, we can clearly see that floating the cryostat correlates with eliminating the increase in vibration at 25 Hz. We might conclude that floating the cryostat eliminates the low frequency peaks but the total vibration remains similar because vibrational power up-mixes to higher frequencies. However dataset 1.5 suggests otherwise. Dataset 1.5 has the cryostat not floating and is similar to group of datasets where the cryostat is not floating at low frequency. However, unlike the rest of the dataset (5.5-8.5), this dataset shows a similarly large increase in vibrations at 480 Hz compared to the dataset 1.5. This suggests that the source of the large vibrations at 480 Hz might not be

something related to the microscope but something time dependent on the week time scale such as another experiment in the building. Unfortunately our measurements are not definitive because we did not measure another dataset with the cryostat floating after dataset 8.5.

In summary, we have not observe a noticeable difference between the vibrations with and without the circulation of the mixture. We have recorded motion of the mixing chamber plate along the vertical direction using a geophone, since we cannot measure the sample-to-SQUID vibrations with the pulse tube turned off. With the vacuum cans closed and the cryostat at room temperature, no noticeable motion is detected with the pulse tube turned off, however with the pulse tube turned on, some motion is clearly present at higher frequencies. However the amplitudes and exact positions of peaks are not strongly correlated with the peaks visible in Figure 5.7. We speculate that the motion we observe above 200 Hz has contributions from the pulse tube and that resonances in the microscope shape the spectrum we observe, but that an additional source of vibrations is intermittently present in the lab.

5.3 Conclusions and Outlook

I have described our method of characterizing vibrations in our SQUID microscope in our dilution refrigerator. The origin of the large vibrational peak around 480 Hz remains unsolved. The intermittent nature of these vibrations invites further study.

APPENDIX A

IT MAINTENANCE

I built the network back-end for the lab. Unfortunately, I did not train anyone before I left. The goal of this section is to provide future graduate students with enough information that it would be possible to fix a problem with the lab network. It will require research. This is not meant to be a guide on how to fix a potential problem.

The server (minnow) is a Xen hypervisor with a Arch Linux Dom0. A hypervisor is a generalization of virtualization. A type 1 hypervisor is like Xen or VMWare ESXI. A type 2 hypervisor is like VirtualBox or Parallels. If you connect directly to minnow through a monitor and keyboard, you will be in an Arch Linux environment (the Dom0). On top of the hypervisor are many different virtual machines. Each virtual machine (VM) contains a different service, such as the DNS server, VPN server, and file-server. The advantage to using VMs is that you can save the VM and reload it so you can always guarantee the server functions even if you change things. Note, this backup process is manual, not automatic. You cannot revert the VM to a previous version without saving.

The DNS server has two network interfaces and acts as the firewall and router for the lab. The first network interface is directly linked to one of the Ethernet ports on minnow and connects to Cornell's internal network. The second network interface is internal and there is an internal router that serves all the VMs and any computer on the second minnow Ethernet. This VM also provides the IP addresses for the internal lab network. It also restricts communication if necessary. For instance, we prevent computers in the DR room from contacting the outside world. All network traffic from the lab is routed through the DNS server. You will

need root access to modify the firewall, router, and static IP addresses. To change the firewall and router, use iptables. To modify the static IP addresses, find the dnsmasq.conf file.

The VPN server is from openvpn. The purpose of a VPN is to allow computer outside the internal network to access anything inside the internal network without compromising security. It requires keys and a client on the external computer. The only thing you might need to do with the VPN server is to make new keys. For that, you do not need to access the VPN server on minnow, you will need to access the VPN key server. For security reasons the VPN key server is on a separate VPN that has little access to the general network. The key server often stays on manchot instead of minnow. You will login as root, no password, go into `easy-rsa`, and execute `build-key filename-of-key`. Then, you will need to scp the keys to a different computer. Note that a key expire yearly because a key cannot be blacklisted. **By 2032, the VPN root key will need to be replaced.** This will require modifying the VPN server VM. Replacing the root server key will require replacing all of the keys.

The file-server uses both samba and nfs. Samba allows access by windows computers while nfs allows access by linux or unix computers. The fileserver also has direct PCI pass-through access to the RAID card which performs RAID 5 on the given disks. Most of the file-server is stable but it requires someone to execute a single command after every power failure. The samba server gets confused on reboot and requires you to restart the service with `systemctl restart smbd` executed from root. Note that the static IP of the file-server is `192.168.0.8`.

APPENDIX B

DIPPING PROBE USAGE

The dipping probe was designed with a outer diameter that is almost too large to safely fit in the neck of the standard transport dewar. Additionally, these transport dewars lack some of the safety features present in dewars specifically designed for dipping probe style systems. Operating this system thus requires a little more care.

The main concern is that the dipping probe becomes stuck in the neck of the transport dewar. If the seal is tight enough and ice builds up in the neck of the dewar, this could create an explosive device.

The quick connect coupling should always be clamped onto the helium dewar if the vacuum can is in the dewar more than 1/3 of the length of the vacuum can.

If one follows this simple rule, the vacuum can will always be parallel to the neck of the dewar. If there is a large weld bead in the neck of the dewar, the vacuum can will hit the weld bead and stop. There is no way to lock the vacuum can in the neck of the dewar as there is no way to get past the weld bead. You can also feel how rough the vacuum can scrapes as it is inserted into the dewar. An increasingly rough insertion indicates that this dewar is slightly too small.

When extracting the vacuum can from the dewar, the quick connect coupling is loosened. Frost often develops on the can as you extract it from the dewar. It might be alluring to unclasp the quick connect from the helium dewar and yank the probe from the dewar. **Avoid unclamping the quick connect until the probe is 2/3 out of the neck of the dewar!** Pulling the dipping probe from

Dewar	Fits?	Notes
C046	Yes	The neck of the dewar is offset with the mouth. The opening is large enough but the quick connect does not sit nicely on the flange. If you leave the clamp loose, the probe slides with a little friction but work fine.
C057	No	Slides in if you force it but requires a loose quick connect
C059	Yes	Smooth, no discernible contact points
C063	Yes	Smooth, no discernible contact points
C067	Yes	Smooth, no discernible contact points
C069	No	Does not fit the smaller RF dipping probe. Rachel Resnick tested this dewar
C070	No?	Fits the smaller, RF dipping probe but got jammed with this dipping probe. Matt Ferguson tested this dewar
C071	Yes	Smooth, frictionless fit
C073	No	First measurement saw the o-ring was tight (ungreased) but a second test found that this dewar does not fit

Table B.1: Dewars that safely accommodates the dipping probe. These dewars were measured by David Low unless otherwise noted. If the dewars was measured by people other than David Low, the quick connect might not have been connected.

the dewar with the quick connect clamped in a single smooth motion limits the frost that develops. It requires a little more force and leverage but is significantly safer. I am neither tall nor muscular and I am easily able to accomplish this action. Extra leverage from a stool can also be used. Greasing the o-ring of the quick connect before cooling the dipping probe or using a heat gun to warm the quick connect can also help. If the probe gets jammed, waiting will often allow the vacuum can and quick connect to warm and make removing the dipping probe easier. **If the dipping probe gets lodged in the neck of the dewar, seek help immediately.**

We have included a selection of dewars that have been tested to work with the existing dipping probe can in Table B.1.

BIBLIOGRAPHY

[1] R. Barends, J. Kelly, A. Megrant, D. Sank, E. Jeffrey, Y. Chen, Y. Yin, B. Chiaro, J. Mutus, C. Neill, P. O'Malley, P. Roushan, J. Wenner, T. C. White, A. N. Cleland, and John M. Martinis. Coherent josephson qubit suitable for scalable quantum integrated circuits. *Phys. Rev. Lett.*, 111:080502, Aug 2013.

[2] R. Barends, J. Kelly, A. Megrant, A. Veitia, D. Sank, E. Jeffrey, T. C. White, J. Mutus, A. G. Fowler, B. Campbell, Y. Chen, Z. Chen, B. Chiaro, A. Dunsworth, C. Neill, P. O'Malley, P. Roushan, A. Vainsencher, J. Wenner, A. N. Korotkov, A. N. Cleland, and John M. Martinis. Superconducting quantum circuits at the surface code threshold for fault tolerance. *Nature*, 508(7497):500–503, Apr 2014.

[3] Julie A. Bert, Beena Kalisky, Christopher Bell, Minu Kim, Yasuyuki Hikita, Harold Y. Hwang, and Kathryn A. Moler. Direct imaging of the coexistence of ferromagnetism and superconductivity at the $LaAlO_3/SrTiO_3$ interface. *Nature Physics*, 7(10):767–771, 9 2011.

[4] Logan Bishop-Van Horn, Zheng Cui, John R. Kirtley, and Kathryn A. Moler. Cryogen-free variable temperature scanning squid microscope. *Review of Scientific Instruments*, 90(6):063705, 2019.

[5] Per G Björnsson, Brian W Gardner, John R Kirtley, and Kathryn A Moler. Scanning superconducting quantum interference device microscope in a dilution refrigerator. *Review of Scientific Instruments*, 72(11):4153–4158, 2001.

[6] RC Black, A Mathai, FC Wellstood, E Dantsker, AH Miklich, DT Nemeth, JJ Kingston, and J Clarke. Magnetic microscopy using a liquid nitrogen cooled yba2cu3o7 superconducting quantum interference device. *Applied physics letters*, 62(17):2128–2130, 1993.

[7] Hendrik Bluhm, Nicholas C. Koshnick, Julie A. Bert, Martin E. Huber, and Kathryn A. Moler. Persistent Currents in Normal Metal Rings. *Physical Review Letters*, 102(13):136802, 3 2009.

[8] Alex I. Braginski and John Clarke. *The SQUID Handbook*, volume 1. Wiley-VCH, 2004.

[9] C Z Chang, J Zhang, X Feng, J Shen, Z Zhang, M Guo, K Li, Y Ou, P Wei, L L Wang, Z Q Ji, Y Feng, S Ji, X Chen, J Jia, X Dai, Z Fang, S C Zhang,

K He, Y Wang, L Lu, X C Ma, and Q K Xue. Experimental Observation of the Quantum Anomalous Hall Effect in a Magnetic Topological Insulator. *Science*, 340(6129):167–170, 2013.

[10] Cui-Zu Chang, Weiwei Zhao, Duk Y. Kim, Haijun Zhang, Badih A. Assaf, Don Heiman, Shou-Cheng Zhang, Chaoxing Liu, Moses H. W. Chan, and Jagadeesh S. Moodera. High-precision realization of robust quantum anomalous hall state in a hard ferromagnetic topological insulator. *Nature Materials*, 14(5):473–477, May 2015.

[11] I. Chiorescu, Y. Nakamura, C. J. P. M. Harmans, and J. E. Mooij. Coherent quantum dynamics of a superconducting flux qubit. *Science*, 299(5614):1869–1871, 2003.

[12] D. V. Christensen, Y. Frenkel, Y. Z. Chen, Y. W. Xie, Z. Y. Chen, Y. Hikita, A. Smith, L. Klein, H. Y. Hwang, N. Pryds, and B. Kalisky. Strain-tunable magnetism at oxide domain walls. *Nature Physics*, 15(3):269–274, Mar 2019.

[13] J. Dechert, M. Mueck, and C. Heiden. A scanning squid microscope for samples at room temperature. *IEEE Transactions on Applied Superconductivity*, 9(2):4111–4114, 1999.

[14] A. M. J. den Haan, G. H. C. J. Wijts, F. Galli, O. Usenko, G. J. C. van Baarle, D. J. van der Zalm, and T. H. Oosterkamp. Atomic resolution scanning tunneling microscopy in a cryogen free dilution refrigerator at 15 mk. *Review of Scientific Instruments*, 85(3):035112, 2014.

[15] Haiming Deng, Zhiyi Chen, Agnieszka Wołoś, Marcin Konczykowski, Kamil Sobczak, Joanna Sitnicka, Irina V. Fedorchenko, Jolanta Borysiuk, Tristan Heider, Łukasz Pluciński, Kyungwha Park, Alexandru B. Georgescu, Jennifer Cano, and Lia Krusin-Elbaum. High-temperature quantum anomalous hall regime in a mnbi2te4/bi2te3 superlattice. *Nature Physics*, 17(1):36–42, Jan 2021.

[16] B. Efron and R. Tibshirani. Bootstrap methods for standard errors, confidence intervals, and other measures of statistical accuracy. *Statist. Sci.*, 1(1):77, 02 1986.

[17] J Ekin. *Experimental techniques for low-temperature measurements: cryostat design, material properties and superconductor critical-current testing*. Oxford University Press, Oxford, 2006.

[18] S. Etaki, M. Poot, I. Mahboob, K. Onomitsu, H. Yamaguchi, and H. S. J. van der Zant. Motion detection of a micromechanical resonator embedded in a d.c. squid. *Nature Physics*, 4(10):785–788, Oct 2008.

[19] A. Finkler, D. Vasyukov, Y. Segev, L. Ne'eman, E. O. Lachman, M. L. Rappaport, Y. Myasoedov, E. Zeldov, and M. E. Huber. Scanning superconducting quantum interference device on a tip for magnetic imaging of nanoscale phenomena. *Review of Scientific Instruments*, 83(7):073702, 2012.

[20] L. E. Fong, J. R. Holzer, K. K. McBride, E. A. Lima, F. Baudenbacher, and M. Radparvar. High-resolution room-temperature sample scanning superconducting quantum interference device microscope configurable for geological and biomagnetic applications. *Review of Scientific Instruments*, 76(5):053703, 2005.

[21] F. Foroughi, J.-M. Mol, T. Müller, J. R. Kirtley, K. A. Moler, and H. Bluhm. A micro-squid with dispersive readout for magnetic scanning microscopy. *Applied Physics Letters*, 112(25):252601, 2018.

[22] E. J. Fox, I. T. Rosen, Yanfei Yang, George R. Jones, Randolph E. Elmquist, Xufeng Kou, Lei Pan, Kang L. Wang, and D. Goldhaber-Gordon. Part-per-million quantization and current-induced breakdown of the quantum anomalous hall effect. *Phys. Rev. B*, 98:075145, Aug 2018.

[23] Yiftach Frenkel, Noam Haham, Yishai Shperber, Christopher Bell, Yanwu Xie, Zhuoyu Chen, Yasuyuki Hikita, Harold Y. Hwang, Ekhard K. H. Salje, and Beena Kalisky. Imaging and tuning polarity at srtio3 domain walls. *Nature Materials*, 16(12):1203–1208, Dec 2017.

[24] Sergey M. Frolov, Micah J. A. Stoutimore, Trevis A. Crane, Dale J. Van Harlingen, Vladimir A. Oboznov, Valery V. Ryazanov, Adele Ruosi, Carmine Granata, and Maurizio Russo. Imaging spontaneous currents in superconducting arrays of π-junctions. *Nature Physics*, 4(1):32–36, 1 2008.

[25] Dorri Halbertal, Moshe Ben Shalom, Aviram Uri, Kousik Bagani, Alexander Y. Meltzer, Ido Marcus, Yuri Myasoedov, John Birkbeck, Leonid S. Levitov, Andre K. Geim, and Eli Zeldov. Imaging resonant dissipation from individual atomic defects in graphene. *Science*, 358(6368):1303–1306, 2017.

[26] M. Hatridge, R. Vijay, D. H. Slichter, John Clarke, and I. Siddiqi. Dispersive magnetometry with a quantum limited squid parametric amplifier. *Phys. Rev. B*, 83:134501, Apr 2011.

[27] D. Hautot, Q. A. Pankhurst, N. Khan, and J. Dobson. Preliminary evaluation of nanoscale biogenic magnetite in alzheimer's disease brain tissue. *Proceedings of the Royal Society of London. Series B: Biological Sciences*, 270(suppl_1):S62–S64, 2003.

[28] M. Hirota, T. Furuse, K. Ebana, H. Kubo, K. Tsushima, T. Inaba, A. Shima, M. Fujinuma, and N. Tojyo. Magnetic detection of a surface ship by an airborne lts squid mad. *IEEE Transactions on Applied Superconductivity*, 11(1):884–887, 2001.

[29] Martin E Huber, Nicholas C Koshnick, Hendrik Bluhm, Leonard J Archuleta, Tommy Azua, Per G. Björnsson, Brian W Gardner, Sean T Halloran, Erik A Lucero, and Kathryn A Moler. Gradiometric micro-SQUID susceptometer for scanning measurements of mesoscopic samples. *Review of Scientific Instruments*, 79(5):053704, 2008.

[30] Sergey Ioffe and Christian Szegedy. Batch normalization: Accelerating deep network training by reducing internal covariate shift. In *Proceedings of the 32nd International Conference on International Conference on Machine Learning - Volume 37*, ICML'15, page 448–456. JMLR.org, 2015.

[31] Beena Kalisky, Eric M. Spanton, Hilary Noad, John R. Kirtley, Katja C. Nowack, Christopher Bell, Hiroki K. Sato, Masayuki Hosoda, Yanwu Xie, Yasuyuki Hikita, Carsten Woltmann, Georg Pfanzelt, Rainer Jany, Christoph Richter, Harold Y. Hwang, Jochen Mannhart, and Kathryn A. Moler. Locally enhanced conductivity due to the tetragonal domain structure in $LaAlO_3/SrTiO_3$ heterointerfaces. *Nature Materials*, 12(12):1091–1095, 9 2013.

[32] M. B. Ketchen, T. Kopley, and H. Ling. Miniature squid susceptometer. *Applied Physics Letters*, 44(10):1008–1010, 1984.

[33] Diederik P. Kingma and Jimmy Ba. Adam: A method for stochastic optimization, 2017.

[34] J R Kirtley. Fundamental studies of superconductors using scanning magnetic imaging. *Reports on Progress in Physics*, 73(12):126501, 12 2010.

[35] J. R. Kirtley, M. B. Ketchen, K. G. Stawiasz, J. Z. Sun, W. J. Gallagher, S. H. Blanton, and S. J. Wind. High-resolution scanning squid microscope. *Applied Physics Letters*, 66(9):1138–1140, 1995.

[36] J. R. Kirtley, M. B. Ketchen, C. C. Tsuei, J. Z. Sun, W. J. Gallagher, Lock See Yu-Jahnes, A. Gupta, K. G. Stawiasz, and S. J. Wind. Design and applications

of a scanning squid microscope. *IBM Journal of Research and Development*, 39(6):655–668, 1995.

[37] J. R. Kirtley, C. C. Tsuei, Ariando, C. J. M. Verwijs, S. Harkema, and H. Hilgenkamp. Angle-resolved phase-sensitive determination of the in-plane gap symmetry in $YBa_2Cu_3O_{7-\delta}$. *Nature Physics*, 2(3):190–194, 3 2006.

[38] John R. Kirtley, Lisa Paulius, Aaron J. Rosenberg, Johanna C. Palmstrom, Connor M. Holland, Eric M. Spanton, Daniel Schiessl, Colin L. Jermain, Jonathan Gibbons, Y.-K.-K. Fung, Martin E. Huber, Daniel C. Ralph, Mark B. Ketchen, Gerald W. Gibson, and Kathryn A. Moler. Scanning squid susceptometers with sub-micron spatial resolution. *Review of Scientific Instruments*, 87(9):093702, 2016.

[39] Jens Koch, Terri M. Yu, Jay Gambetta, A. A. Houck, D. I. Schuster, J. Majer, Alexandre Blais, M. H. Devoret, S. M. Girvin, and R. J. Schoelkopf. Charge-insensitive qubit design derived from the cooper pair box. *Phys. Rev. A*, 76:042319, Oct 2007.

[40] N. C. Koshnick, H. Bluhm, M. E. Huber, and K. A. Moler. Fluctuation Superconductivity in Mesoscopic Aluminum Rings. *Science*, 318(5855):1440–1443, 11 2007.

[41] E. O. Lachman, A F Young, A Richardella, J Cuppens, H. R. Naren, Y Anahory, A Y Meltzer, A Kandala, S Kempinger, Y Myasoedov, M E Huber, N Samarth, and E Zeldov. Visualization of superparamagnetic dynamics in magnetic topological insulators. *Science Advances*, 1(10):e1500740–e1500740, 11 2015.

[42] Ella O. Lachman, Masataka Mogi, Jayanta Sarkar, Aviram Uri, Kousik Bagani, Yonathan Anahory, Yuri Myasoedov, Martin E. Huber, Atsushi Tsukazaki, Masashi Kawasaki, Yoshinori Tokura, and Eli Zeldov. Observation of superparamagnetism in coexistence with quantum anomalous hall $c = \pm 1$ and $c = 0$ chern states. *npj Quantum Materials*, 2(1):70, Dec 2017.

[43] E M Levenson-Falk, N Antler, and I Siddiqi. Dispersive nanoSQUID magnetometry. *Superconductor Science and Technology*, 29(11):113003, sep 2016.

[44] Chao-Xing Liu, Shou-Cheng Zhang, and Xiao-Liang Qi. The quantum anomalous hall effect: Theory and experiment. *Annual Review of Condensed Matter Physics*, 7(1):301–321, 2016.

[45] D. Low, G. M. Ferguson, Alexander Jarjour, Brian T. Schaefer, Maja D. Bachmann, Philip J. W. Moll, and Katja C. Nowack. Scanning squid microscopy in a cryogen-free dilution refrigerator. *Review of Scientific Instruments*, 92(8):083704, 2021.

[46] D. Low, G. M. Ferguson, Alexander Jarjour, Brian T. Schaefer, and Katja C. Nowack. Design files for a scanning superconducting quantum interference device operated in a cryogen-free dilution refrigerator. *Zenodo*, 2021.

[47] YP Ma, IM Thomas, A Lauder, and JP Wikswo. A high resolution imaging susceptometer. *IEEE transactions on applied superconductivity*, 3(1):1941–1944, 1993.

[48] A. Marguerite, J. Birkbeck, A. Aharon-Steinberg, D. Halbertal, K. Bagani, I. Marcus, Y. Myasoedov, A. K. Geim, D. J. Perello, and E. Zeldov. Imaging work and dissipation in the quantum hall state in graphene. *Nature*, 575(7784):628–633, Nov 2019.

[49] J. A. B. Mates, D. T. Becker, D. A. Bennett, B. J. Dober, J. D. Gard, J. P. Hays-Wehle, J. W. Fowler, G. C. Hilton, C. D. Reintsema, D. R. Schmidt, D. S. Swetz, L. R. Vale, and J. N. Ullom. Simultaneous readout of 128 x-ray and gamma-ray transition-edge microcalorimeters using microwave squid multiplexing. *Applied Physics Letters*, 111(6):062601, 2017.

[50] H Minami, Q Geng, K Chihara, J Yuyama, and E Goto. Detection of trapped flux quanta in superconducting films by scanning a squid pick-up coil. *Cryogenics*, 32(7):648–652, 1992.

[51] Y. Nakashima, F. Hirayama, S. Kohjiro, H. Yamamori, S. Nagasawa, A. Sato, S. Yamada, R. Hayakawa, N. Y. Yamasaki, K. Mitsuda, K. Nagayoshi, H. Akamatsu, L. Gottardi, E. Taralli, M. P. Bruijn, M. L. Ridder, J. R. Gao, and J. W. A. den Herder. Low-noise microwave squid multiplexed readout of 38 x-ray transition-edge sensor microcalorimeters. *Applied Physics Letters*, 117(12):122601, 2020.

[52] Katja C Nowack, Eric M Spanton, Matthias Baenninger, Markus König, John R Kirtley, Beena Kalisky, C Ames, Philipp Leubner, Christoph Brüne, Hartmut Buhmann, Laurens W Molenkamp, David Goldhaber-Gordon, and Kathryn A Moler. Imaging currents in HgTe quantum wells in the quantum spin Hall regime. *Nature Materials*, 12(9):787–791, 6 2013.

[53] Hiroshi Ohta, Toshiaki Matsui, and Yoshinori Uchikawa. A whole-head squid

system in a superconducting magnetic shield. *IEEE Transactions on Applied Superconductivity*, 17(2):730–733, 2007.

[54] Yoshio Okada, Matti Hämäläinen, Kevin Pratt, Anthony Mascarenas, Paul Miller, Menglai Han, Jose Robles, Anders Cavallini, Bill Power, Kosal Sieng, Limin Sun, Seok Lew, Chiran Doshi, Banu Ahtam, Christoph Dinh, Lorenz Esch, Ellen Grant, Aapo Nummenmaa, and Douglas Paulson. Babymeg: A whole-head pediatric magnetoencephalography system for human brain development research. *Review of Scientific Instruments*, 87(9):094301, 2016.

[55] Yoshio Okada, Kevin Pratt, Christopher Atwood, Anthony Mascarenas, Richard Reineman, Jussi Nurminen, and Douglas Paulson. Babysquid: A mobile, high-resolution multichannel magnetoencephalography system for neonatal brain assessment. *Review of Scientific Instruments*, 77(2):024301, 2006.

[56] M. Pelliccione, A. Sciambi, J. Bartel, A. J. Keller, and D. Goldhaber-Gordon. Design of a scanning gate microscope for mesoscopic electron systems in a cryogen-free dilution refrigerator. *Review of Scientific Instruments*, 84(3):033703, 2013.

[57] M. Pelliccione, A. Sciambi, J. Bartel, A. J. Keller, and D. Goldhaber-Gordon. Design of a scanning gate microscope for mesoscopic electron systems in a cryogen-free dilution refrigerator. *Review of Scientific Instruments*, 84(3), 2013.

[58] Matthew Pelliccione, Alec Jenkins, Preeti Ovartchaiyapong, Christopher Reetz, Eve Emmanouilidou, Ni Ni, and Ania C. Bleszynski Jayich. Scanned probe imaging of nanoscale magnetism at cryogenic temperatures with a single-spin quantum sensor. *Nature Nanotechnology*, 11(8):700–705, 5 2016.

[59] Francesca Paola Quacquarelli, Jorge Puebla, Thomas Scheler, Dieter Andres, Christoph Bödefeld, Balázs Sipos, Claudio Dal Savio, Andreas Bauer, Christian Pfleiderer, Andreas Erb, and Khaled Karral. Scanning probe microscopy in an ultra-low vibration closed-cycle cryostat: Skyrmion lattice detection and tuning fork implementation. *Microscopy Today*, 23(6):12–17, 2015.

[60] Matthew Reagor, Christopher B Osborn, Nikolas Tezak, Alexa Staley, Guenevere Prawiroatmodjo, Michael Scheer, Nasser Alidoust, Eyob A Sete, Nicolas Didier, Marcus P da Silva, et al. Demonstration of universal parametric entangling gates on a multi-qubit lattice. *Science advances*, 4(2):eaao3603, 2018.

[61] Carl D. Reintsema, Jörn Beyer, Sae Woo Nam, Steve Deiker, Gene C. Hilton, Kent Irwin, John Martinis, Joel Ullom, Leila R. Vale, and Mike MacIntosh.

Prototype system for superconducting quantum interference device multiplexing of large-format transition-edge sensor arrays. *Review of Scientific Instruments*, 74(10):4500–4508, 2003.

[62] Francis J. Ridgeon, Mark J. Raine, D. P. Halliday, M'hamed Lakrimi, Adrian Thomas, and Damian P. Hampshire. Superconducting properties of titanium alloys (ti-64 and ti-6242) for critical current barrels. *IEEE Transactions on Applied Superconductivity*, 27(4):1–5, 2017.

[63] Daniel Schiessl, John R. Kirtley, Lisa Paulius, Aaron J. Rosenberg, Johanna C. Palmstrom, Rahim R. Ullah, Connor M. Holland, Y.-K.-K. Fung, Mark B. Ketchen, Gerald W. Gibson, and Kathryn A. Moler. Determining the vibrations between sensor and sample in squid microscopy. *Applied Physics Letters*, 109(23):232601, 2016.

[64] Yishai Shperber, Naor Vardi, Eylon Persky, Shai Wissberg, Martin E. Huber, and Beena Kalisky. Scanning squid microscopy in a cryogen-free cooler. *Review of Scientific Instruments*, 90(5):053702, 2019.

[65] Jeffrey Siegel, Jeff Witt, Naia Venturi, and Stuart Field. Compact large-range cryogenic scanner. *Review of Scientific Instruments*, 66(3):2520–2523, 1995.

[66] Eric M. Spanton, Mingtang Deng, Saulius Vaitiekenas, Peter Krogstrup, Jesper Nygård, Charles M. Marcus, and Kathryn A. Moler. Current-phase relations of few-mode InAs nanowire Josephson junctions. *Nature Physics*, 13(12):1177–1181, 12 2017.

[67] Nitish Srivastava, Geoffrey Hinton, Alex Krizhevsky, Ilya Sutskever, and Ruslan Salakhutdinov. Dropout: A simple way to prevent neural networks from overfitting. *J. Mach. Learn. Res.*, 15(1):1929–1958, January 2014.

[68] Chiu-Chun Tang, Hui-Ting Lin, Sing-Lin Wu, Tse-Jun Chen, M. J. Wang, D. C. Ling, C. C. Chi, and Jeng-Chung Chen. An interchangeable scanning hall probe/scanning squid microscope. *Review of Scientific Instruments*, 85(8):083707, 2014.

[69] C. L. Tschirhart, M. Serlin, H. Polshyn, A. Shragai, Z. Xia, J. Zhu, Y. Zhang, K. Watanabe, T. Taniguchi, M. E. Huber, and A. F. Young. Imaging orbital ferromagnetism in a moiré chern insulator, 2020.

[70] A. Uri, S. Grover, Y. Cao, J.A. Crosse, K. Bagani, D. Rodan-Legrain, Y. Myasoedov, K. Watanabe, T. Taniguchi, P. Moon, M. Koshino, P. Jarillo-Herrero,

and E. Zeldov. Mapping the twist-angle disorder and landau levels in magic-angle graphene. *Nature*, 581:47–52, 2020.

[71] Denis Vasyukov, Yonathan Anahory, Lior Embon, Dorri Halbertal, Jo Cuppens, Lior Neeman, Amit Finkler, Yehonathan Segev, Yuri Myasoedov, Michael L. Rappaport, Martin E. Huber, and Eli Zeldov. A scanning superconducting quantum interference device with single electron spin sensitivity. *Nature Nanotechnology*, 8(9):639–644, Sep 2013.

[72] L.N. Vu and D.J. Van Harlingen. Design and implementation of a scanning squid microscope. *IEEE Transactions on Applied Superconductivity*, 3(1):1918–1921, 1993.

[73] X. Renshaw Wang, C. J. Li, W. M. Lu, T. R. Paudel, D. P. Leusink, M. Hoek, N. Poccia, A. Vailionis, T. Venkatesan, J. M. D. Coey, E. Y. Tsymbal, Ariando, and H. Hilgenkamp. Imaging and control of ferromagnetism in LaMnO3/SrTiO3 heterostructures. *Science*, 349(6249):716–719, 8 2015.

[74] Shai Wissberg, Maria Ronen, Ziv Oren, Doron Gerber, and Beena Kalisky. Sensitive readout for microfluidic high-throughput applications using scanning squid microscopy. *Scientific Reports*, 10(1):1573, Jan 2020.

[75] Friedrich Wulschner, Jan Goetz, Fabian R. Koessel, Elisabeth Hoffmann, Alexander Baust, Peter Eder, Michael Fischer, Max Haeberlein, Manuel J. Schwarz, Matthias Pernpeintner, Edwar Xie, Ling Zhong, Christoph W. Zollitsch, Borja Peropadre, Juan-Jose Garcia Ripoll, Enrique Solano, Kirill G. Fedorov, Edwin P. Menzel, Frank Deppe, Achim Marx, and Rudolf Gross. Tunable coupling of transmission-line microwave resonators mediated by an rf squid. *EPJ Quantum Technology*, 3(1):10, Jul 2016.